Fault Gouge Characterization in the Øygarden Complex in SW Norway

Relevance for offshore CO_2 storage

Master of Science Thesis

in Geoscience

Anders Bjørnstad

Department of Earth Science

University of Bergen

June 2022

Abstract

Pre-existing structures such as faults are common within the North Sea sedimentary basin. Fault-bounded reservoirs provide significant closures for subsurface storing of CO_2. An understanding of faults and fault rocks is therefore crucial for evaluating the long-term storage stability of CO_2 storage sites. When injecting CO_2 into a faulted or fault-bound reservoir, the increasing fluid pressure can lead to an increased risk of fault reactivation, which can cause earthquakes and alter the future fault sealing capabilities.

The Smeaheia area, a newly licensed CO_2 storage site (2022), at the Horda Platform in the Northern North Sea is juxtaposed with basement rocks of the Øygarden Complex to the east by the N-S striking Øygarden Fault System. The fault-related reactivation risk of the Smeaheia site towards the eastern basin-bounding Øygarden Fault System is closely linked to the characteristics of fault rocks present within the faulted crystalline basement rocks of the Øygarden Complex. Fault gouge, a clay-rich material found within the core of shallow brittle faults, is of particular interest, as this material can act as an impermeable barrier preventing fluid flow. Fault gouges represent the mechanically weakest material found within the fault core, and they may be associated with increased risk of reactivation. However, the presence of clay-rich gouge can also lower the likelihood of earthquakes by acting as a low friction gliding surface for the fault blocks, which is known as aseismic creep or stable sliding.

Despite fault rocks and fault gouges being highly important for CO_2 storage evaluation, the amount of data from intact offshore fault rocks is limited. In this work, we tested the friction angles of well-characterized fault rocks, i.e., fault gouges and fault breccias, from the Øygarden Complex by using accessible surface-exposed onshore faults. The fault rocks were characterized by grain size distribution and mineralogy using powdered clay analysis (XRD) and thin sections (optical microscopy). To determine the friction angles, the fault rock samples were subjected to direct shear box experimentation at normal stresses ranging from 0.1 to 1.5 MPa.

Six faults from the Øygarden Complex were sampled in addition to the well-documented Lærdal-Gjende fault for comparison purposes. The tested fault rocks had friction angles (ϕ) at 4 mm shear displacement (d) ranging from 17° to 31°, with a mean friction angle for the Øygarden Complex fault rocks of 23.5°. The sand-dominated gouges (45 to 67 %) had varying clay contents from 2 to 17 %. The fault gouges of the Øygarden Complex were predominantly quartzofeldspathic with clay minerals such as chlorite, kaolinite, illite and smectite. The tested fault rocks underwent systematic strain hardening during shearing at the higher normal stresses (1.0 to 1.5 MPa). However, the coarsest samples underwent significant strain hardening due to grain-locking even at the lower normal stresses (0.3 to 0.5 MPa). The results indicated no systematic correlation between the structural characteristics of the faults and the resulting friction angles. The fault rocks from the Øygarden Complex were on average weaker than the Lærdal-Gjende fault rocks and previous studies on natural gneissic fault rocks. However, significant variations in friction angles were also observed between the studied fault rocks due to the heterogeneous nature of fault cores. The results also showed systematic trends between the resulting friction angles, clay mineral concentrations, and grain-size properties, where clay-rich gouges had a lower friction angle.

This thesis offers insight into the friction angles we can expect from fault gouges derived from the Øygarden Complex and their physical properties. This data can be used as additional input data to model the risk of reactivation and the potential for induced seismicity of the Øygarden Fault System.

Acknowledgements

First, I would like to thank my supervisors, Prof. Joachim Jacobs, PhD. Elin Skurtveit, and Magnus Soldal, who has supported me throughout this work, and given great and valuable feedback. I thank you also for the many good discussions, it has been a thrill to work with you all.

Secondly, I want to thank the NCCS group, the Norwegian Geotechnical Institute (NGI), and the Department of Earth Science at the University of Bergen (UiB) for the good support and allowing me the opportunity to work on such an exciting project.

I thank Åse Hestnes for introducing me to the world of fault gouges. Andrew Walker, Maria Cansignia, and Diana Silva are thanked for introducing me to geotechnical lab-work, and for their great support and fruitful discussions. I want to thank Erlend Aven and Sjur Beyer for being excellent field trip companions. Also, many thanks to Andreas Viken at the University of Bergen, for going out of his way to create thin sections from difficult materials, and for the help with XRD analysis.

I would also like to thank my whole family for their support. Lastly, I want to give a special thanks to my son and my partner Hege.

Bergen 31.05.2022

Anders Bjørnstad

Table of Contents

1 Introduction and motivation

1.1 Background

With increased global CO_2 emissions, additional carbon reduction methods are required. The Norwegian government has initiated large-scale carbon capture and storage (CCS) projects, such as the Northern Lights and Longship projects, to accelerate the evaluation of storage sites and the associated risks. CCS is not a new project, and several projects have successfully captured CO_2 in hydrocarbon reservoirs (e.g., In Salah and Utsira High, Rutqvist, 2012). Norway has extensive experience producing hydrocarbons on the Norwegian Continental Shelf (NCS), and existing infrastructure, technology, and available reservoirs provide an excellent opportunity to store CO_2 over longer periods.

The Smeaheia site was opened for licensing and was awarded to Equinor for CO_2 storage in April 2022. Smeaheia is a tilted fault block at the Horda Platform in the North Sea, which is bound by the basement-involved N-S striking Vette Fault System (VFS) to the west and the N-S striking Øygarden Fault System (ØFS) to the east (Fig. 1A). The Smeaheia site is a suitable storage area which contains a structurally trapped and top-sealed sandstone reservoir, the Viking Group Sandstones. Three potential CO_2 storage sites within the Smeaheia, the Alpha, Beta, and Gamma structures, are considered for storage (Fig. 1A, Fig. 3B). The Alpha site is considered the primary target for CO_2 storage, as the top sealing Draupne Formation at the Beta site is close to the critical storage depth of 800 m for CO_2. The lateral- and along-fault fluid flow of the Øygarden Fault System is also more uncertain than the Alpha bounding Vette Fault System (Wu et al., 2021). The three sites are still closely linked in fluid and pressure communication, so injection into Alpha or Gamma might also affect the Beta site.

Faults can be reactivated by increasing the fluid pressure (Wang et al., 2020) or by dynamic pressure changes that span a much wider area than the injected CO_2 plume itself (Rutqvist, 2012). Pressure-induced reactivation can lead to seismicity, i.e., earthquakes (White and Foxall, 2016; Rutqvist et al., 2016), which can have severe consequences (Grigoli et al., 2018). Fault slip can also alter the sealing capabilities of the reservoir bounding fault systems. Evaluation of the fault slip tendency, or fault stability, is therefore required to de-risk the Smeaheia Beta site in case:

1. Upwards migration of CO_2 from Alpha or Gamma towards Beta occurs (Fluid pressure)
2. Injection leads to far-reaching fault reactivation and induced seismicity (Dynamic pressure changes)

Fault reactivation or stability is dependent on several geomechanical parameters such as the shear strength of the fault plane (e.g., smoothness or irregularities), the strength properties of the fault rock material and the in-situ stress state. For upper-crustal non-cohesive faults, shear failure is the dominant failure mode (Skurtveit et al., 2018; Montanari et al., 2017). In this work, friction angles of fault rocks from the Øygarden Complex will be determined by the Mohr-Coulomb failure criteria, as this can be used to evaluate fault stability.

The Øygarden Complex juxtaposes the Smeaheia fault block, and we expect the Øygarden Fault System to consist of a mixture of fault rocks derived from both the Øygarden Complex (footwall block) and the sedimentary basin rocks (hanging wall block), Fig. 1B. The Øygarden Complex, a tectonic window west of Bergen, provides an excellent onshore analogue for testing the frictional properties of such crystalline basement fault rock material.

1.2 Aims

We aim to learn more about these fault rocks, and clay-rich fault gouges are of particular interest, as they can be viewed as weak points in fault stability (Tembe et al., 2010). The presence of clay-rich gouges not only accommodates further low friction displacement, but they are also associated with lower permeability which can provide a barrier for fluid flow (Farrell et al., 2021; Chu et al., 1981). We plan to investigate systematic trends in friction angle compared to field-based structural observations, such as orientation, kinematics, and fault core width. In addition, we will compare the friction angle to more conventional geotechnical friction angle strength predictors, i.e., grain size and mineralogical data. The goal is to increase the available friction angle inputs for modelling of fault-bounded reservoirs (e.g., Beta site) that are juxtaposed to crystalline basement rocks (e.g., Øygarden Complex), to further de-risk these potential CO_2 storage sites.

Although many previous studies have conducted direct shear box experiments on natural and synthetic fault gouges and fault rock mixtures (e.g., Dafalla, 2013; Ikari et al., 2009; Alves Da Silva, 2021; Liu et al., 2007; Numelin et al., 2007; Seo et al., 2016), there is still a lack of site-specific data (i.e., the Øygarden Fault System and the Øygarden Complex). In this work, we have sampled fault rocks from the well-documented Lærdal-Gjende fault and six faults from the Øygarden Complex (Fig. 1A). A series of direct shear box experiments at normal stresses from 0.1 to 1.5 MPa were conducted on these natural fault rocks to determine the friction angles at 4 mm shear displacement by using the Mohr-Coulomb failure criteria. Cohesion is highly dependent on the applied normal stress (Montanari et al., 2017; Schellart, 2000); thus, the friction angles were the strength criteria parameter of main interest. Grain size data and mineralogical data were collected by sieving and XRD analysis. The mineralogical composition and thin sections were not initially planned as a part of the thesis, so these data need to be viewed as complementary data.

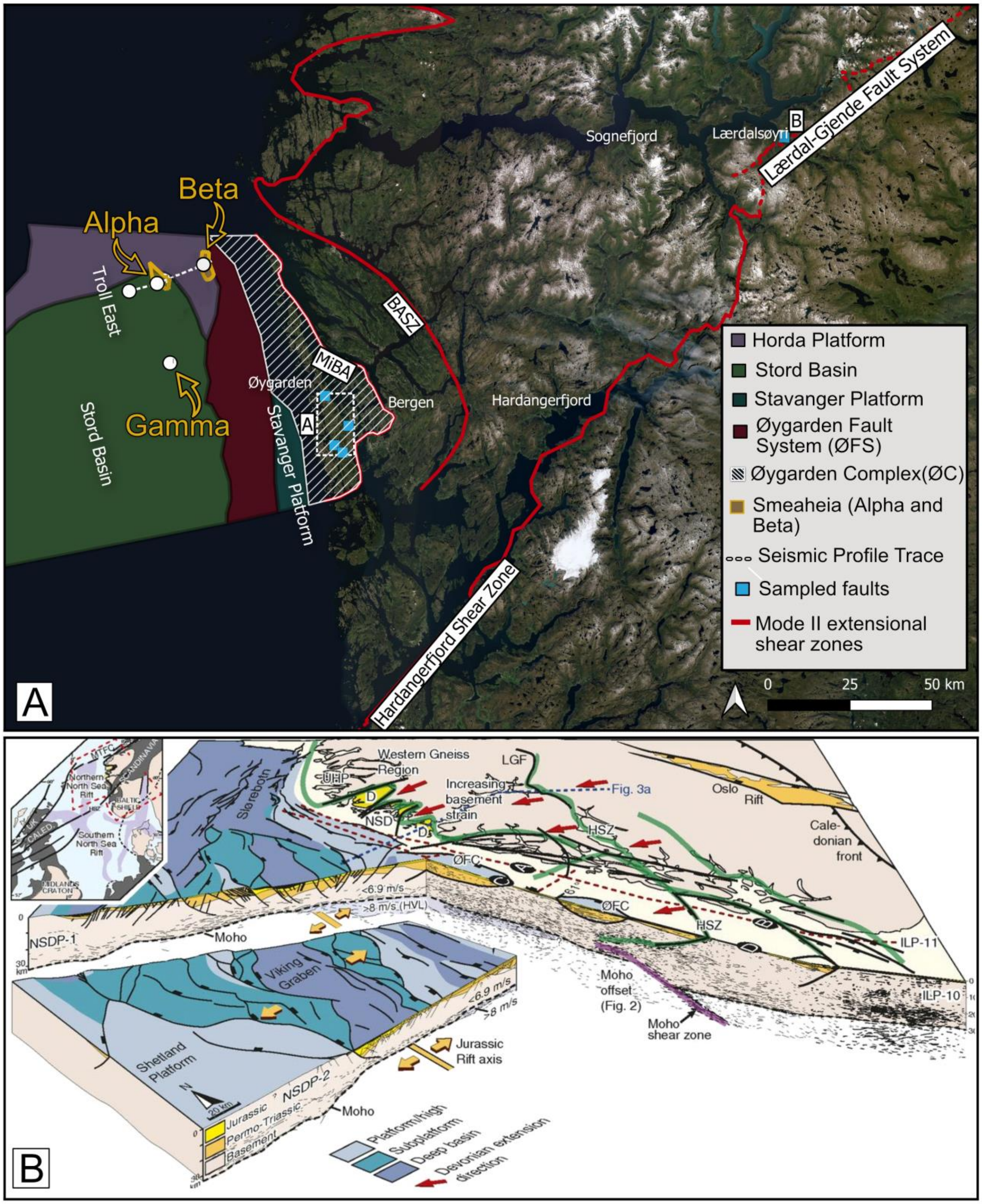

Fig. 1. A) *Map of the study area. The sampled faults from the Øygarden Complex can be seen with blue squares. The crystalline basement rocks of the Øygarden Complex (white dashed area) juxtaposes the Smeaheia Beta storage site (orange) through the Øygarden Fault System. Smeaheia is a tilted fault block at the Horda Platform, and it is bound by the Øygarden Fault System to the east (red field). A seismic profile across the Smeaheia fault block, through the Beta and Alpha sites is shown in Fig. 3.* ***B)*** *Overview of the study area, the northern North-Sea and southwest Norway in cross-sections. The figure is created by (Fossen et al., 2014) based on deep seismic data from 1988.*

2 Regional geology

Post-Caledonian tectonic activity in Norway has predominantly involved multiple extensional phases that have both produced and reactivated large-scale shear zones, faults, and fault systems. These extensional structures have played a significant role in controlling and developing southwest Norway, the onshore and offshore margin, and the North Sea basins (Fig. 1B). An understanding of these extensional phases is essential as it relates to how the fault rocks in the study area were formed and the likelihood of new reactivations and fault activity in the Øygarden Complex.

2.1 The North Sea

The North Sea basin is underlain by a basement of accumulated terrain from the Caledonian and Variscan orogenies (Bell et al., 2014). The Caledonian collapse initiated the multiple extensional phases that developed the North Sea basin and onshore Western Norway (Bell et al., 2014). Crustal-scale extensional shear zones (Mode II extension, Fossen, 2000), such as the Bergen Arc Shear zone (BASZ), Hardangerfjord Shear Zone (HSZ), and Nordfjord-Sogn Detachment (NSD), produced large intermontane Devonian basins that are preserved onshore Norway (Fig. 2a), (Duffy et al., 2015). Two extensional phases have predominantly developed the North Sea basins, i.e., rift phase 1 and rift phase 2 (Bell et al., 2014).

2.1.1 North Sea rift phases

The first phase of extension that developed the North Sea Rift basin is estimated at 261 to 225 Ma, based on dating from sedimentary rocks, fault rocks and magmatic intrusions (Bell et al., 2014). This first phase of extension is believed to be a reactivation of Devonian basement involved shear zones (Mode II extension, Fossen, 2000), which produced N-S striking, westerly dipping faults (Fig. 2b). The N-S striking Vette Fault System and the Øygarden Fault System were formed during this initial rifting phase. Bell et al. (2014) estimate that these N-S trending Permian-Triassic faults have strike lengths of above 100 km and accumulated throws of 4 km.

The second major rift phase is estimated to have occurred during the Middle Jurassic to Early Cretaceous (Fig. 2d-f). The onset of this rift phase was diachronous throughout the North Sea Basin but is estimated at ca. 167 to 170 Ma based on sediment thickness patterns (Bell et al., 2014; and references therein). The initial, middle Jurassic extensional phase was focused in the Viking Graben and a mixture of N-S and NE-SW striking fractures formed (Færseth, 1996; Duffy et al., 2015). This also included reactivation of the N-S striking rift phase 1 faults. The faults were reactivated initially in the Viking Graben before progressing towards the Horda Platform, with a time difference of about 30 Myr (Bell et al., 2014). During the Late Jurassic to Early Cretaceous, the Permian-Triassic rifts were also reactivated in the Horda Platform (Fig.

2e-f). Bell et al. (2014) concluded that the N-S Permian-Triassic faults in the Horda Platform were not reactivated during this initial stage of phase 2 rifting (e.g., the Øygarden Fault System). The cause of the rift initiation and extensional direction is debated, and multiple explanations are suggested. The collapse of a thermal dome, far-field stress fields, and variations in the regional extension direction could have played a role (Bell et al., 2014; and references therein; Duffy et al., 2015).

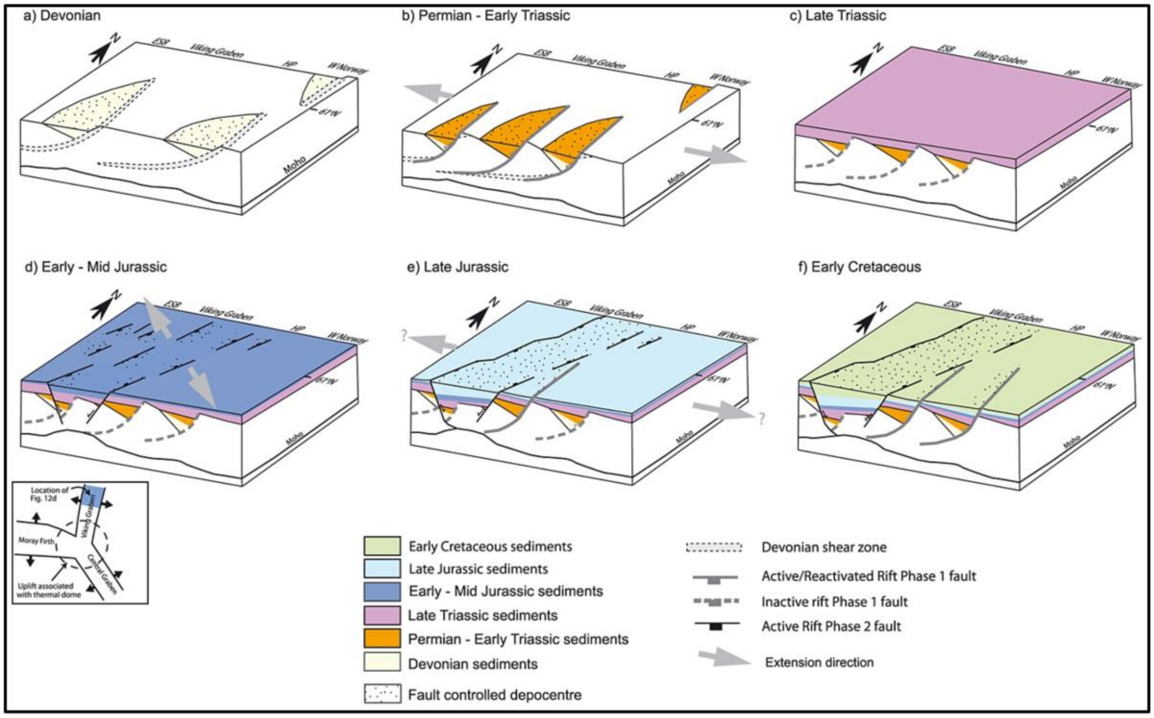

Fig. 2. *Development of the North Sea rift Basin.* ***a)*** *Crustal scale extensional shear zones led to the development of large intermontane basins in the Devonian.* ***b)*** *Onset of phase 1 rifting of the North Sea basin by reactivation of the Devonian shear zones.* ***c)*** *Late Triassic sediments deposited.* ***d-f)*** *Onset of phase 2 rifting in the North Sea Basin occurred diachronous by reactivation of earlier N-S trending faults and development of new SE-NW striking fractures from the Mid Jurassic to Early Cretaceous. Figure from Bell et al. (2014).*

2.1.2 The Horda Platform

The Horda Platform is a N-S elongated structural high, ca. 300 km long and 100 km wide (Mulrooney et al., 2020). The Horda Platform is located along the eastern margin of the northern North Sea (Fig. 3A). It is bound by the N-S trending Viking Graben to the west and the N-S trending Øygarden Fault System to the east. Within the Horda Platform are westward dipping half-grabens bound by basement-involved faults (Mulrooney et al., 2020). This results in a series of rotated fault blocks, such as the Smeaheia site (Fig. 3B).

Smeaheia

The easternmost fault block within the Horda Platform, i.e., the Smeaheia fault block, extends over 70 km north-south (Mulrooney et al., 2020). It is located just east of the Troll West and Troll East fields, and it is bound by the basement-involved N-S striking Vette Fault System (VFS) to the west and the Øygarden Fault System (ØFS) to the east (Fig. 3B). These N-S striking faults are thick-skinned, i.e., they connect to the crystalline basement below the sedimentary rock succession (Mulrooney et al., 2020). The Smeheia block comprises an underlying basement of accreted terrain from the Caledonian and Variscan orogenies (Bell et al., 2014). A series of Permian to Cenozoic sedimentary rocks have been deposited onto this basement during the multiple stages of post-Caledonian rifting (Wu et al., 2021). Amongst them are the Lower to Middle Jurassic aged Viking Group Sandstones (i.e., the potential CO_2 storage reservoir) and the Upper Jurassic to Lower Cretaceous aged Draupne Formation (i.e., top-seal; Wu et al., 2021; Mulrooney et al., 2020).

The Viking Group Sandstones is a structurally trapped reservoir, which is overlain by the top-sealing Draupne Fm. Two of the main sites considered for CO_2 storage are the Alpha and Beta sites (Fig. 3B). The top sealing Draupne Fm is considered a high-quality top-seal for these sites, so cap-rock involved leakage risk is considered low (Wu et al., 2021). Both the Vette Fault System and the Øygarden Fault System have throws of > 300 m at the considered sites (Wu et al., 2021).

Alpha and Beta structures

The Alpha structure is in the western part of the Smeaheia fault block (seismic trace, Fig. 1A). Here the Viking Group Sandstones are juxtaposed to clay-rich and marly rocks from the Draupne and Svarte Formations (Wu et al., 2021). Fluid flow across the Vette Fault System into the adjacent western Troll Field is therefore not considered very likely. Towards the south and north of this seismic line (Fig. 1A), a lower throw of the Vette Fault System means that the Viking Sandstone group are self-juxtaposed (Wu et al., 2021). Risks associated with CO_2 injection into the Alpha site are therefore mainly related to fault reactivation of the Vette and Øygarden fault systems, far-reaching pressure changes, and upwards fluid migration towards the beta structure.

The Beta structure is in the eastern part of the Smeaheia fault block (Fig. 3B). The Beta structure is characterized by a N-S trending fold parallel to the east-bounding Øygarden Fault System. A series of intra-reservoir faults with throws of < 50 m crosscut this structure, interpreted as faults formed during phase 2 rifting (Wu et al., 2021). The Beta structure is juxtaposed to the crystalline basement rocks of the Øygarden Complex and is considered a storage site associated with higher risk. No wells have been drilled into the basement area here, so the laterally sealing properties and the risk of reactivation of the Øygarden Fault System are more uncertain. The Øygarden Fault System have been active further to north up until Holocene (Bell et al., 2014), and more recent seismicity has been recorded in SW Norway and the Northern North Sea area, the latter being related also to post-glacial relaxation (Olesen et al., 2013). Rutqvist et al. (2016) also highlight that faults that juxtapose crystalline basement are more likely to reactivate. Crystalline rocks are more brittle and, therefore, also more susceptible to changes in the stress field and more likely to exhibit stick-slip behaviour that could induce earthquakes.

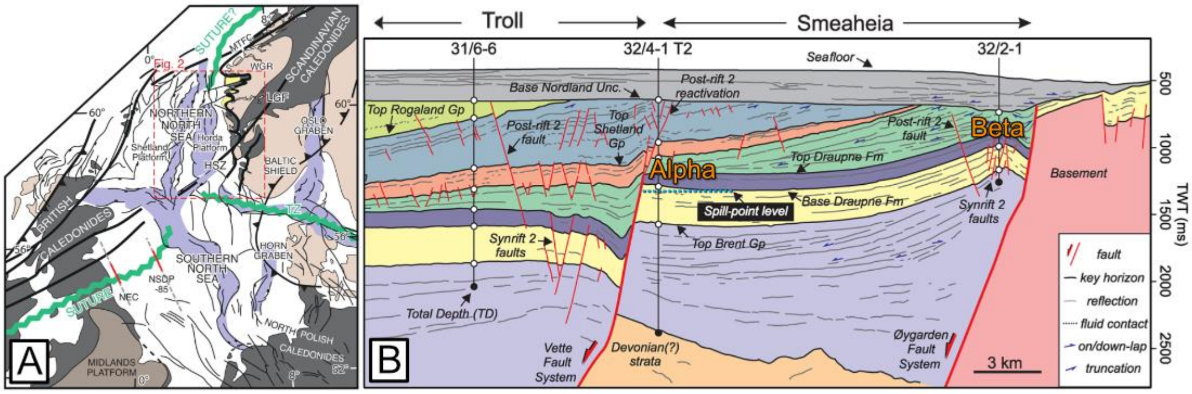

***Fig. 3. A**) Overview of the North Sea Basins and onshore SW Norway from Fossen et al. (2017). **B)** Overview of the Smeaheia seismic profile from well 32/2-1 to 34/4-1. Permian to Devonian sediments (light purple), overlain by the Viking Group Sandstones (yellow). The Viking Group Sandstones are top sealed by the Draupne Formation (dark purple). Above the Draupne Formation are post-rift phase 2 sediments deposited from the Lower Cretaceous to the Cenozoic (green, orange, and blue). Figure modified from Wu et al. (2021).*

2.2 Geology of the study area

2.2.1 The Lærdal-Gjende Fault

Post-Caledonian crustal-scale extensional shear zones (Mode II extension, Fossen, 2000) were reactivated as shallow brittle faults between Late Paleozoic and Mesozoic (Ksienzyk et al., 2016). The Dalsfjord Fault, the Lærdal-Gjende Fault System, and the Fensjord fault reactivated the Nordfjord-Sogn Detachment Zone (NSDZ), the Hardangerfjord Shear Zone (HFSZ), and the Bergen Arc Shear Zone (BASZ), respectively.

The Lærdal-Gjende fault system is a series of NE-SW trending, low angle (ca. 30°), north-westerly dipping detachment faults that separates the pre-Caledonian crystalline basement footwall block, and the middle allocthnonous Jotun Nappe hanging wall block (Fossen and Hurich, 2005). The Lærdal-Gjende fault, which is the most pronounced fault within the Lærdal-Gjende Fault system, is well-exposed just NE of Lærdalsøyri (Fig. 1A). At the Lærdal site, the Lærdal-Gjende fault core comprises a thick asymmetric damage zone (upwards of 200 m thick; Tartaglia et al., 2020) consisting of a thick mylonitic zone. The mylonitic zone was reworked as the Hardangerfjord Shear Zone was reactivated in the shallower brittle regime. This upper-crustal reactivation overprinted the mylonites to produce cataclasites, well-defined fault gouge lenses and clay smear in a highly accessible fault core at Lærdalsøyri (Fig. 1A). Tartaglia et al. (2020) have interpreted the initial brittle faulting of the Lærdal-Gjende fault at ca. 180 Ma with younger reactivations in the Jurassic, Early Cretaceous and Paleogene (ca. 121, 87, 78, and 57 Ma).

2.2.2 The Øygarden Complex

The Bergen Arc System in southwestern Norway consists of a series of Caledonian allochthonous nappes in addition to an underlying parautochthonous basement complex (The Øygarden Complex; Larsen et al., 2003). The Øygarden Complex, a tectonic basement window, makes up the core of the Bergen Arcs and has a mylonitic contact with the minor Bergen Arc Caledonian thrust nappes to the east (Fig. 4). The Øygarden Complex also extends offshore westwards, where it juxtaposes Northern North Sea sedimentary basins, such as the Horda Platform, through the basin-bounding Øygarden Fault System (Fig. 1B, Fig. 3B).

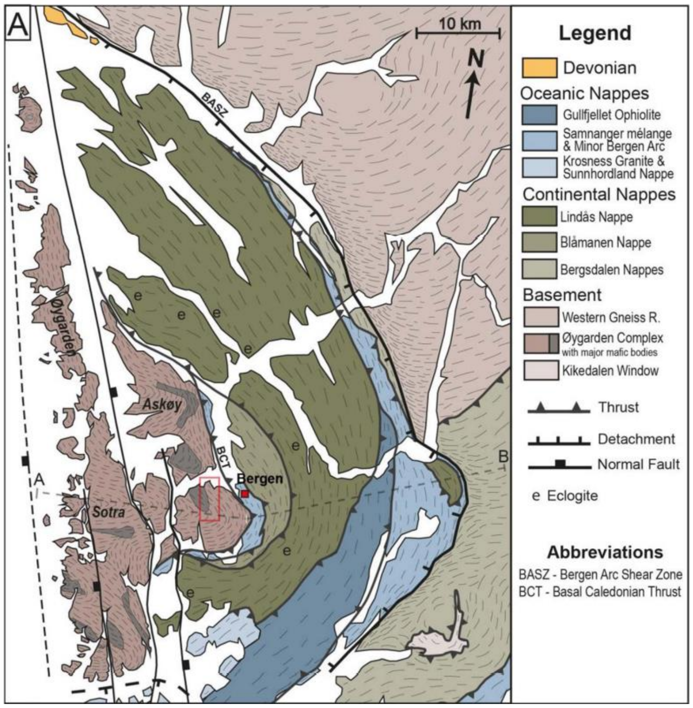

Fig. 4. *The Øygarden Complex, a tectonic basement window forms the core of the Bergen Arc System (BAS). The Øygarden Complex has a mylonitic contact to the Bergen Arc Caledonian thrust nappes. Figure from Wiest et al. (2021).*

The Precambrian basement rocks of the Øygarden Complex consist of rocks from the Telemarkian granitic basement (ca. 1506 +- 5 Ma; Wiest et al., 2020; Wiest et al., 2018), which was intruded by granites and leucogranites during the Sveconorwegian orogeny (ca. 1040 and 1020 Ma). These Precambrian basement rocks were ductily reworked to form granitic-, migmatitic- and tonalitic-gneisses during the Caledonian orogeny and collapse (Larsen et al., 2003; Ksienzyk et al., 2016).

Fault activity and reactivations

The Øygarden Complex was strongly sheared during the post-Caledonian collapse and core-complex exhumation between 405 and 398 Ma (Wiest et al., 2021). It was later subject to multiple stages of brittle faulting and reactivations of pre-existing structures.

The onset of post-Caledonian fault activity, closely related to the initial Caledonian collapse, has been identified by U/Pb dating of sphene mineralization within faults (ca. 396 Ma; Larsen et al., 2003). This first extensional phase produced NE-SW striking normal-faults within the Øygarden Complex, indicative of a regional NW-SE extension. These initial NE-SW striking faults are commonly associated with epidote, quartz, and chlorite mineralization (Øygarden Complex, Set I fractures; Larsen et al., 2003). The set I fractures were later reactivated by a set of N-S striking fractures (Øygarden Complex, Set II fractures;

Larsen et al., 2003), which indicate a regional shift from NW-SE to E-W extension between these phases. The set II fractures typically contain fault plane epidote- and calcite-mineralization, and these N-S striking faults are commonly associated with incohesive and brittle fault rocks (i.e., fault gouge and fault breccia; Larsen et al., 2003). The incohesive and brittle fault rocks have allowed dating of syn-kinematic fault gouges to further fill in the gaps of the phases of reactivation in the Øygarden Complex and SW Norway. Ksienzyk et al. (2016) have identified additional four stages of post-Caledonian tectonic activity in the Bergen Arcs region by the method of K-Ar illite dating of fault gouges in the Øygarden Complex:

1. Post-Caledonian collapse (ca. 396 Ma, Set I fracture)
2. Late Devonian-Early Carboniferous (> 340 Ma, Set II fracture reactivation)
3. Late Carboniferous – Mid Permian (305 – 270 Ma, onset of phase 1 rifting in the North Sea)
4. Late Triassic – Early Jurassic (215 – 180 Ma)
5. Reactivation of faults in the Early Cretaceous (120 – 110 Ma, late phase 1 rifting or initiation of North Atlantic rifting)

The second stage, the Late Carboniferous – Mid Permian reactivation, was interpreted to coincide with the onset of phase 1 rifting in the North Sea (Ksienzyk et al., 2016). The reactivation during the Early Cretaceous rifting was interpreted as a late rifting phase in the North Sea or the initiation of the North Atlantic rifting (Ksienzyk et al., 2016).

3 Fault and fault rock geomechanics

Faults and brittle fault rocks can be a complicated topic with numerous methods that could be applied to describe them and test their various properties. In this chapter we will highlight some key aspects about faults and fault rock materials, and how we can characterize them. This is followed by a more detailed description of fault stability, and how this relates to the frictional properties of granular fault rock materials. Lastly, we will present the principles of direct shear testing, which was the method applied to test the frictional strength of the Øygarden Complex and Lærdal-Gjende fault rocks.

3.1 Faults and fault rocks

Faults

Faults are often thought of as two-dimensional planes cutting through a volume of rock, but in fact, they can be highly complex zones containing fault rocks formed by multiple deformation processes (Fossen, 2016; Faulkner et al., 2010). A typical fault contains a tabular fault core and a surrounding damage zone (Fig. 5) extending into the hanging wall and footwall blocks (Fossen, 2016; Torabi et al., 2020; Faulkner et al., 2010).

The fault core represents the volume of the fault where the highest degree of strain has accumulated, and the damage zone is a zone of lower strain surrounding it (Torabi et al., 2019). In crystalline rocks, the strain is commonly partitioned and localized in high strain lenses, separated by several slip surfaces (Lee and Kim, 2005). This strain partitioning can make fault cores highly heterogeneous and complex, comprising of a multitude of fault rocks. Common fault rock types are fault gouges, fault breccias, cataclasite, mylonites and clay smear, but undeformed host-rock is also often incorporated in the fault core (Torabi et al., 2020).

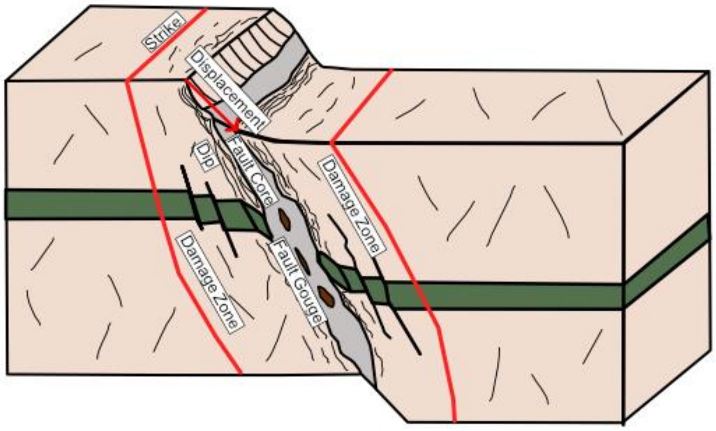

Fig. 5. *Illustration of a normal fault. Surrounding the fault core (grey color) is a damage zone that can extend into the hanging wall block and the footwall block. Most of the deformation is focused within the fault core (grey), and the lenses (brown) represents highly sheared fault rock material such as a fault gouge. Modified from Torabi et al. (2020).*

Incohesive fault rocks

Fault gouges and fault breccias are incohesive fault rocks formed by brittle deformation processes in upper crustal fault zones by comminution (Engelder, 1974; Woodcock and Mort, 2008; Brodie et al., 2007). Granular flow and cataclasis are brittle (-ductile) deformation mechanisms producing shallow brittle fault rocks in the frictional regime.

These processes involve fracturing, rigid-body rotation, and frictional sliding of grains (Engelder, 1974; Fossen, 2016). With increased displacement and accumulated strain in a fault zone, the fault rocks are progressively subjected to grain size reduction by intra-particle fracturing (i.e., grain-splitting) and abrasion at the grain boundaries resulting in a finer-grained material (Henderson et al., 2010; Mair and Abe, 2011). Fault gouge, a fine-grained and incohesive fault rock, can therefore be seen as a fault rock or host rock matured through comminution (i.e., grain size reduction) by fault displacement. In deeper fault or shear zones, frictional processes become less dominant, and the production of fault rocks is increasingly controlled by ductile deformation processes such as neocrystallization and recrystallization (Engelder, 1974).

Fault gouges often form lenses where high strain has occurred, intermingled between fault rocks such as fault breccias (Storti et al., 2003). The fault gouge lenses are not always continuous and are commonly found to be braided or bifurcating within the fault core (Engelder, 1974). Studies on variously coloured fault gouges suggest that colour variations in gouges are primarily controlled by mineralogical composition (Bao et al., 2019). Common clay minerals occurring in fault gouges are chlorite, illite, smectite, kaolinite, and mixed-layer clays (Liu et al., 2007). Fault gouges can also be highly heterogeneous in terms of clay mineralogy, and it is common for gouge material to have incorporated undeformed host-rock fragments (Logan, 1979; Cladouhos, 1999).

Fault rock classification

Sibson (1977) introduced a system of characterizing and classifying fault rocks based on foliation, cohesiveness, and the abundance of visible fragments at the outcrop. Sibson (1977) classified fault breccias and gouges as rocks without primary cohesion.

Woodcock and Mort (2008) argue that it is difficult to determine if the cohesion is primary or not, as fault gouges can be weathered versions of formerly cohesive fault rocks. They also suggest that using grain size determination by sieving methods is a more accurate way to describe incohesive fault rocks (Fig. 6).

In addition, Woodcock and Mort (2008) propose three main subdivisions for fault breccias (i.e., crackle, mosaic, and chaotic breccia), inspired by cave-collapse literature (Loucks, 1999). In their proposed classification:

- Fault gouges are incohesive with < 30 % large clasts < 2 mm
- Fault breccias are incohesive with > 30 % large clasts > 2 mm

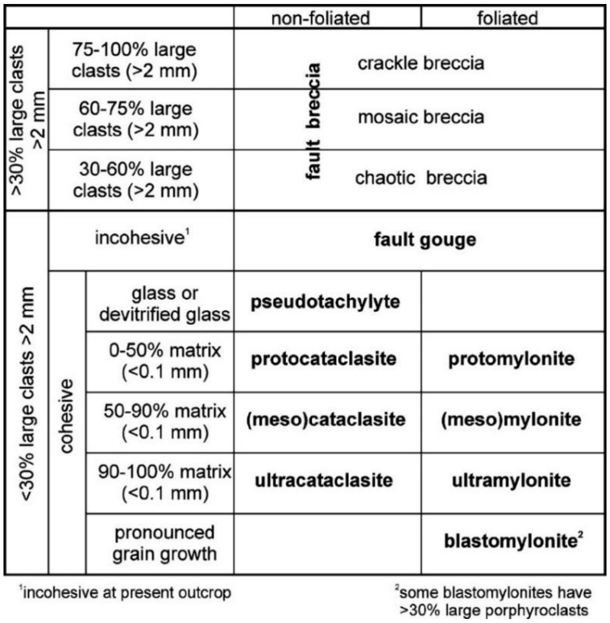

			non-foliated	foliated
>30% large clasts >2 mm		75-100% large clasts (>2 mm)	**fault breccia** crackle breccia	
		60-75% large clasts (>2 mm)	mosaic breccia	
		30-60% large clasts (>2 mm)	chaotic breccia	
<30% large clasts >2 mm	incohesive[1]		**fault gouge**	
	cohesive	glass or devitrified glass	**pseudotachylyte**	
		0-50% matrix (<0.1 mm)	**protocataclasite**	**protomylonite**
		50-90% matrix (<0.1 mm)	**(meso)cataclasite**	**(meso)mylonite**
		90-100% matrix (<0.1 mm)	**ultracataclasite**	**ultramylonite**
		pronounced grain growth		**blastomylonite**[2]

[1] incohesive at present outcrop

[2] some blastomylonites have >30% large porphyroclasts

Fig. 6. *Revised classification of fault rocks from (Woodcock and Mort, 2008).*

3.2 Grain Size Data

Grain size distribution

Grain-size distributions are essential physical parameters for soils and granular materials used to determine the quantities of each particle size within the sample (Bardet, 1997). The grain-size distribution can be found by sieving analysis, where the material is dry- or wet-sieved through sieves with differently sized apertures. The material retained on each sieve represents the total mass of the particle size that corresponds to the previous sieve (i.e., aperture size of the sieved it passed through), and the cumulative weight is added to create the distribution.

Soil grading

Granular fault rock material has many similarities to soils in the geotechnical domain. The principles that apply when classifying a soil can also be applied to describing incohesive fault rock material. In soil mechanics, soil that contains sand and gravel is divided into three types based on the particle size distribution: uniform, well-graded and poorly graded (Bardet, 1997; Lommler, 2012). The soil grading describes how evenly the different particle sizes are distributed.

Well graded materials contain particle sizes that are evenly distributed, which results in a more tightly packed grain configuration and higher density. Poorly graded materials, such as uniformly- or gap-graded materials, are not evenly distributed, resulting in a less tightly packed grain configuration and lower bulk density. Materials are uniformly graded if most of the particles are of the same size, while a gap-graded material has missing particle sizes in the grain-size distribution.

- Well graded soils can become more closely packed, denser, resulting in a higher shear strength
- Poorly graded (i.e., uniformly and gap-graded) soils can become less closely packed, less dense, resulting in a lower shear strength

The soil grading is determined from the grain size distribution curves by the uniformity coefficient (C_u) and the coefficient of curvature (C_c), formula (1) and (2). C_u numerically describes the distribution of the particle sizes, while C_c numerically describes the shape of the grain size distribution curve.

$$C_u = \frac{D_{60}}{D_{10}}$$

(1)

$$C_c = \frac{D_{30}^2}{D_{10}D_{60}}$$

(2)

The D_{10} value corresponds to a particle size in mm, where 10 % of the sample material is finer, and 90 % is coarser (Fig. 7). The D_{10}, D_{30} and D_{60} are found graphically by the intersection of the horizontal lines at the cumulative percentage of weight passing through the sieves. (Fig. 7).

- Soils are well graded when $C_u > 5,\ 1 < C_c < 3$ (Bao et al., 2019)
- Soils are uniformly graded when $C_u, C_c = 1$
- Soils are poorly graded if the first criterion is not met

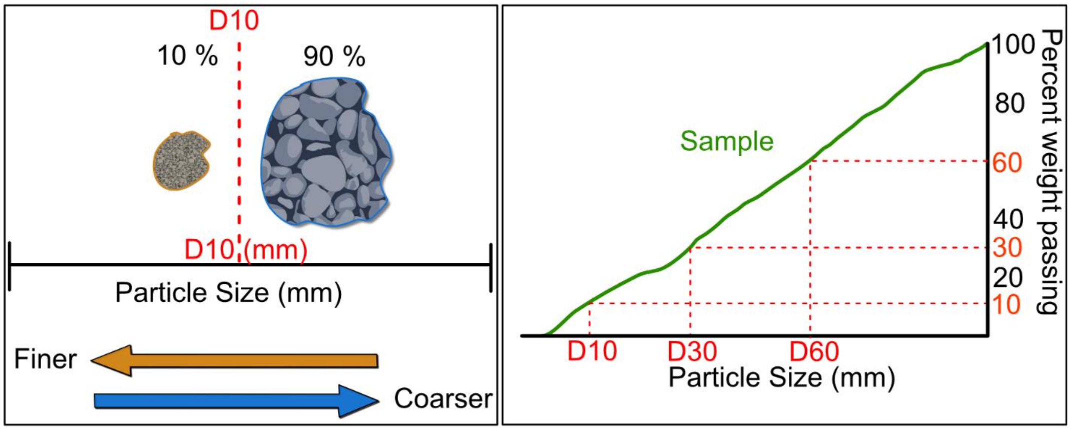

Fig. 7. *Representation of* D_{10}, D_{30} *and* D_{60} *values, which needs to be found for soil grading. D10 is a particle size (mm), which represents where 10 % of the sample is finer and 90 % is coarser.*

Grain- or matrix-supported fault rocks

Brittle fault rocks formed by grain-size reduction due to abrasion and intra-particular fracturing (i.e., grain splitting), are affected by the degree to which these processes dominate. A fault rock formed dominantly by abrasion commonly has a bimodal (i.e., two dominating grain size clusters) particle size distribution and more round particles (Henderson et al., 2010; Mair and Abe, 2011). Smaller particles will be chipped off at the grain boundaries during abrasion, resulting in grain size reduction and a finer-grained matrix. If intra-particle fracturing is the domination grain-size reduction mode, the resulting particles are commonly split into equally sized and more angular particles (Henderson et al., 2010). Mair and Abe (2011) conducted numerical simulation experiments and found that intra-particular fracturing was the dominating grain-size reduction process at higher normal stresses, and at the initial stages of the comminution process. At lower stresses, and as the fault rock was progressively fragmented, abrasion was found to be the dominating process (Mair and Abe, 2011).

Any combination of these two can also occur, which results in a hybrid between these two end members. These three types, i.e., grain-supported (intra-particle fracture), matrix-supported (grain-boundary abrasion) and the hybrid combination, can be identified from the grain size distribution curve (Fig. 8). Distinguishing between these types is important as it is expected that matrix-supported fault rocks will have a lower shear stress resistance than grain-supported fault rocks. However, this also depends on the coarseness of the matrix. The grain-supported fault rock will have a concave (Fig. 8, 1), the matrix-supported a convex (Fig. 8, 4), and the transitional a sigmoidal or linear (Fig. 8, 2 and 3) grain-size distribution curve (Henderson et al., 2010).

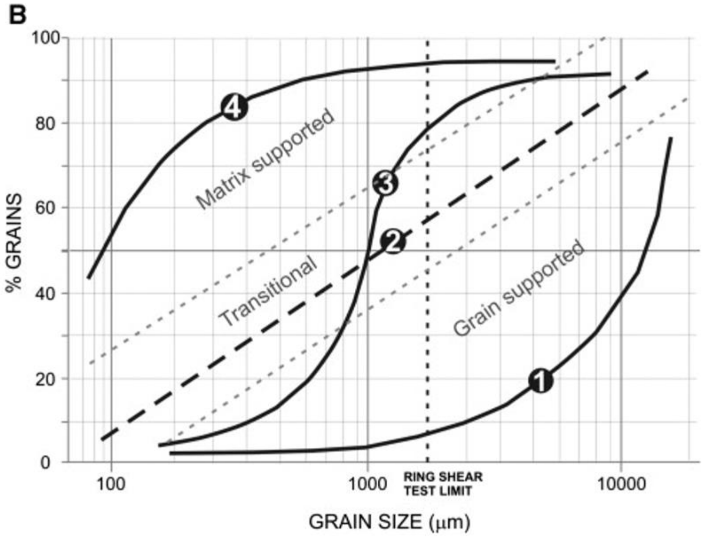

Fig. 8. *Grain-supported fault rock has a concave grain size distribution (**1**). Matrix-supported fault rocks has a convex grain size curve (**4**). The transitional (i.e., a combination of matrix and grain-supported) has either a linear (**2**) or sigmoidal distribution (**3**). Figure from Henderson et al. (2010).*

Fault rock classification by grain size distribution

To classify the fault rocks with Woodcock and Mort (2008) revised fault classification scheme (Fig. 6), the D_{70} particle sizes can be found for the sampled fault rocks. A fault rock can be classified as fault gouge if it is incohesive and if the $D_{70} < 2$ mm (i.e., 70 % of the fault rocks' particles are smaller than 2 mm). If the D_{70} is > 2 mm, the incohesive fault rock is classified as a fault breccia.

- Fault gouges are incohesive with $D_{70} < 2\ mm$
- Fault breccias are incohesive with $D_{70} > 2\ mm$

3.3 Fault stability and fault rock geomechanics

Mohr-Coulomb failure envelope

With increased burial depth or confining pressure, the differential stress required to fracture the rock increases. The relationship between the confining pressure and the differential stress can be described using the Coulomb fracture criterion, formulas (3) and (4). This can be visualized in the Mohr space (Fig. 9). The Coulomb fracture criterion is a linear line that represents the state of critical stress. The slope is given by the coefficient of internal friction (μ), and the cohesion represents the shear strength required to cause failure when no normal stress is applied (i.e., intersection with the y-axis). The fracture criterion depends on the material that is undergoing differential stress and is controlled by the cohesion (C) and the internal angle of friction (ϕ) of the material, formula (4). Different materials will have different values that can be tested experimentally.

The positions and sizes of the Mohr-circles are controlled by the effective normal and shear stresses acting on the material (Fig. 9). The centre of the circle is defined as the mean stress, and the diameter of the circle is defined as the differential stress. If a Mohr-circle intersects the tangential failure envelope, the rock is critically stressed and will fracture at an angle 2θ from the direction of applied normal stress (Fig. 9). The values of σ_1 and σ_3 that produce circles that do not intersect the envelope are referred to as a stable state of stress (Fig. 9). The rock can become unstable and fracture either by altering the stress field, which moves or expands the circle, or by the increase of fluid pressure, which moves the entire circle to the left in the diagram (Fig. 9B-C).

$$\sigma_s = C + {\sigma_n}' \cdot \mu$$

(3)

$$\sigma_s = C + \sigma_n' \cdot \tan(\phi)$$

(4)

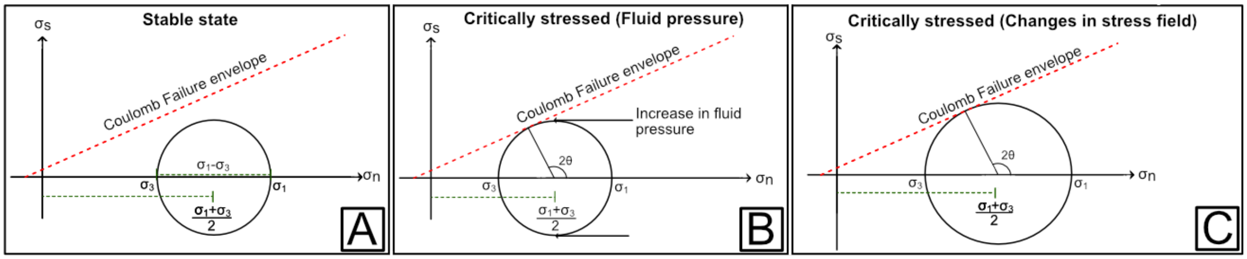

Fig. 9. A) *Stress levels at a stable state, the rock does not reach a critical state of failure.* ***B)*** *Fluid pressure is increased, until the Mohr-circle intersects the failure envelope, causing fracture, which means the material is critically stressed.* ***C)*** *The material is critically stressed due to changes in the stress field, by different values of* σ_1 *and* σ_3 *causing a different radius (differential stress) and different position of the centre of the circle (mean stress).*

Granular material shear strength

The shear strength of granular materials and soils can be expressed using the Mohr-Coulomb (4), although many different failure envelopes could be applied to describe the shear strength. The granular material failure envelope (i.e., C, ϕ) is controlled by the mechanical properties that counteract frictional sliding, rigid-body rotation, and fracturing of grains. The cohesion (C) and internal angle of friction (ϕ) differ from material to material and need to be found through experimentation (Lommler, 2012). Some key factors that can influence the shear strength of granular materials are particle size distribution, particle angularity, particle roughness, the shear strength of individual grains, saturation, drainage conditions, and mineralogy (Marone and Scholz, 1989; Alias et al., 2014; Islam et al., 2019; Ikari et al., 2011; Lommler, 2012).

Fault sealing

The fault rock material is highly important for a reservoir's sealing capacity and integrity in hydrocarbon production or CO_2 storage (Cappa and Rutqvist, 2011). The fault rock can act as a seal or baffle, stopping or delaying fluid flow out of a reservoir. Fine-grained and clay-rich fault gouges found within the fault core are typically less permeable and can reduce the fault's transmissibility (Farrell et al., 2021). However, it is difficult to identify the presence of fault gouges on the seismic scale. Low shear strength clay gouges may increase the likelihood for the fault to slip or reactivate, which can cause earthquakes and ultimately alter the future seal capacity (Fossen, 2016; Cappa and Rutqvist, 2011). Fluid flow across a fault also depends on the relations of the lithological contacts along a fault, such as juxtaposition seal and shale smear seal.

Fault stability and reactivation risk

The stability of a fault or fracture is controlled by the resolved balance of the stresses acting normal to the fault plane and the stresses running along the fault plane (Zoback, 2010; Fossen, 2016). The sum of the stresses acting normal to the fault plane is the effective normal stress ($\sigma_n{}'$), while the sum of the stresses acting parallel to the fault plane is the effective shear stress (σ_s'). The shear and normal stresses are controlled by the in-situ principal stress orientations in relation to the angle of the sliding plane. The relationship between the effective stresses acting on a fault and if the fault will slip is given by the Coulomb failure function (CFF), formula (5). The sliding resistance ($u_f \sigma_n{}'$) counteracts the effective shear stress. If the effective shear stress overcomes the resistance to sliding, the fault will slip. In other words, if the CFF is greater than 0, the fault is unstable and frictional sliding will occur.

- If Coulomb failure function (CFF) > 0, then the fault is unstable (i.e., critically stressed), and slip will occur

The effective stresses can be altered either through changing the in-situ stress field, altering the pore pressure or by differences in mechanical strength properties within the fault. The effective normal stress is proportional to the coefficient of sliding friction. Increasing pore pressure will lower the effective normal stress (6), which lowers the sliding resistance ($u_f \sigma_n{}'$). This means that less effective shear stress is required for frictional sliding when pore pressure is increased. The shear strength properties of the fault rock material can also impact the effective shear stress (σ_s'). A stronger fault rock with higher frictional properties or cohesion counteracts the effective shear stress ($\sigma_s{}'$), which means that higher in-situ shear stress or a lower effective normal stress is required to overcome the sliding resistance.

$$CFF = \sigma_s{}' - \mu_f \sigma_n'$$

(5)

$$\sigma_n' = S_n - p_f$$

(6)

Coefficient of sliding friction

The coefficient of sliding friction (μ_f), which also depend on the fault rock material within the core, can be calculated if the effective shear and normal stresses are known, by the ratio of effective shear stress over normal stress (7). Ikari et al. (2011) found a threshold value for fault gouges of $\mu_f = 0.5$, where clay-rich gouges that had a coefficient of sliding $\mu_f < 0.5$ exhibited a stable sliding behaviour, while stronger fault gouges ($\mu_f \geq 0.5$) experienced both stable slip and unstable slip. This is based on the assumptions that the cohesion contribution of the fault (i.e., pre-existing failure plane) is zero (Ikari et al., 2011). Stable slip does not induce seismicity (aseismic creep), while unstable slip does, through cycles of sudden stress release (i.e., stick-slip).

$$\mu_f = \frac{{\sigma_s}'}{{\sigma_n}'}$$

(7)

3.4 Principles of direct shear testing

Granular fault rocks have many similarities to soils in the geotechnical domain. The experimental methods used to test the shear strength of soils can therefore also be applied to fault rocks. Lenses of fine fault rock material can be tested in direct shear box experiments as an analogue to what stresses a fault rock would experience under natural fault zone conditions (Fig. 10A). Effective normal stress is simulated by applying a vertical load. The effective normal stress is the resolved result of the applied stress and any fluid pressure present within the sample. The effective shear stress, acting parallel to the fault plane, is simulated by displacing one half of the sample horizontally (Fig. 10A). The effective shear stress is the resolved result of the applied horizontal stress (i.e., shear stress) and the material shear strength. As the material is displaced or slip occurs in the fault analogue, granular flow processes occur within the sample to accommodate the applied stresses, resulting in grain reconfiguration (i.e., translation) and grain-size reduction (i.e., grain splitting and abrasion), Fig. 10.

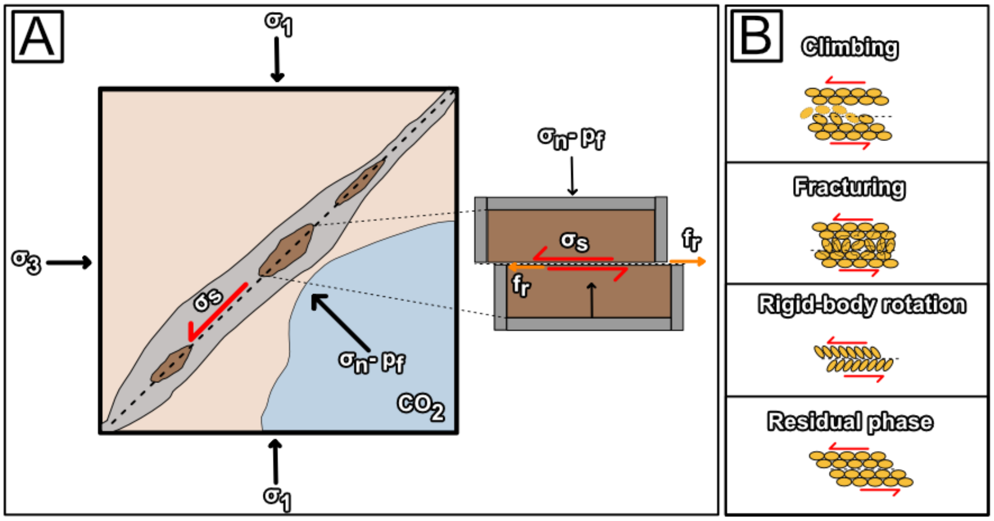

Fig. 10. A) *Shows the relationship between a fault and its fault rocks and the direct shear box experiment. The brown lenses represent a finer grained fault rock, such as a fault gouge that is sampled and tested in a metal shear box. The effective normal stress is found by subtracting the pore pressure caused by a fluid such as injected* CO_2. *Frictional forces resist the shearing force that displaces the fault blocks (red arrow).* ***B)*** *Granular flow processes that occur when the sample is subjected to confining pressure (normal stress) and shear stress. Frictional sliding, fracturing, and rigid body rotation must occur to accommodate the vertical or shear displacement. The residual phase, represents a state where grains have become aligned parallel to the displacement direction, resulting in a lower friction force and less shear stress required for further movement.*

Peak shear strength

The peak strength is found graphically by the material’s shear stress path as the shear displacement (d) increases (Fig. 11). The peak strength is the maximum effective normal and shear stress obtained in ideal brittle materials. This peak value is followed by a phase of strain-softening, where the material has been irreversibly deformed, lowering its future shear strength. This is referred to as a distinct failure, which can easily be identified in the shear stress path of the material (Fig. 11).

Materials do not always display a distinct failure point, and instead, the shear stress increases as strain accumulate (Fig. 11). This is referred to as strain- or work-hardening. Strain hardening can occur in granular materials if grains become interlocked in a way that makes the material temporarily stronger as strain accumulates (Fossen, 2016). This is more likely to occur in coarser materials with angular grains (Li, 2013). Strain hardening can also occur if the applied normal stress is higher than the pre-consolidation, as this suppresses the particles’ ability to re-configure. In such cases, the shear displacement from a direct shear box experiment might not be sufficient to simulate the shear strength needed to overcome this grain-locking, and a subsequent residual phase might not be reached.

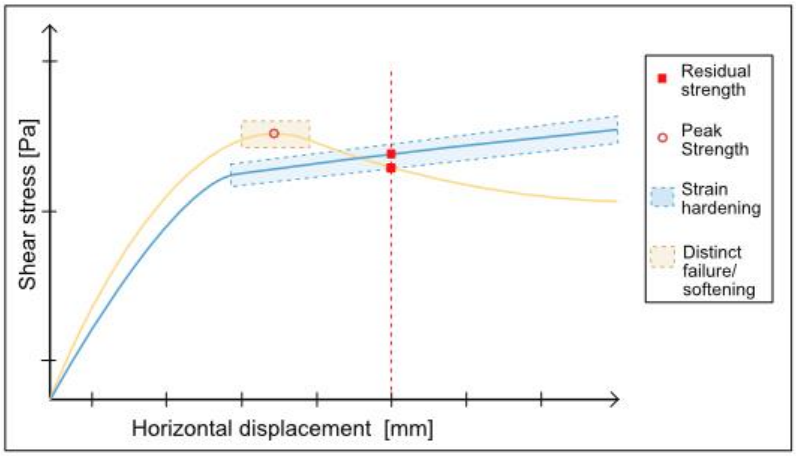

Fig. 11. *Graph used to determine peak yield strength of a material. Horizontal displacement is measured in mm along the x-axis and the shear stress applied to the sample is in Pa. The yellow curve represents a material that has a distinct brittle failure (red circle) at a point of maximum obtained shear stress, followed by a weakened material after failure (strain softening). The blue curve represents a material that does not have a distinct failure point, but instead reaches a phase of ductile strain hardening. A point of residual shear strength (red square) at a specified point of shear displacement (mm) can be used to represent the strength of the material in absence of a distinct peak (red line).*

In the absence of distinct failure, different approaches can be applied to describe the shear strength of the materials. It is common to use the onset of strain hardening, the residual strength, or a value of shear and normal stress obtained after a predetermined shear displacement (mm), Fig. 11. The residual strength for clay-rich gouges is lower compared to coarser materials since the platy clay minerals can align along the shear surface. However, large shear displacements can be necessary to enter a true residual strength phase (Scaringi and Di Maio, 2016).

Drainage

When testing a granular material, it is important that excess pore fluids are dissipated as the sample is deformed either vertically or horizontally by consolidation or shearing (Lommler, 2012; Bardet, 1997). This criterion is ensured by allowing fluids to circulate freely between the sample and the surroundings, i.e., the sample is tested in fully drained conditions, submerged in de-aired water. It is also important that the material is placed in contact with porous and perforated plates, which allows for fluid communication.

Consolidation

It is also crucial that the stresses applied are applied to the grains and not water or air that resides in the pore spaces. Excess porewater and air also alter the fluid pressure, lowering or increasing the effective normal stress applied to the sample. If pore pressure increases, the effective normal stress is reduced, and less shear stress is required to cause failure (Bardet, 1997).

The consolidation process involves applying a compressive force to the material so that the material becomes more densely packed with a grain-supported load configuration. The rate at which the excess pore fluids dissipate as the volume of pore space decreases is called the rate of consolidation. If the container holding the material has rigid walls, such as the direct shear box, the sample can only be compressed in the vertical direction. Change of volume is therefore accommodated by a change in the vertical height of the sample, which alters the available pore space and the density of the material.

Over-consolidation

It is common in soil mechanics to test materials in an over-consolidated state. This generally leads to more well-defined failure curves of the tested material (Li et al., 2017; Vithana et al., 2012). Over-consolidation means that the material has experienced a higher effective normal stress in the past $(maximum\, \sigma_n')$ compared to the current state of stress (current σ_n') formula (8). Over-consolidation is achieved by initially applying higher normal stress to the material before lowering the normal stress to the desired test condition at a pace that allows excess pore pressure to dissipate.

$$OCR = \frac{maximum\, {\sigma_n}'}{current\, {\sigma_n}'}$$

(8)

Shear rate

After the sample is fully consolidated, the shear phase can begin. The shear rate (mm/min) must be slow enough to allow any excess pore pressure to dissipate. The shear rate is usually selected based on the time it took for the sample to consolidate fully. The rate of consolidation, and subsequently the shear rate, depend primarily on the permeability of the material, which is related to the grain size distribution, the initial water content, and types of clays present. The consolidation rate differs from material to material and is found through experimentation.

Linear least square regression

Linear least square regression fits two variables with multiple points (x and y) along a linear line (9). The slope (a) is found by formula (10), while the intercept (b) is found by formula (11). The r value, which represents the correlation between the two variables (x and y), is found by formula (12). By squaring the r value, we get r^2 which represents the amount of variance in x that can be explained by y. An r^2 value closer to 1 represents a strong correlation, while a value closer to 0 represents a weaker correlation.

$$y = ax + b$$

(9)

$$a = \frac{\sum xy - (\sum x \cdot \sum y)}{\sum x^2 - \sum y^2}$$

(10)

$$b = \frac{\sum y - a \cdot \sum x}{n}$$

(11)

$$r = \left(\frac{n \cdot \sum xy - (\sum x \cdot \sum y)}{\sqrt{n \cdot \sum x^2 - (\sum x^2)} \cdot \sqrt{n \cdot \sum y^2 - (\sum y^2)}} \right)$$

(12)

4 Methods

4.1 Field work

The studied faults (i.e., the Lærdal-Gjende and the Øygarden Complex faults) were described in terms of the host rock across both sides of the fault. Structural measurements included fault core width, exposed fault core height or length, the orientation of the faults, kinematics, and host-rock foliation.

Fault kinematics

Fault slip analysis can be a complicated topic, and numerous types of fault plane markers can indicate the relative movement of the host-rock bodies (Doblas et al., 1997; Tjia, 2014). The 'smoothness criterion' has been a common way to determine the sense of fault slip in the past. It is performed by running the hand along slickenside striations and feeling if there is a difference in roughness based on the direction. A positive smoothness indicates the smooth direction, while a negative smoothness is the rougher direction. In step-like fractures, the positive smoothness is the direction that the risers of the steps are facing (Fig. 12, downslope). The striated block has a relative movement in the direction of the negative smoothness, while the missing block moves in the same direction as the positive smoothness. This is an oversimplification of fault slip analysis, and many contradictory examples of the smoothness criterion have been discovered (Tjia, 2014).

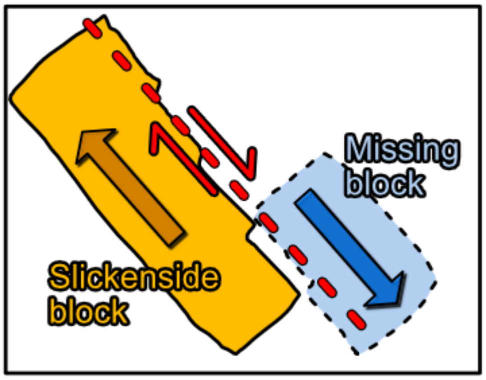

Fig. 12. *Simplified image of slickenside fracture steps to determine fault slip sense. The smoothness criterion can be used to determine relative movement of the blocks. Positive smoothness is achieved by running downslope. A negative smoothness is by running the hand upslope against the direction the risers of the steps are facing. The missing block generally moves in the direction that the risers are facing (Parallel and in the same direction as the positive smoothness direction)*

The selected faults in the Øygarden Complex could have been subjected to multiple reactivation phases (Chapter 2.2.2). The resulting slickensides can be a combination of several episodes of faulting, resulting in complex fault planes where relative movement is hard to identify. Another complication is that kinematic markers on surface-exposed fault planes can be susceptible to weathering and erosion.

Fault rock sampling

Fault rock classification can be challenging in the field. Visible lenses of clay-rich gouge were targeted if present during sampling of the fault rock material. In the absence of clear and distinct clay-gouge lenses, the fault core's weakest and most fine-grained sections were sampled. Weathered and surface-exposed fault rock material was removed prior to sampling. Larger fragments of fault breccia and gravel were purposefully not collected since we were primarily interested in testing the weakest possible material in terms of shear strength. With fault gouge and fault breccia being incohesive at the outcrop, it is challenging to sample these fault rocks in an intact and in-situ configuration. Any foliation, structure, or grain configuration formed by the fault movement, if present, was therefore disturbed during sampling the sampling of these fault rocks.

4.2 Grain size determination

Dry sieving and sedimentation analysis were combined to produce a complete grain size distribution curve. 200 g sample material was removed for dry-sieving to determine the grain-size distribution of the particles ranging from 0.063 mm to the maximum particle size (i.e., sand and gravel). Another 15 g was removed to determine the distribution of particles ranging from 0.063 to the minimum particle size (i.e., silt and clay contents). The silt and clay fractions were determined using the Falling Drop Method (Moum, 1965), developed at the Norwegian Geotechnical Institute (NGI).

Dry sieving

The dry sieving method used is standardised (ASTM-D6913, 2009). The samples were oven-dried at $110°C$ for 24 hours before dry-sieving to record in-situ water content. The materials were washed in a 0.063 mm sized sieve to remove any particles of the clay and silt fractions (< 0.063 mm). The sand and gravel fractions caught by the sieve were dried again (24h, 110°C) to remove the water content. The corresponding weight loss is the total weight of the silt and clay fractions. The dried samples were placed into a shaking tower for 15 min with sieve apertures from 16 mm to 0.063 mm. Each sieve with the materials was weighed to record the cumulative weight of the materials passing.

Falling Drop Method

The falling drop method (Moum, 1965) for determining the clay and silt grain size distribution was performed by accredited lab technicians at the Norwegian Geotechnical Institute (NGI), Oslo. A shortened version of the falling drop method is explained here.

The falling drop samples (ca. 15 g) were placed into a pyrophosphate solution. The material was kept in the solution overnight to dissolve aggregates of silt and clay prior to sieving (Fig. 13A). The falling drop samples were then sieved using a 0.063 mm sieve to remove particles larger than 0.063 mm. The remaining silt and clay solution were then poured into test tubes. The test tubes were placed into the sedimentation vessel (Fig. 13B). to acclimate and reach the same temperature as the anisole (organic liquid), at ca. 25°C. A silt and clay mixture drop were placed into the sedimentation vessel using a calibrated pipette (Fig. 13C). The time it takes for the drop of silt and clay mixture to travel from point A to point B is used to determine the velocity. The velocity depends on the proportion of clay to silt, which is found by Stoke's Law for sedimentation.

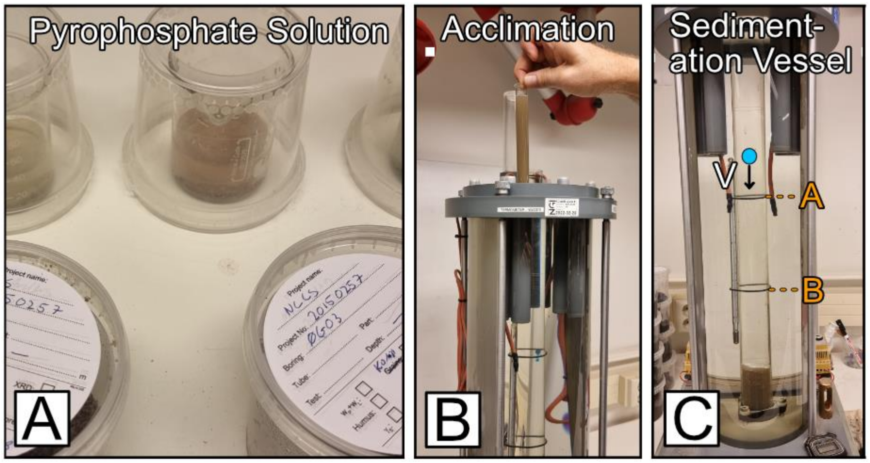

Fig. 13. *Falling drop method for clay and silt content determination.* ***A)*** *The samples were placed into a pyrophosphate solution overnight to dissolve the clay and silt fragments.* ***B)*** *The dissolved samples were placed into test tubes and inserted into slots at the top of the sedimentation vessel to acclimate to the correct temperature.* ***C)*** *A calibrated pipette is used to insert a single and constantly sized drop of the clay and silt mixture into the sedimentation vessel. The time it takes for the drop to travel from point A to point B is recorded. The velocity of the drop is found by the time recorded and the distance travelled. This velocity depends on the relative amounts of clay and silt of the solution (Stoke's Law).*

4.3 Mineralogical data

Powdered bulk XRD

The samples were crushed into a fine powder using an agate mortar and pestle. The samples were placed onto glass squares before being placed into a Bruker D8 advance at the University of Bergen. A bulk sediment program was selected, with a scanning range (2θ) from 5 to 70. The scan time for each sample was 30 minutes. Diffrac.EVA and Profex were used to identify the mineral phases, and semi-quantification of the identified phases was performed in Profex by Rietveld Refinement (Doebelin and Kleeberg, 2015), see Appendix 4.

Powdered Clay XRD

The Millipore vacuum method was used to separate the finer fractions of the samples for clay analysis. The samples were mixed with water and allowed to settle for around 20 minutes, which allows for sedimentation of the particles. The liquid containing the suspended finer particles was then carefully poured into a container with a 0.2 μm filter at the bottom. A vacuum was created by connecting a tube to a water outlet and letting the water flow through it. The liquid containing the fine powder was then forced through the filter by the vacuum, and the finer fractions were caught by the filter. After the suspended liquid had gone through the filter, the filter was removed, and the finer material from the filter was scraped off and placed onto a glass square. With the samples prepared, the clay analysis could be performed. Phyllosilicate minerals can be susceptible to glycol and heat treatment, either by swelling or being destroyed, which can be observed in the resulting XRD patterns (Ali et al., 2022). This makes for a more straightforward determination of the constituent clay minerals. The following four steps were performed on the clay powder fraction:

1) Air drying
2) Glycol
3) Heat treatment in oven at 350 $°C$
4) Heat treatment in oven at 550 $°C$

After each step, the clay fractions were placed into a Bruker D8 advance, with a scanning range (2θ) from 5 to 25, with a scan time of 30 minutes for each sample. The resulting diffraction data were plotted (Appendix 4) and adjusted using quartz (d = 4.26 Å) as a reference. The clay minerals were identified using various reference articles (Ali et al., 2022; and references therein). The following steps sum up how the clay (-phyllosilicate) minerals were identified:

- Smectite group minerals swell when glycol is added, which produces distinct peaks at d = 8.42 and 5.59 Å
- Kaolinite has a strong peak at = 7.16 Å that gets destroyed by heating to 550$°C$
- Chlorite has a strong peak at d = 7.07 Å that gets destroyed by heating to 550$°C$
- Kaolinite and chlorite can be distinguished in bulk XRD patterns
- Illite has distinct peaks at d = 10 Å and 5.53 Å that remains unaltered

Thin sections

Thin sections were prepared at the University of Bergen (UiB) to complement the XRD data, make qualitative observations about grain angularity and determine if clay minerals appeared as aggregates. Not all prepared thin sections were successful, as loose material flaked off during polishing to approximately 30 μm thickness.

4.4 Direct shear test

4.4.1 Equipment and test setup

The equipment used for shear testing was a VJ tech Pro Static Simple and Direct Shear System, located at the Schmertmann Research Laboratory (SRL) at the Norwegian Geotechnical Institute (NGI). The shear box is connected to Clisp studio software by VJ tech, used for soil and rock testing, allowing easy configuration of the experiments and extraction of the continuously recorded data. The shear box consists of two calibrated load cells and two displacement transducers (Fig. 14).

The metal shear box consists of bottom and top parts that can move horizontally relative to each other (Fig. 15A). This metal box holds the sample in place and controls the shearing within the sample along the pre-determined shear plane (Fig. 15B). The sample is mounted between the perforated plates, porous stones and the base plate and loading pad (Fig. 15B). The porous and perforated plates allow fluid communication between the sample and the surrounding water chamber.

When the sample is mounted, two red pins are used to tighten the bottom and top parts of the shear box, and the shear box device is placed inside the direct shear box equipment (Fig. 15A). The grey pins are used to create a gap between the metal components when shearing the material to reduce metal-to-metal friction between the two halves of the shear box (Fig. 15A).

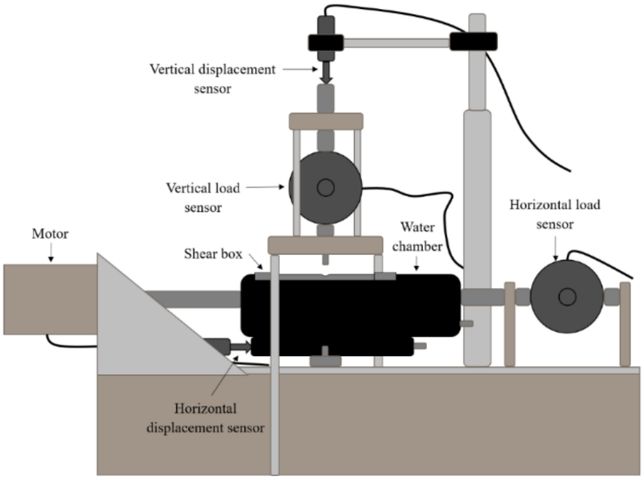

Fig. 14. *Sketch of the direct shear box device that was used. The shear box is mounted in a water chamber, which is filled with water during the consolidation stage to shear the samples fully saturated. Figure from Alves Da Silva (2021).*

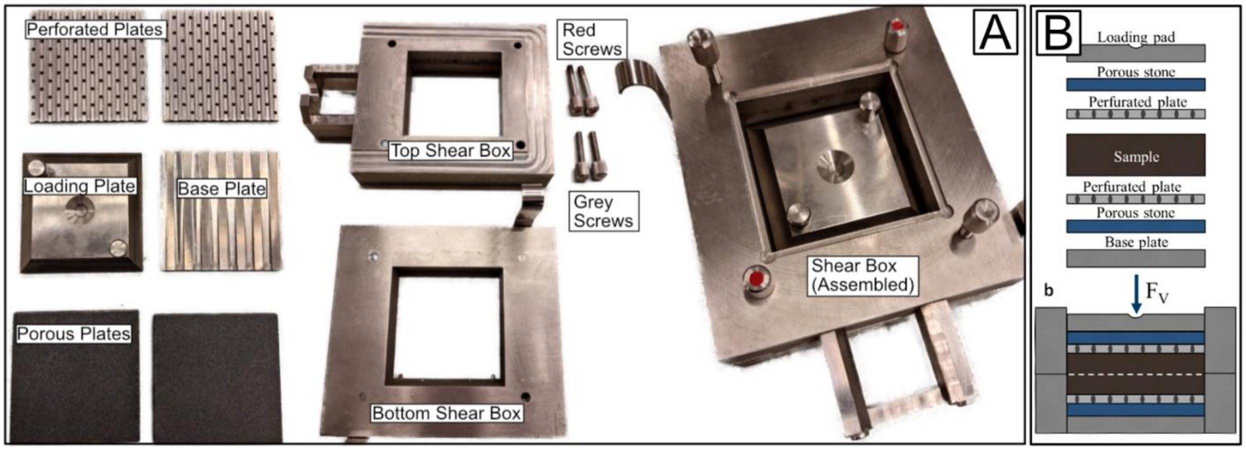

Fig. 15. A) *Overview of the individual components and the assembled shear box****.*** ***B)*** *Schematic representation of how the sample is mounted within the shear box. The predetermined shear plane is shown with a white dashed line. The sample is placed between perforated plates and porous stones to allow communication of fluids between the sample and the surrounding water chamber. Figure B is from Alves Da Silva (2021).*

Normal stress

A vertical force (F_{vrt}) is applied to the top of the sample through the loading pad to consolidate and test the sample at different normal stresses. The applied vertical force and the vertical displacement change are continuously measured by a vertical load sensor and a vertical displacement sensor. The applied normal stress (σ_n) is given by the vertical force (F_{vrt}) divided by the area of the base or top of the sample (13). The area where the vertical force (F_{vrt}) is applied will change throughout the experiment as a function of the shear displacement (d). We assume that fluid pressure (p_f) is negligible by selecting a shear rate lower than the dissipation rate of excess fluids. The effective normal stress (σ_n') is therefore given as,

$$\sigma_n' = \frac{F_{vrt}}{s \cdot (s - d)}$$

(13)

where s is the initial side length of the sample (70 mm). Only one side of the box will reduce its length as the shear displacement (d) increases, corrected by subtracting the shear displacement (d). This correction is performed after the experiments to get the effective normal stress (σ_n').

Shear stress

The horizontal force (F_{hrz}) is applied to the sample by displacing the lower half of the shear box. The upper half stays fixed and is attached to the horizontal load sensor, which measures the applied horizontal load force (N). The applied shear stress (σ_s) can be calculated using the measured horizontal load force (F_{hrz}) and the surface area, which is calculated by the samples side surface (14). However, the applied shear stress is continuously recorded in the VJ studio software and does not need to be corrected as the shear displacement increases. The shear displacement (d), i.e., how much the upper half moves relative to the lower half, is measured by the horizontal displacement sensor.

$$\sigma_s = \frac{F_{hrz}}{s \cdot h}$$

(14)

4.4.2 Direct shear test procedure

Each experiment took approximately 24 hours to complete, and 30 direct shear box experiments were performed. A more detailed version of the development of the direct shear box method used in this thesis can be seen in Alves Da Silva (2021). The direct shear procedure performed on each fault rock sample can be summed up in these steps:

1) Sample preparation
2) Mounting the sample (1 hour)
3) Consolidation (19 hours)
4) Shearing (4 hours)
5) Post Shear (1 hour)
6) Failure envelopes

Sample preparation

The fault rock samples were dried in the oven at $110°C$ for 24 hours (Fig. 16A). The maximum recommended particle size for a direct shear box test was 1/6 of the sample height (ASTM-D3080, 2011). The recommended sample height with this specific shear box setup was approximately 20 mm, which allowed a maximum particle size of 3.33 mm. No sieve with a size between 4 mm and 2 mm was available; thus, the samples were sieved only using a 4 mm sieve to avoid losing additional material. The dried fault rock samples were gently broken up to break up solidified clay and silt particles using a mortar and pestle (Fig. 16B) and sieved at 4 mm. The weight of the lost particles of sizes > 4 mm was recorded (Appendix 1, Fig. 16C).

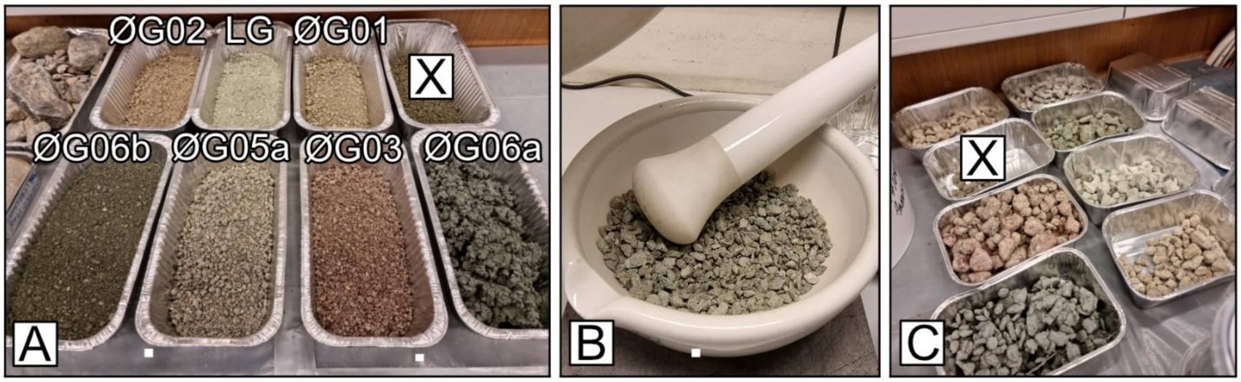

Fig. 16. *Sample preparation and dry sieving.* ***A)*** *The 7 fault rock samples were oven-dried at 110° for 24 hours. One fault sample was removed as it did not have enough material for more than 1 test, marked by an X.* ***B)*** *The slightly hardened samples were gently crushed to avoid sample loss due to aggregation of finer material.* ***C)*** *The particles larger than 4 mm was sieved and weighed.*

Mounting the samples

The shear box was assembled and placed within the direct shear box water container (Fig. 18A-B). Each test required approximately 200 g of dry weight material. The samples were mixed with water and stirred to achieve a homogeneous sample and ease the mounting process. Clay-rich samples can be difficult to work with, so more water was added to the clayey samples to limit material loss, achieve homogeneous mixtures, and even mounting of the samples. Initial water content varied from 10 to 30 % across the samples (Appendix 1). The wet samples were then put into the direct shear box container (Fig. 18, C), and their initial wet weight was recorded. The samples were compressed by tapping with a metal rod (Fig. 18D). The heights of the samples were recorded, and the initial sample densities could be calculated.

Consolidation and time of consolidation

After the sample was mounted (Fig. 18E), the load device was engaged, which applied a normal stress to the sample. After two minutes of applied vertical force, the water container was filled with de-aired water to achieve drained conditions. The samples were consolidated at normal stresses $\sigma_n = 0.1, 0.3, 0.5, 1.0, 1.5\ MPa$. The 0.5, 1.0, 1.5 MPa normal stress states were prioritized where material was lacking (Appendix 1). The fault rock samples were consolidated by incremental loading (30 minutes) and over-consolidated to a higher normal stress than used for shearing (Fig. 17). The samples were kept at the over-consolidation stage for 15 hours before being lowered in increments (30 minutes) to the normal stress used for the test for an additional 3 hours (Fig. 17).

The highest normal stress that could be applied was 1.75 MPa, which limited the achievable over-consolidation ratio. Over-consolidation ratios (OCR) used for the upper normal stresses (0.5 to 1.5 MPa) were 3.5, 1.75 and 1.17. For the lower normal stresses (0.1 to 0.5 MPa), the OCR was kept constant at 3.5 (see Appendix 1). The time of consolidation can be found by the relationship between the applied vertical load and the corresponding vertical displacement (i.e., compression) in the sample as a function of time.

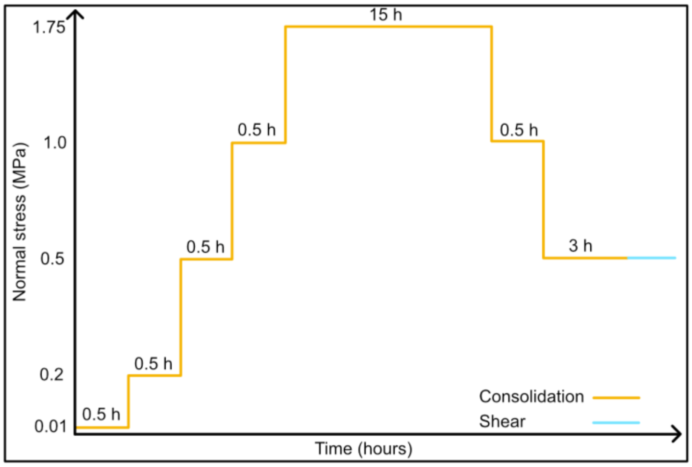

Fig. 17. *Example of the incremental consolidation stages for a sample sheared at 0.5 MPa normal stress, including an over-consolidation stage at 1.75 MPa normal stress.*

Two different methods can determine the consolidation rate, the log-time or the square root of time methods (Bardet, 1997). The fault rock samples were mostly sand-dominated and low in clay, and consolidation times were considered fast. Consolidation data from Alves Da Silva (2021) was used to estimate the time of consolidation for the studied fault rock samples based on the samples sand content. A conservative 15 hours at the over-consolidation step was chosen and kept constant throughout all experiments.

Shearing and shear rate

After the consolidation phase, the horizontal shear displacement was initiated by applying a horizontal force (Fig. 18E). The shear rates were chosen qualitatively based on the results of Alves Da Silva (2021), who had shear rates ranging from 0.003 mm/min (100 % clay) to 0.3 mm/min (100 % sand). An intermediate value of 0.03 mm/min was selected for the studied fault rocks, based on the contents of sand. The two red pins were removed to allow the halves of the metal shear box to move relative to each other. The two grey pins were tightened slightly to avoid metal-to-metal friction along the sliding surface.

Post-shear

After the shearing phase was completed, the water was drained from the water chamber. The horizontal and vertical load and displacement sensors were disconnected, and the entire metal shear box was removed from the water container. The metal shear box was weighed post-shear to determine any change in mass due to the experiment. The wet sample (Fig. 18F) was weighed and placed into an oven to dry at 110°C overnight. The shear box and the components were carefully cleaned and prepared for the next experiment. The dried sample was weighed the next day (Fig. 18G), and the water content and final density could be determined post-shear.

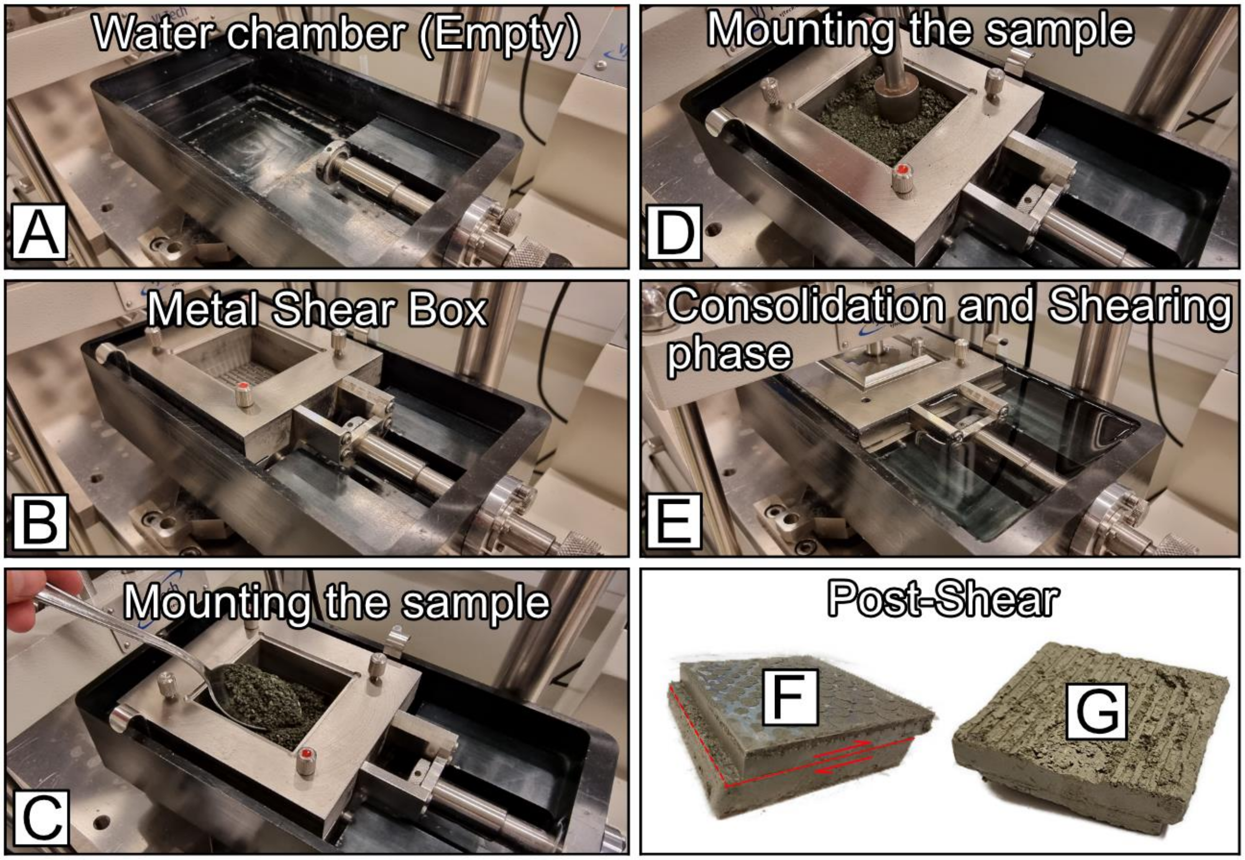

Fig. 18. *Stepwise description of the direct shear box experiment.* ***A)*** *The water chamber is emptied and cleaned before mounting a new sample.* ***B)*** *The metal shear box is assembled and placed into the water chamber.* ***C)*** *The sample is placed into the metal shear box.* ***D)*** *The sample is gently compressed by tapping with a metal rod.* ***E)*** *Consolidation is started by applying a vertical load to the sample. After 2 minutes, the water chamber is filled with deaired and deionized water to fully submerge the sample. The shearing phase is initiated when the sample is consolidated.* ***F)*** *The samples are weighed both wet and dry, post-shear, to determine the final water content.*

Failure envelopes (Mohr-Coulomb)

Thirty direct shear box experiments were conducted for the fault rock material after removing the particles larger than 4 mm (Appendix 1). The obtained normal- and shear-stress at 4 mm shear displacement (d) was used to determine the peak strength values for each test (Fig. 11). These peak strengths will be referred to as the residual strength at 4 mm shear displacement, although proper residual strength conditions were not achieved for all samples with the low shear displacements involved (see chapter 3.4).

Each fault rock was tested across several normal stresses (0.1 to 1.5 MPa), which produced 2 to 5 peaks (normal stress, shear stress), depending on available sample material (Appendix 1). The residual cohesion (C_r) and residual coefficient of internal friction (μ_r) were found by fitting a linear least-square error regression to the peak points for each fault rock (see chapter 3.3). The cohesion (C_r) value was found by the intersection of the linear failure envelope with the y-axis, and the angle of internal friction (ϕ_r) was found by $\tan^{-1}(\mu_r)$, where μ_r is the slope of the resulting linear curve.

Coefficient of sliding friction

The coefficients of sliding (μ_f) were calculated using formula (7), by using the recorded effective shear stress and effective normal stress ratio at 4 mm shear displacement (d) for the 1.5 MPa normal stress test per fault rock sample. The fluid pressure was assumed to be negligible due to the slow shearing rate (0.03 mm/min).

5 Results

This chapter is divided into three main sections. In the first section, every fault is structurally described in terms of fault anatomy, tectonic units, structures, and fault core. This is followed by the fault rock grain size data, mineralogy, and friction angles. Lastly, these different parameters are compared and correlated to the resulting friction angles from the Øygarden Complex fault rocks.

5.1 Faults

The locations of the studied faults are presented in Fig. 19, and the 7 studied faults (i.e., the Lærdal-Gjende fault and Øygarden Complex faults) are summarized in Table 1. See Fig. 1 for how the fault locations relates to the Øygarden Fault System. The most recent reactivation of the Lærdal-Gjende fault was ca. 57 Ma (Tartaglia et al., 2020). The ØG06a fault was active in late Jurassic – Jurassic ca. 215 to 180 Ma (Ksienzyk et al., 2016), while the most recent dated reactivation that produced fault gouges in the Øygarden Complex was in the Early Cretaceous, ca. 120 to 110 Ma (Ksienzyk et al., 2016).

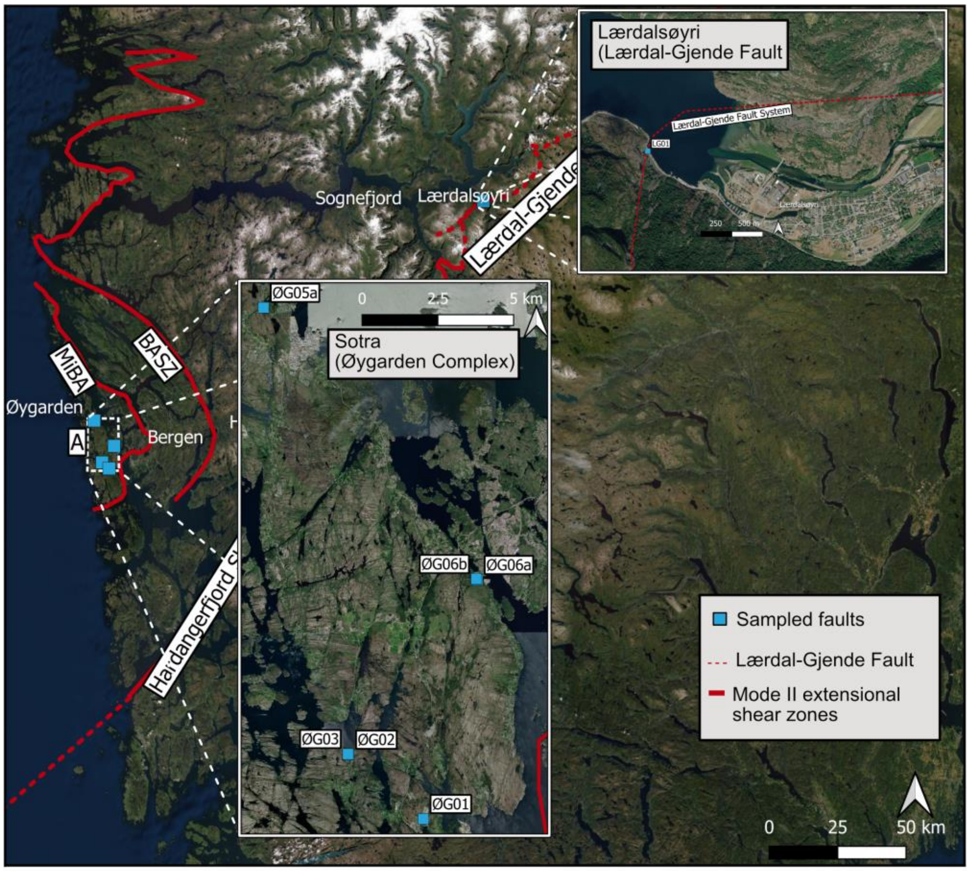

Fig. 19. *Overview of the sample locations from Lærdalsøyri (i.e., the Lærdal-Gjende fault, northeast), and Sotra (i.e., the Øygarden Complex, west).*

Table 1. *Summary of all sampled faults from the Øygarden Complex and the Lærdal-Gjende fault. Faults or locations notated with (1) are based on the faults and locations from (Ksienzyk et al., 2016). Orientations of the faults are given in azimuthal strike/dip notation, using the right-hand rule. The dip direction is in brackets. The weight of the sampled fault rock material is the remaining weight after 4 mm sieving and grain-size determination.*

Sample	Location	EU89 lat/lon	Strike/ Dip	Host rock	Sample Weight (kg)	Description	Fault activity
LG	Lærdalsøyri	61°06'11.9"N 7°27'22.8"E 61.103307, 7.456328	250/30 (NNW)	Footwall: Granitic Gneisses of the pre-caledonian basement. Hanging wall: Jotun Nappe Complex	1.65	Tunnel roadcut northwest of Lærdalsøyri, Sogn and Fjordane; 8 meter wide fault, 1 m wide fault core with green clay gouge, red clay gouge, clay smear and green cataclasite.	121, 87, 78, and 57 Ma
ØG01	Hald Stadion	60°16'18.9"N 5°04'44.0"E 60.271913, 5.078900	035/62 (ESE)	Tonalitic to granitic gneisses. Gneissic banding dipping gently towards WNW. Amphibolites in hanging wall block	0.50	Fault located at northeastern corner of Hald Football stadion, Sotra; 11 m wide fault, 0.5 m wide fault core with fault breccia and lenses of grey clay gouge.	-
ØG02	Kallestadvika	60°17'26.8"N 5°02'04.2"E 60.290774, 5.034492	174/82 (W)	Granitic orthogneiss, with medium to coarse grained distinctive red k-feldspar crystals. Slightly pegmatitic.	0.58	Road cut near boat harbor, Kallestadvika, Sotra; 7 m wide fault, 0.6 m wide fault core with brecciated euhedral calcite, fault breccia and intermingled grey clay gouge	-
ØG03		60°17'27.5"N 5°02'02.8"E 60.290983, 5.034100	168/80 (W)		0.93	Fault under rock net, 25 m NW of ØG02, Kallestadvika, Sotra; 12 m wide fault, 2.90 m wide fault core with large blocks of fault breccia and red to grey clay gouge	
ØG05a	Vindesnesvegen, Olsvika	60°25'20.9"N 4°59'01.2"E, 60.422475, 4.983655	320/76 (NE)	Granitic gneiss with gnessic banding dipping gently towards NW	0.97	Parking area at Olsvika Båthavn, Sotra; 2.5 m wide fault, 10 cm wide fault core with fault breccia and grey clay gouge	-
ØG06a	Døsjeneset	60°20'32.4"N 5°06'40.4"E 60.342339, 5.111214	022/84 (ESE)	Banded and migmatitic granitic gneiss from the Øygarden Complex (Kziensyk, A, 2016)	1.05	Quarry near marina at Døsjeneset, Sotra; 10 m wide fault, 2.60 m wide fault core with fault breccia and lenses of green to grey clay gouge.	215 to 180 Ma
ØG06b		60°20'33.6"N 5°06'37.7"E 60.342671, 5.110466	352/83 (E)	Granitic to granodioritic gneisses with red k-feldspar. Rich in amphibole and biotite.	1.99	Fault at quarry, 50 m NW of ØG06a, Døsjeneset, Sotra; 14 m wide fault, 2 m wide fault core with fault breccia and green, sandy fault rock material.	-

5.1.1 Lærdalsøyri, Lærdal (LG)

The Lærdal-Gjende fault is well exposed just northwest of Lærdalsøyri, a small town near the south-easternmost arm of the Sognefjord (Fig. 20). The boundaries of the fault core were mostly visible, and the width of the core was approximately 1 meter. The fault core was surrounded by an asymmetric damage zone, extending about 200 meters from the fault core (Tartaglia et al., 2020). The LG fault itself has a WSW to ENE trend and dips moderately towards NNW.

The footwall block host-rock is a part of the pre-Caledonian crystalline basement which mainly comprises granitic- to migmatitic-gneisses. The hanging wall block consists of mangerites, jotunites and gabbros from the Jotun Nappe Complex (Fig. 20). The footwall block and the hanging wall block are separated by a thick mylonitic zone, which were reworked by brittle-ductile to brittle processes during active periods of the LG fault. Green and grey cataclasites were found across both sides of the fault near the fault core, but the cataclasites were more abundant in the hanging wall block. The hanging wall block was also crosscut by quartz and epidote veins (Tartaglia et al., 2020).

A wide variety of fault rocks were found within the LG fault core. The principal slip surface (red dashed line, Fig. 20) was characterized by a thin (2-3 mm) clay smear that ran along it. Several other slip surfaces were identified above and below the main slip surface. A weakly foliated green gouge surrounded the clay smeared principal slip surface (Fig. 21B). In some sections, it had formed sigmoidal lenses, which indicated a top to the NW extensional shear sense (Fig. 21A). Lenses of reddish gouge were identified, embedded within the weakly foliated green gouge. The reddish gouge was hardened and crosscut by zeolite veins (Tartaglia et al., 2020) that ran parallel to the principal slip surface (Fig. 21B). Normal Riedel fractures crosscut the reddish gouge roughly 50° from the slip surface (Fig. 21B). A representative gouge sample close to the clay smear along the principal slip surface was targeted. The sample contained two parts, collected from the sigmoidal green gouge lens (Fig. 21A) and along the clay smear (Fig. 21B). The sample has been mixed to provide enough material for testing, which means that these two different areas' grain sizes and mineralogy have been distorted. The overall composition and mineralogy still represent the average gouge material closer to the principal slip surface.

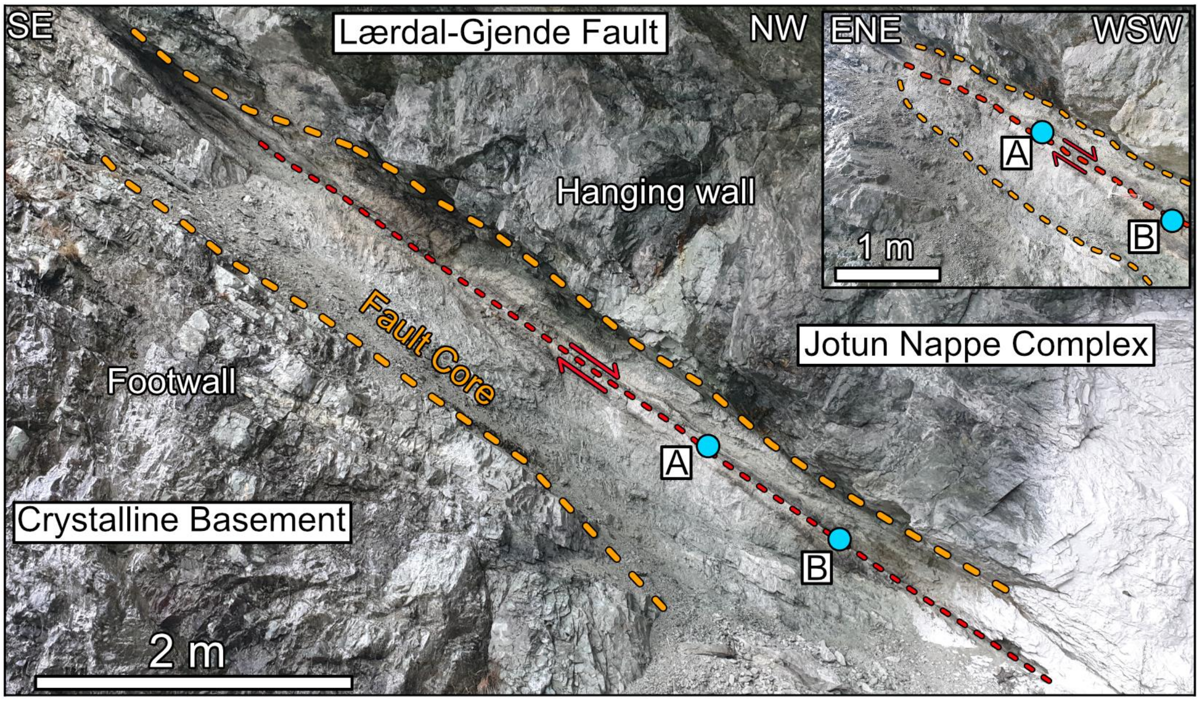

Fig. 20. *Field photograph of the well-exposed Lærdal-Gjende fault near Lærdalsøyri, Sogn and Fjordane. The exposed fault core length is about 8 meters long, and the maximum width of the fault core (dashed orange lines) is around 1 m. Several slip surfaces are identified within the fault core, but the principal slip surface is marked with a dashed red line. The footwall block is a heavily damaged (mylonitic) granite, with gneissic augens, while the hanging wall block consists of mylonites and cataclasites derived from mangerites, jotunites and gabbros of the Jotunite Nappe Complex. The fault core itself contains a wide variety of fault rocks from green cataclasites, green gouges, red gouges, and clay smear. Sampled locations are marked with blue dots, point A and B.*

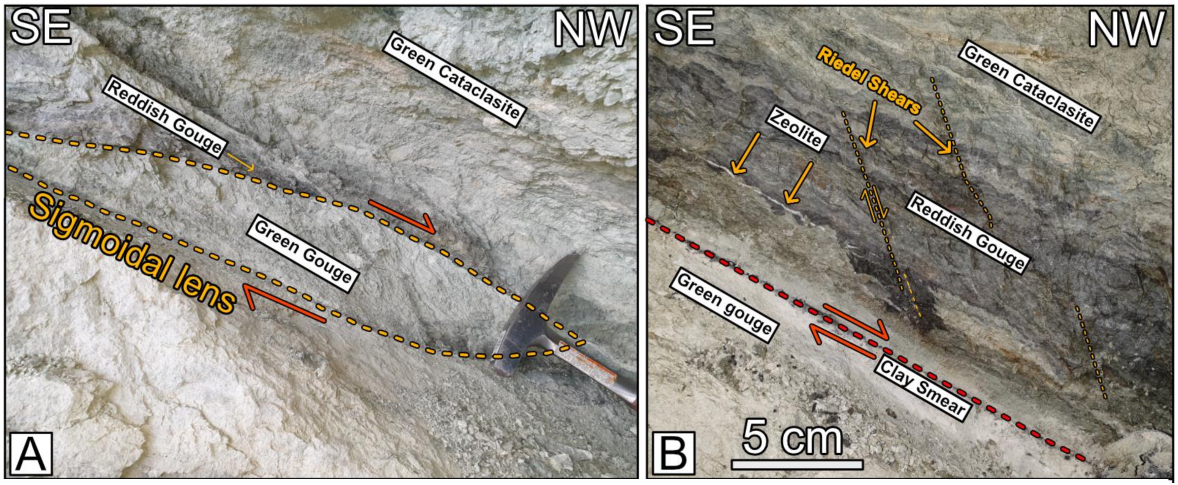

Fig. 21. A) *Sigmoidal green gouge lens, with a top-to-the-NW extensional shear sense. Surrounding the lens is a reddish gouge and green cataclasites.* ***B)*** *Principal slip surface (red dashed line). A thin layer (2-3 mm) of clay smear runs along the principal slip surface and is surrounded by green gouges. Above we find a reddish gouge which is crosscut by normal riedel shear fractures, which again is overlain by the green cataclasite. Zeolite veins running parallel to the principal slip-surface were identified by Tartaglia et al. (2020).*

5.1.2 Hald Stadion, Sotra (ØG01)

The ØG01 fault is well exposed at Hald Stadion football field, located just North-West of the small town of Skogsvåg, Sotra (Fig. 22). The fault is NE-SW trending and dips steeply towards the SE. The fault cuts through a body of tonalitic to granitic gneiss. The gneissic banding had a NNE-SSW trend, dipping gently towards ESE. There was a slight change in orientation of the S-fabric across the fault, with the dip direction changing from ESE to SES when crossing the fault W-E. The boundaries of the fault core were visible, and the core had a maximum width of 0.5 m, and a length of 11 m (Fig. 22).

The surrounding host rock on both sides of the fault was crosscut by numerous steep N-S striking and E-W striking fractures (Fig. 22). These smaller fractures were found within the entire exposed rock wall, which ran along the entire length of the football field (approximately 100 meters). A steeply W-dipping N-S trending fault was identified on the western surface of the footwall block (Fig. 23B). This fault plane was covered by a calcite-mineralized step slickenside (Fig. 23B). The striations plunged steeply and parallel to the fault plane, and the risers of the steps were facing downwards. This positive smoothness downwards indicates that an adjoining and missing western block has moved down relative to the footwall block. This also suggests that the western footwall block of the ØG01 fault has moved up relative to the eastern hanging wall block (Fig. 23C), but no other clear kinematic indicators within the fault or fault core were identified.

The fault core was mostly dominated by fault breccia (Fig. 23A) and proto-cataclasites. Brecciated fragments identified within the core did not contain the distinct gneissose foliation but instead consisted of angular porphyroclasts of red K-feldspar (1-2 mm) in a darker amphibolitic matrix. The amphibolitic matrix made up over 50 % of the rock volume of these host-rock fragments. This could indicate that the fault rock has undergone cataclastic processes in the ductile-brittle transition zone before forming brittle fault breccia and gouge. In the centre of the fault core, anastomosing lenses of grey clay-rich material were identified (Fig. 23A). The fault core was highly weathered, and an abundance of organic material such as soil and roots were also present. The sample was retrieved from the clay-rich lens (Fig. 23A).

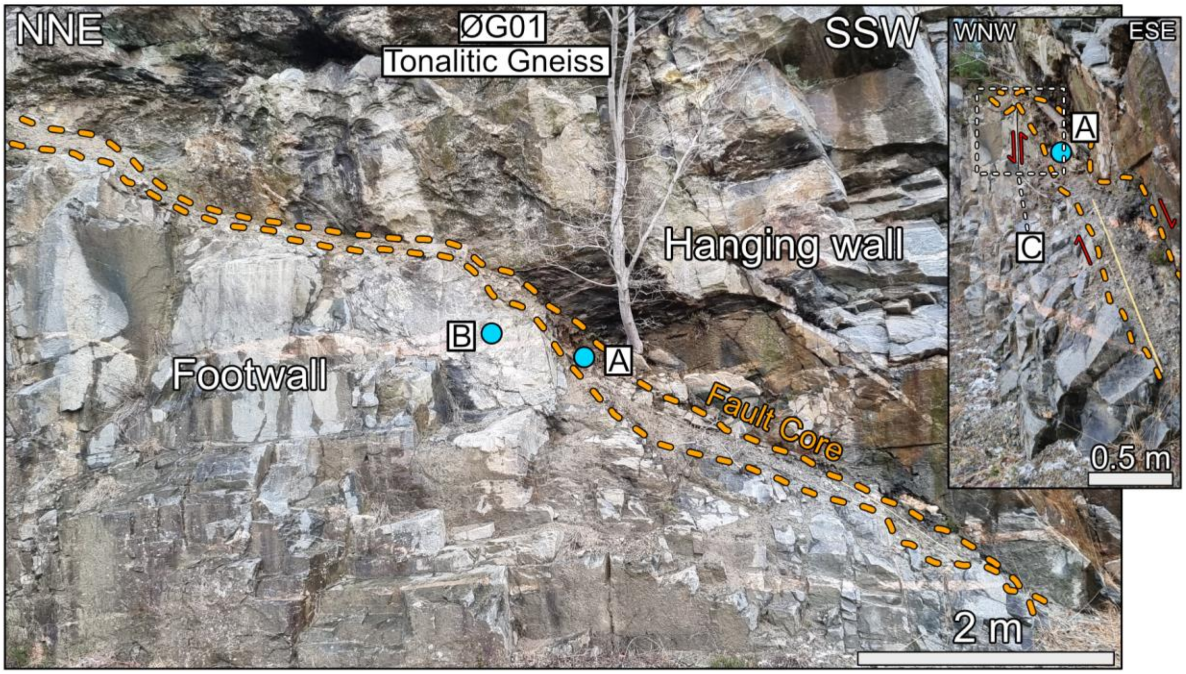

Fig. 22. *Photographs of ØG01 fault, located at Hald Stadion, Sotra. The exposed fault core (dashed orange line) is approximately 11 m long, and 0.5 m wide at its maximum. The host rock across both sides of the fault is tonalitic gneiss, but the hanging wall block is also amphibolitic in certain places. Points of interest is marked in blue, where A marks the sample location.*

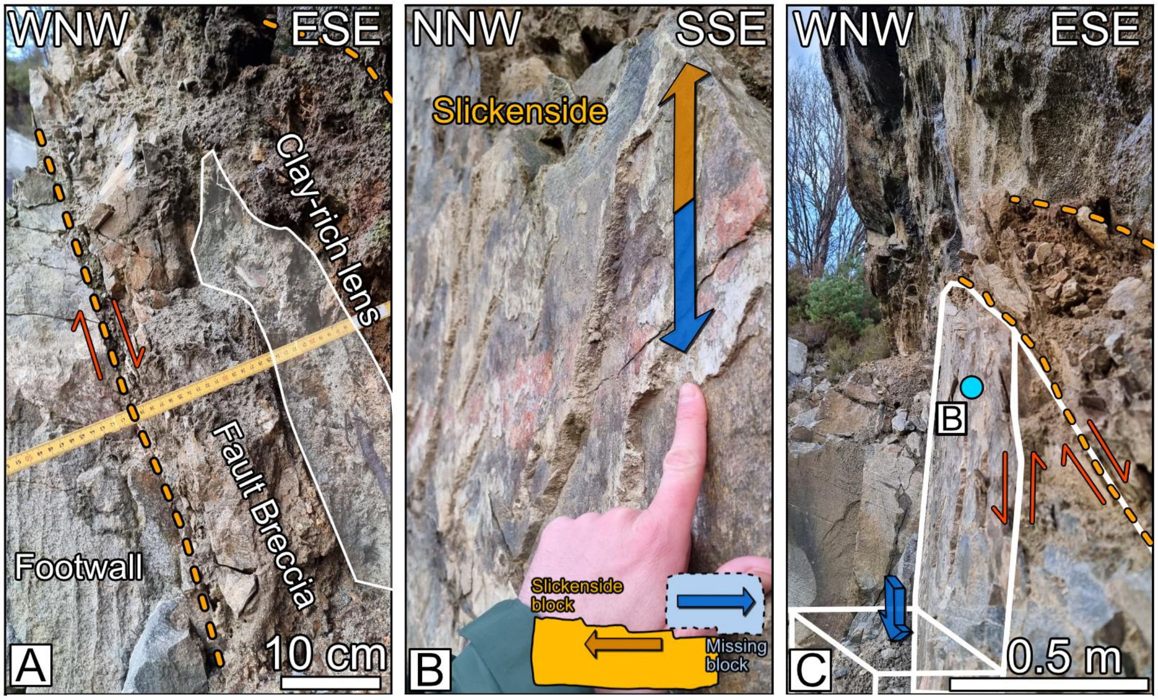

Fig. 23. A) *Clay-rich grey gouge lens is surrounded by fault breccia and cataclasite.* ***B)*** *Step slickenside is identified. The risers of the steps are pointing downwards. This indicates that the footwall block has moved up relative to a missing western block (white box,* ***C****), and up relative to the hanging wall block.* ***C)*** *The fault that displaced the missing western block can be interpreted as a conjugate Riedel shear of the larger ØG01 fault.*

5.1.3 Kallestadvika, Sotra (ØG02)

The ØG02 fault is located near a boat harbour at Kallestadvika, Sotra (Fig. 24). The fault is N-S trending and dips steeply towards the W. The host rock in the hanging wall block and footwall block was a granitic orthogneiss. The host rock had medium- to coarse-grained red K-feldspar augens, and it appeared to be slightly pegmatitic. The fault core had a maximum width of 0.6 m, and the height of the exposed fault core was 7 m.

A step slickenside covered the surface of the footwall block (west, Fig. 24) with calcite and chlorite mineralization (Fig. 25B). The striations plunged steeply and had a pitch close to 90 degrees, parallel to the fault plane. The risers of the steps were polished and did not protrude much, meaning that relative movement was more difficult to determine. The risers of the steps appeared to be pointing downwards. This positive smoothness downwards indicates a relative downwards movement of the eastern hanging wall block and that the ØG02 fault has a component of reverse dip-slip displacement. Another fault was identified on the outside surface of the eastern hanging wall block (Fig. 24). This fault dips steeply towards the E, and step slickenside mineralization identified on the fault plane indicates a reverse dip-slip displacement. Two sets of sub-vertical dipping minor fractures were surrounding the fault core in the hanging wall block. One set was parallel to the fault itself, while the other set ran perpendicular to the first set, resulting in a blocky and jointed damage zone surrounding the fault.

Within the 0.6 m wide fault core, multiple veins consisting of subhedral coarse-grained calcite were identified (Fig. 25A). They appeared slightly brecciated, and varyingly sized fragments of the host rock were enclosed within the calcite veins. This could suggest a weakened or brecciated zone prior to the formation of the calcite veins. Another possibility is that the fragments were enclosed within the calcite during hydrothermal fracturing. A sudden stress release caused by fluids can cause the host rock to fragment without the need for significant displacement of the fault (Phillips, 1972; Larsen et al., 2003). However, the large veins of calcite indicate that they must have formed at a time when there was open void space for the calcite to grow. The remaining parts of the fault core mainly consisted of larger and intact blocks of host-rock towards the top and middle sections. In the lowermost meter, fault breccia with grain sizes ranging from 20 cm to 7 cm was identified. Smaller gravel to clay-sized particles was intermingled between the brecciated fault rock and calcite. It was challenging to establish if the intermingled material resulted from secondary weathering or if it was an original component of the fault. The sample was retrieved towards the lower parts of the fault, beneath a weathered calcite vein (Fig. 25C).

Fig. 24. *Field photographs of the ØG02 fault, located at Kallestadvika, Sotra. The exposed fault core (dashed orange line) was approximately 7 m high and 0.6 m wide at its maximum. The host-rock across both sides of the fault is granitic orthogneiss. Coarse to medium grained red K-feldspar crystals were present within the host-rock. Large euhedral calcite veins were found within the fault core, in addition to fault breccia with particle sizes ranging from 30 cm to gravel sized fragments (2 mm). Fault gouge material was intermingled within the larger fragments of fault breccia and was concentrated near the calcite vein at point C, where the sample was retrieved. Points of interest is marked with blue dots.*

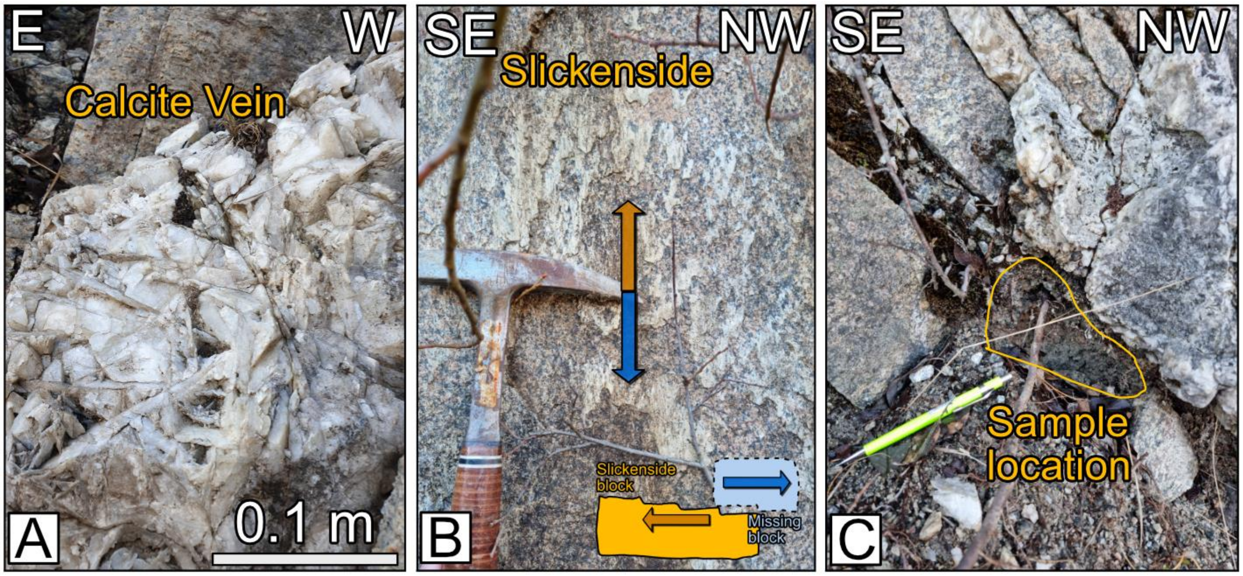

Fig. 25. A) *A large vein of euhedral and brecciated calcite was identified.* ***B)*** *Step slickenside with calcite and chlorite mineralization on the hanging wall block (western block Fig. 24). The risers of the steps were pointing downwards. This indicates that there has been dip-slip (reverse) displacement of the ØG02 fault.* ***C)*** *Sample location is outlined.*

5.1.4 Kallestadvika, Sotra (ØG03)

Located just 25 m NW of the ØG02 fault is the larger sized ØG03 fault at Kallestadvika, Sotra (Fig. 26). The fault is N-S trending and dips steeply towards the W. The host rock across both sides of the fault is a granitic orthogneiss, with medium- to coarse-grained red K-feldspar augens. The exposed fault core is 2.90 m wide at its maximum and was exposed over a height of approximately 12 m.

Two sets of N-S and E-W striking sub-vertical faults were crosscutting the host rock resulting in a blocky damage zone surrounding the fault core. On the rock surface of the western hanging wall block, a step slickenside with calcite and epidote mineralization was identified (Fig. 27C). The striations plunged steeply with a near-vertical pitch parallel to the fault plane. The risers of the steps were in some sections of the fault plane polished and smooth, but more protruding steps were identified close to the fault core (Fig. 27B-C). The risers of the steps pointed downwards. This positive smoothness downwards indicates that the western hanging wall block has moved up relative to the eastern block and that the ØG03 fault has had a component of reverse dip-slip displacement.

The fault core of the ØG03 fault mainly consisted of brecciated fault rock. The narrow top section of the fault core consisted mainly of larger elongated blocks of intact host rock (upwards to 80 cm long). These large blocks were aligned almost parallel to the fault core. In the lower parts of the fault, the brecciated fault rocks were smaller, ranging from the large 80 cm blocks of intact host rock to gravel-sized fragments. Anastomosing lenses of finer grey material (4-10 cm thick) were intermingled between the fault breccia were observed (Fig. 27A-B). The fault gouge had a red iron-stained colour. The iron staining also covered the surfaces of the host rocks across both sides of the fault. The sample was collected from the red-and grey-gouge lenses (Fig. 27A-B).

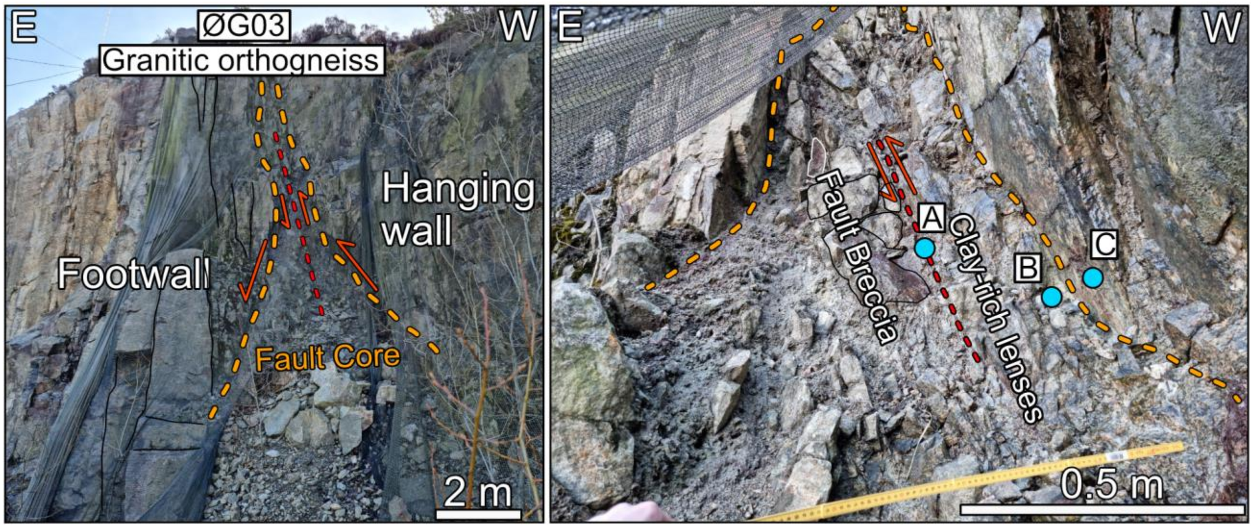

Fig. 26. *Field photographs of the ØG03 fault, located 25 m NW of the ØG02 fault, at Kallestadvika, Sotra. The fault core (dashed orange line) was 2.90 m wide at its maximum and was 12 m high. The fault itself was covered by a rock-net, making observations from a distance more difficult. The fault core (picture on the right) consisted of a wide zone of large (80 cm) elongated to gravel-sized brecciated fault rock. In between the fault breccia, lenses of grey clay gouge with red iron-staining were identified. Points of interest is marked with blue dots.*

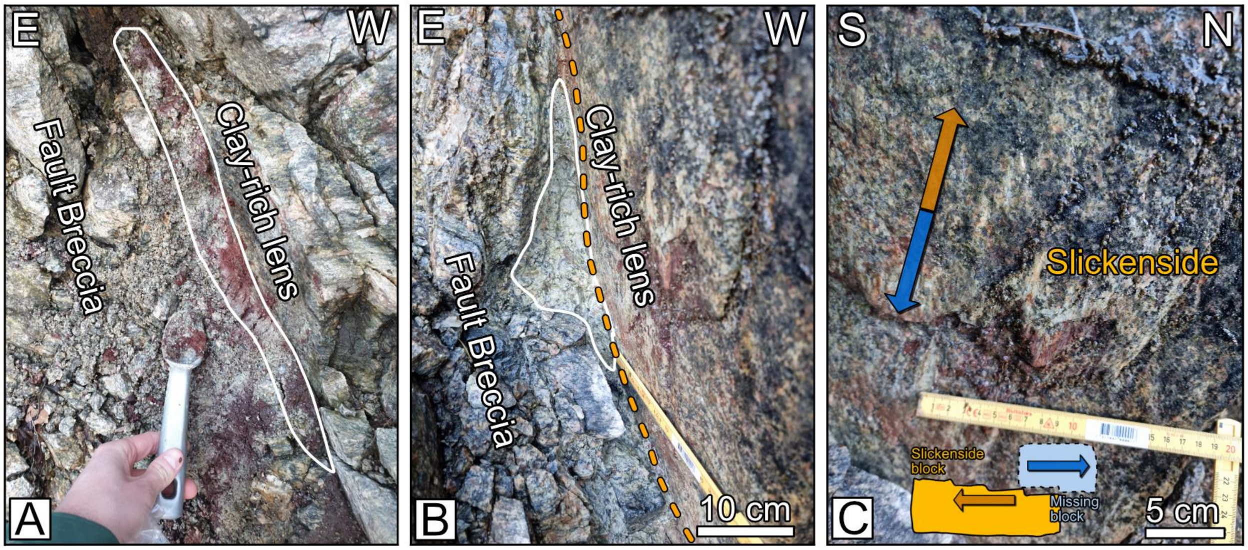

Fig. 27. A*) Grey clay-rich lens with red iron-staining, situated towards the centre of the fault core, between brecciated fault rocks.* ***B)*** *Another clay-rich lens was identified, situated between the footwall rock surface, and brecciated fault rock. The sample was taken from both the clay-rich lenses from* ***A)*** *and* ***B)****.* ***C)*** *Step slickenside mineralization was observed. The risers of the steps were pointing downwards. This indicates that the ØG03 fault has had a component of reverse dip-slip displacement.*

5.1.5 Vindesnes, Sotra (ØG05a)

The ØG05a fault is located at a parking area for the Olsvika boat harbour at Vindesnes, Sotra (Fig. 28). Ksienzyk et al. (2016) described a fault from this location in their study, but the same fault could not be relocated. The ØG05a fault is NW-SE trending and dips steeply towards the NE. The host-rock surrounding the fault core is a granitic gneiss, with a gneissose foliation dipping shallowly towards the NNW. The fault core is around 8-10 cm thick and was exposed over a height of 2.4 m.

On the surface of the southwestern block, a step slickenside was identified (Fig. 29B). The striations plunged shallowly to the SE and had a pitch closer to the horizontal. The risers of the steps pointed towards the NW. The positive smoothness towards the NW indicates that the southwestern slickenside block has moved towards the SE (Fig. 29B). This indicates that the ØG05a fault has had a component of sinistral strike-slip displacement. A horsetail fault termination structure was identified near the top of the fault core on the north-eastern block (Fig. 28). The horsetail structure had a top to the NE sense of shear, and this suggests, in addition to the slickenside steps, that there has been an additional component of normal dip-slip movement. The ØG05a fault is a sinistral-normal oblique dip-slip fault. Cross-cutting sub-vertical faults were also present in the surrounding host rock, producing a blocky or jointed damage zone. At the surface of the sub-vertical NE-SW striking faults, chlorite and epidote mineralization were observed (Fig. 29C). This was also found on the rock surface of the southwestern block of the ØG05a fault.

The fault core of the ØG05a fault consisted of a varyingly thick zone of fault breccia and a zone of grey clay-rich material (Fig. 29A). There were smaller fragments of the fault breccia within the clay-rich lens, and the degree of weathering of the fault was uncertain. The sample location was towards the bottom of the fault (Fig. 29A), where the lens richer in clay was targeted. The varying thickness of the gouge lens and the fact that it was intermingled with fault breccia in certain places means that it was difficult to avoid sampling larger fragments (> 2 mm) of fault breccia.

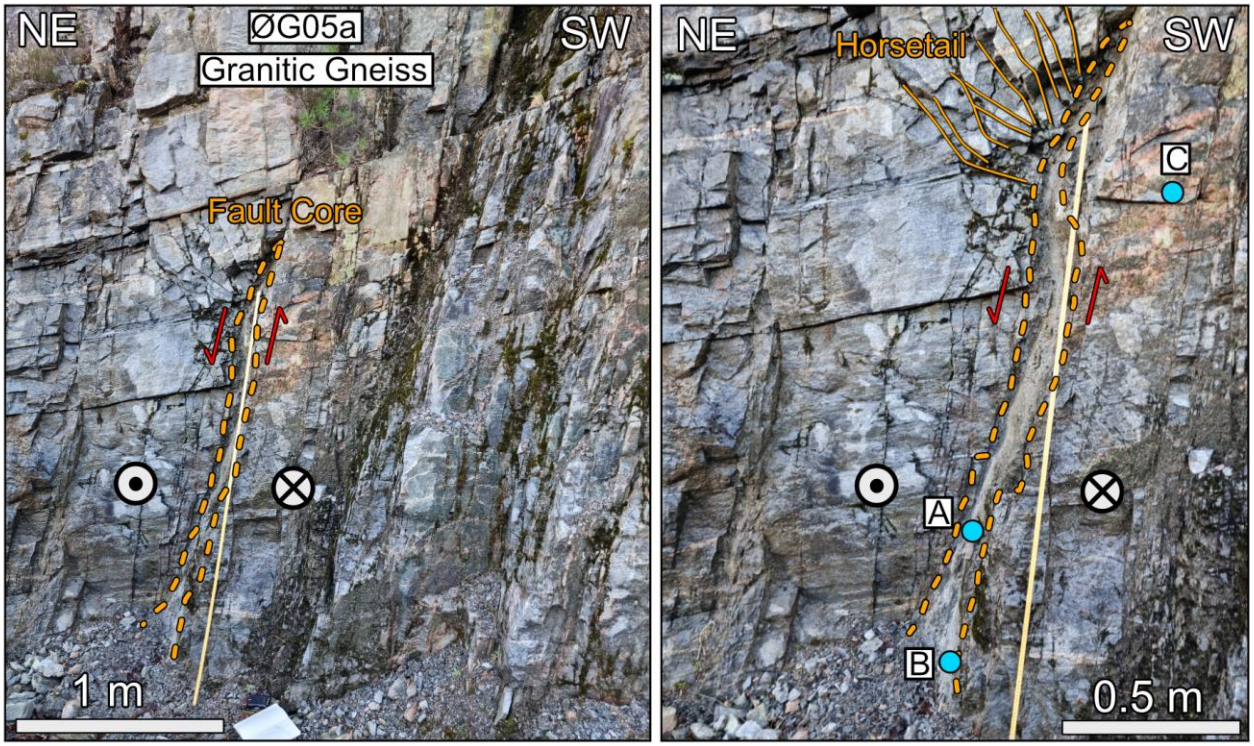

Fig. 28. *Field photographs of the ØG05a fault, located at parking area for the Olsvika boat harbor, at Vindesnes, Sotra. The fault core (dashed orange line) is 10 cm at its widest, and the exposed fault core is 2.4 m tall. The host-rock surrounding the fault is a granitic gneiss, with a gneissose banding dipping shallowly towards the NNW. The fault core consisted of an anastomosing brecciated fault rock zone; 5 cm thick at its maximum. A grey clay-rich lens of fault gouge was situated between the brecciated fault rock and the southwestern block, also 5 cm thick at its maximum. Point A marks the sample location, and other points of interest is marked with blue. Horsetail termination was identified in the NE block, indicating a component of normal dip-slip displacement.*

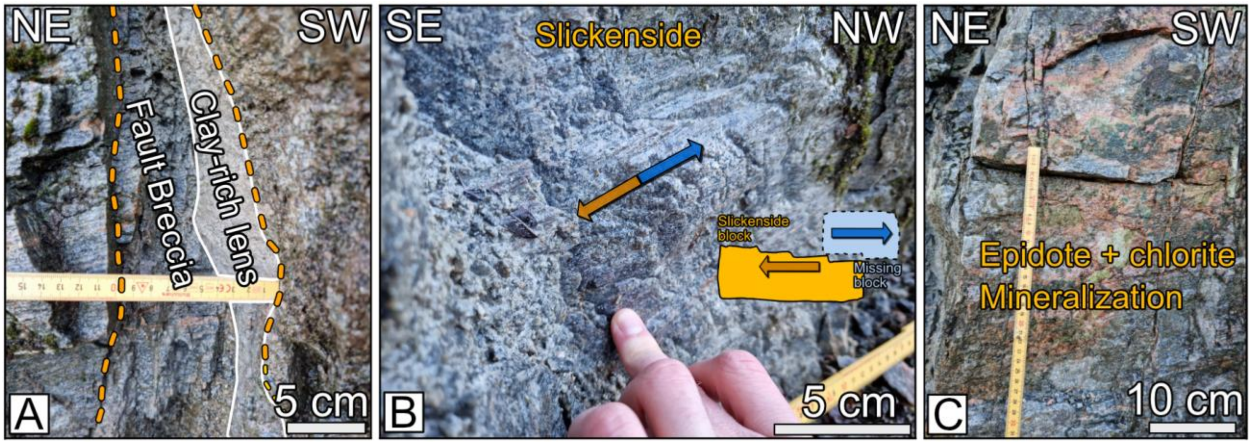

Fig. 29. A) *5 cm thick zone of fault breccia of varying thickness was observed within the fault core. A clay-rich gouge lens rans parallel to it, also 5 cm thick at its maximum. The clay-rich gouge lens was sampled.* ***B)*** *Step slickenside with striations plunging shallowly towards the SE was observed. The risers of the steps points towards the NW, indicating a component of sinistral strike-slip displacement.* ***C)*** *A crosscutting set of sub-vertical fractures, perpendicular to the fault, was observed with epidote and chlorite mineralization*

5.1.6 Døsjeneset, Sotra (ØG06a)

The ØG06a fault is located at a small quarry at Døsjeneset, Sotra (Fig. 30). This fault was studied by Ksienzyk et al. (2016) and it was active during Late Triassic to Early Jurassic (ca. 215 – 180 Ma). It is NNE-SSW trending and dips steeply towards the SSE. The host-rock of the hanging wall block and the footwall block is a granitic gneiss with migmatite banding. The fault core has a maximum width of 2.90 m towards the base and is narrower at the top. The exposed fault core is 9 m high. The footwall block (west, Fig. 30) is intensely damaged.

A step slickenside was identified in the western footwall block (Fig. 31B). The striations plunged steeply towards the SE, and the pitch was close to vertical and aligned with the fault plane itself. The risers of the steps were not very protrusive, but they appeared to be facing upwards towards the NW. This positive smoothness towards the top suggests that the western block has moved up relative to the eastern block (Fig. 30). This indicates that the ØG06a fault has had a component of normal dip-slip displacement. We observed a very complex deformation history in the footwall block, which involved both brittle and ductile deformation processes. There was folding of the banded migmatite (Fig. 31C), and numerous cross-cutting brittle faults. Within the fault core, we identified bands of migmatite that had been dragged during the faulting. The degree of drag increased towards the slip surface (Fig. 30, point A), where the felsic bands were oriented approximately parallel to the slip surface.

Towards the top of the fault core, a lens of dark-green clay gouge was embedded within two lenses of grey-green clay gouge (Fig. 30). Towards the base of the fault, we observed several slip surfaces, which mainly consisted of grey-green clay-rich gouge and some minor amounts of fault breccia. The host rock was somewhat intact within parts of the fault core, and there was apparent ductile deformation or drag of the visible granitic migmatite banding. The sample was collected in a clay-rich lens near what appeared to be the principal slip surface of the fault (Fig. 31A). The sense of shear surrounding the principal slip surface is top-down towards the east. There was a stream of water running through this fault, so it is uncertain how much clay material was derived from recent weathering.

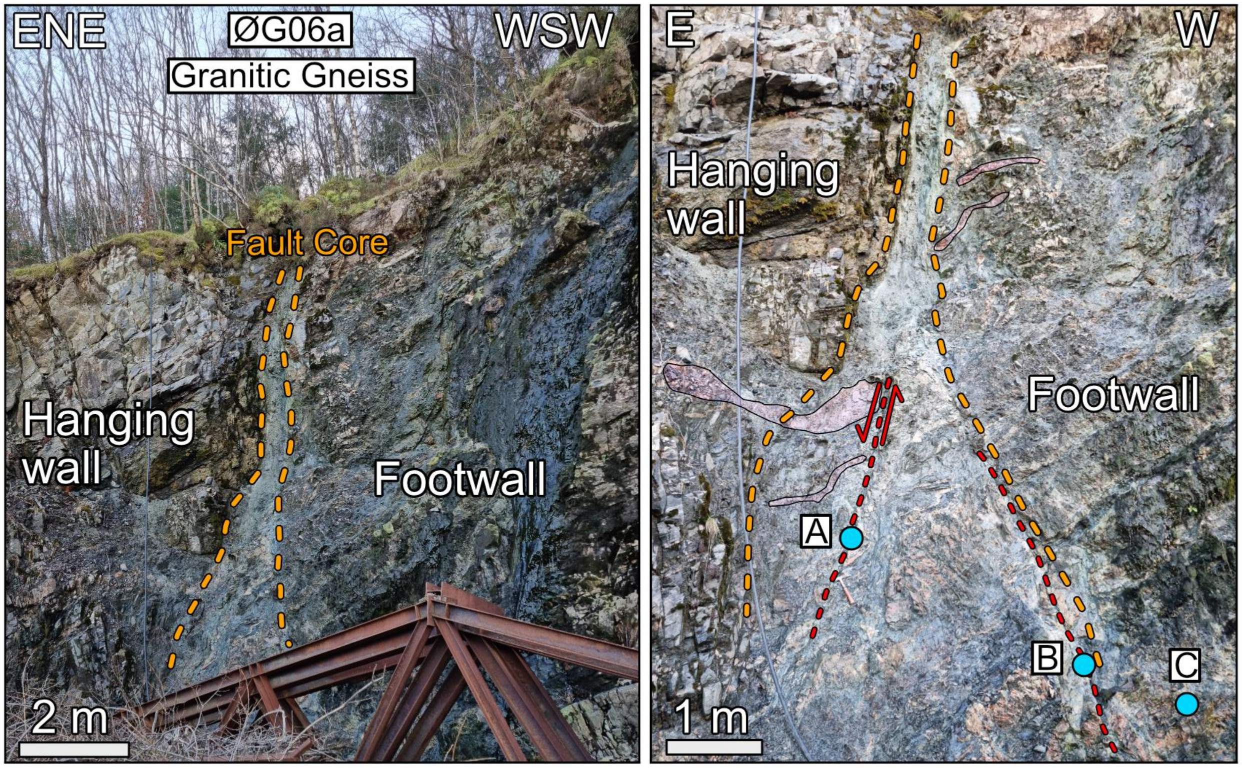

Fig. 30. *Field photographs of the ØG06a fault, located at a quarry near the marina, Døsjeneset, Sotra. The fault core (dashed orange line) is 2.60 m wide at its maximum, and the exposed fault core is about 9 meters high. The host-rock rock across both sides of the fault is a granitic gneiss with migmatite banding. The footwall block was intensely damaged. Within the fault core, several slip surfaces can be identified (dashed red lines). Towards the top of the fault core, a grey-to-green clay gouge lens surrounds a darker green clay gouge lens. Similar lenses of clay-rich gouge were found near the slip surfaces towards the bottom of the fault. The sample location is marked with A, and points of interest is marked in blue.*

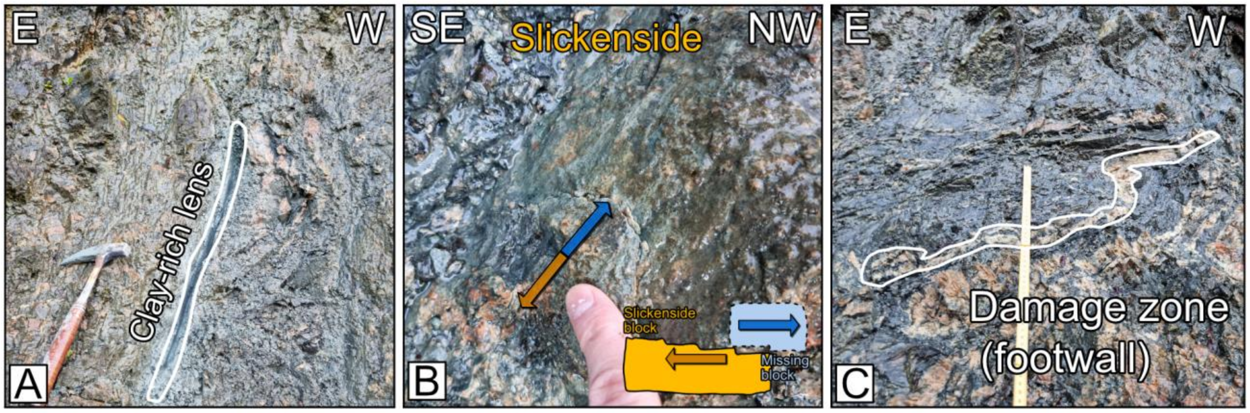

Fig. 31. A) *A clay-rich gouge lens that ran along one of the slip surfaces within the fault core. We also identified remnants of the granitic migmatite banding.* ***B)*** *Slickenside steps were identified on the footwall block. The risers of the steps points upwards towards the NW. This suggests a normal dip-slip displacement of the fault.* ***C)*** *The heavily damaged footwall block is characterized by deformed migmatite banding.*

5.1.7 Døsjeneset Sotra (ØG06b)

The ØG06b fault is located just 50 m NW of the ØG06a, at the same quarry, near the marina at Døsjeneset, Sotra (Fig. 32). This N-S striking fault dips steeply towards the E. The host rock is granitic- to granodioritic-gneiss with distinct red K-feldspar and migmatite banding. The host rock is also rich in amphibolite, resulting in a darker-green rock surface of the western block (Fig. 32). The fault core is 2 m wide at its maximum, and the exposed fault core is approximately 12 m high.

On the western block, a polished step slickenside with calcite and epidote mineralization was observed (Fig. 33C). The slickenside striations had a close to the horizontal pitch in relation to the striated fault plane surface (western block, Fig. 32). The risers of the steps were not very protrusive, but they appeared to be facing towards the N. This positive smoothness towards the N indicates that there has been a component of sinistral strike-slip displacement. The easternmost block appeared to be more intensely damaged, and both the host-rock blocks were crosscut by steeply dipping N-S and E-W striking fractures.

The fault core of the ØG06b fault mainly consisted of fault breccia and cataclasite. Towards the top section of the exposed core, there appeared to be more significant remnants of the western block still intact. In the middle and lower sections of the fault, the degree of fault brecciation appeared to be higher. Some intact migmatite banding was observed within the fault core in an amphibolitic matrix, divided by several slip surfaces (Fig. 32). Towards the lower section of the fault core, there was a large body of cacaclastic rocks (Fig. 33B). These cataclasites were characterized by angular red K-feldspar fragments in a matrix of dark green amphibolite. The cataclasites were only identified within the fault core closer to the westernmost block. This body of cataclastic rock was situated within the fault core, and where it connects to the western host-rock block, we observed a slip surface. The sample was retrieved along this slip surface, where a sandy and dark-green fault rock lens was observed (Fig. 33A).

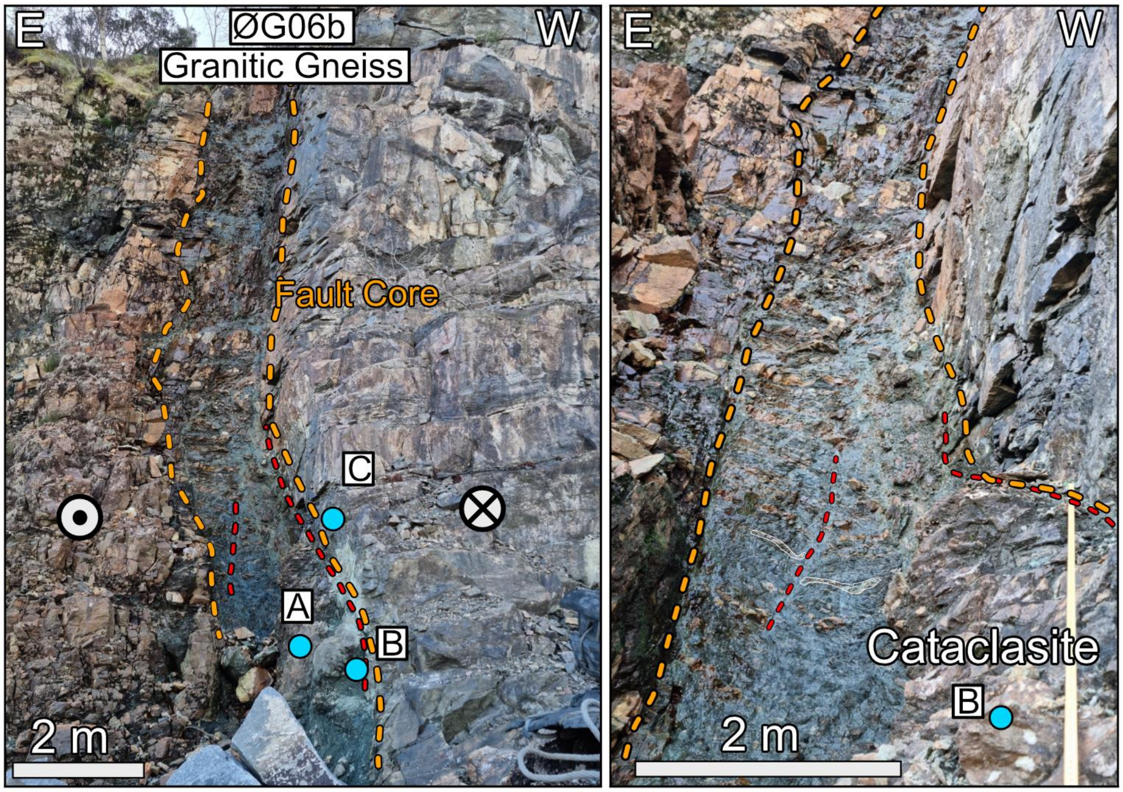

Fig. 32. *Field photographs of the ØG06b fault, located 50 m NW of ØG06a, at the quarry, Døsjeneset, Sotra. The fault core (dashed orange line) is 2 m wide at its maximum, and the exposed fault core height is 12 m. The host-rock is a granitic-to granodioritic -gneiss with red K-feldspar. The fault core predominantly consisted of cataclasite, with angular fragments of red-k feldspar in a dark green amphibolitic matrix. Fault breccia was also identified within the fault core, and a slip surface (dashed red lines) containing a finer dark-green sandy material is marked with A. Points of interest is marked with blue dots.*

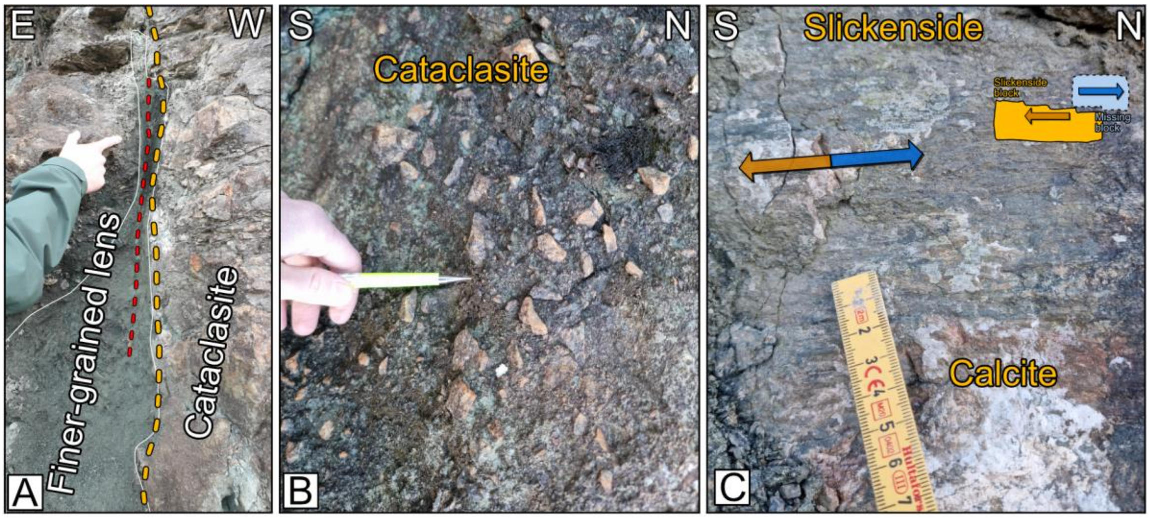

Fig. 33. A) *Lens of dark green sandy material. It runs along a slip surface of the fault. On both sides of the slip surface were cataclasites (**B**). **C)** Step slickenside with calcite and epidote mineralization was identified. The risers were polished and not very protrusive, but they appeared to point towards the N. This indicates that the striated block has moved to the S, and that the ØG06b fault has had a component of sinistral strike-slip displacement.*

5.1.8 Øygarden Complex Fault Classification

The sampled faults from the Øygarden complex were mostly normal- or reverse- dip-slip faults, except for ØG05a and ØG06b, which also had sinistral strike-slip components. The essential information gathered from each fault is summarized in Table 2 and Fig. 34.

The NE-SW striking normal dip-slip faults (i.e., ØG01 and ØG06a) were classified as Set I faults based on the Øygarden Complex fault classifications (Larsen et al., 2003). The ØG05a fault was also classified as Set I based on the presence of fault plane chlorite-and epidote-mineralization, although it did not follow the predominant E-W or extensional trend (Fig. 34). The N-S trending dip-slip to strike-slip faults (i.e., ØG02, ØG03, and ØG06b) were classified as Set II faults (Table 2).

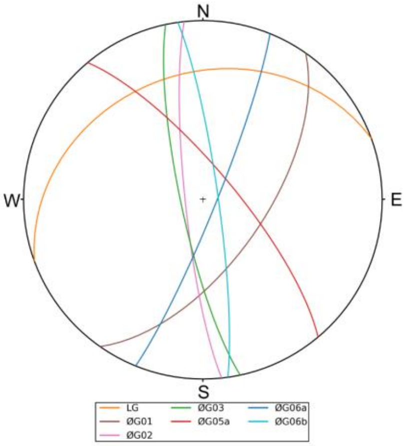

Fig. 34. *Stereonet with orientations of the sampled faults.*

Table 2. *Summary of the key information from each sampled fault. The faults have been classified based on trend, striations, fault plane mineralization, and fault rock material. Fault classifications are based (Larsen et al., 2003). Orientations of the faults are given in azimuthal strike/dip notation, using the right-hand rule. The dip direction is in brackets.*

Sample	Strike/Dip	Kinematics	Core width (m)	Mineralization	Fault rocks	Classification
LG	250/30 (NNW)	Normal dip-slip fault	1	-	Green cataclasite, green gouge, red clay gouge and shale smear.	Large-scale detachment fault
ØG01	035/62 (ESE)	Normal dip-slip fault	0.5	Calcite	Fault breccia, calcite fragments and clay-rich fault gouge.	Set I
ØG02	174/82 (W)	Reverse dip-slip (Tension fracture)	0.6	Calcite	Large veins of euhedral brecciated calcite, and fault breccia.	Set II
ØG03	168/80 (W)	Reverse dip-slip	2.9	Calcite	Fault breccia, grey and red iron-stained fault gouges.	Set II
ØG05a	320/76 (NE)	Sinistral-normal oblique dip-slip	0.01	Chlorite, Epidote	Fault breccia and grey fault gouge.	Set I
ØG06a	022/84 (ESE)	Normal dip-slip	2.9	-	Fault breccia, grey to dark green fault gouge, grey to light green fault gouge.	Set I
ØG06b	352/83 (E)	Sinistral strike-slip	2	Calcite, Epidote	Fault breccia, cataclasite and sandy dark-green material.	Set II

5.2 Fault rock grain size data

Grain size distributions

The sampled fault rocks from the Øygarden Complex were sand dominated ($\bar{x} = 43\ \%$) followed by gravel ($\bar{x} = 29.1\ \%$), silt ($\bar{x} = 21.9\ \%$), and clay ($\bar{x} = 6\ \%$), see Table 3. After removal of the clasts above 4 mm the resulting grain size distributions (Øygarden Complex) were still dominated by sand ($\bar{x} = 53.2\ \%$), followed by silt ($\bar{x} = 27.1\ \%$), gravel ($\bar{x} = 12.5$), and clay ($\bar{x} = 7.2\ \%$), see Table 4. The LG fault rock remained mostly unaltered by removing particles above 4 mm (Fig. 35) and was dominated by sand (62.2 %) followed by silt (28.8 %), Table 4.

Based on the relative horizontal positions of the grain size distribution curves (Fig. 35), it is evident that ØG05a was the coarsest fault rock, i.e., furthest to the right (Fig. 35). The ØG01 fault rock had its distribution furthest to the left and was the finest fault rock (Fig. 35). This is also clear when looking at the grain size fractions of the ØG01 and ØG05a fault rocks (Table 4). The ØG01 fault rock was rich in clay (16.7 %) and silt (30.9 %), which corresponds to a combined fines content of 47.6 % (Table 4). In comparison, the ØG05a fault rock had high gravel (17 %) and sand (54.4 %) content, which corresponds to a total fines content of 28.6 % (Table 4).

The LG, ØG05a, ØG06a, and ØG06b fault rocks were classified as well graded, as they had calculated coefficients of uniformity (C_u) above 5 and coefficients of curvature (C_c) between 1 and 3 (Table 4, see chapter 3.2). The ØG01 fault rock could not be classified as it was too rich in clay (16.7 %, Table 4), which means the D_{10} particle size (i.e., the particle size where 10 % of the material is finer by weight) could not be determined. The remaining fault rocks, ØG02 and ØG03, had coefficients of curvature below 1 and were classified as poorly graded (Table 4). The ØG02 and ØG03 fault rocks did also not meet the criterion for being uniformly graded (C_u and C_c = 1) and were subsequently classified as gap graded.

Fault rock classification

The D_{70} particle size, i.e., the particle size where 70 % of the material is finer by weight (see chapter 3.2), changed significantly due to sieving. The initial D_{70} particle sizes of the Øygarden fault rocks ranged from 1.04 to 3.50 mm (Table 3). The fault rocks classify as fault gouges if D_{70} < 2mm, and only the LG, ØG01, and ØG06a fault rocks met this criterion (Table 3). The remaining samples were classified as fault breccias ($D_{70} > 2\ mm$). After removal of the particles above 4 mm, all the samples were classified as fault gouges, as they had D_{70} values ranging from 0.49 to 1.38 mm (Table 4), all below 2 mm.

The ØG06b and the ØG05a fault rocks had concave-shaped grain size distributions (Fig. 35), which means they are grain-supported materials (Table 4, see chapter 3.2). The ØG01 had a convex-shaped distribution corresponding to a matrix-supported material. The LG had a distinct sigmoidal distribution, while the, ØG02, ØG03, ØG06a fault rocks had linear distributions (Fig. 35). These latter faults (i.e., LG, ØG02, ØG03, and ØG06a) were transitional (i.e., a mixture of the end members).

Table 3. *An overview of the key information before sieving to 4 mm. The soil description is based on the fractions of gravel, sand, silt, and clay. Sandy (> 5 % sand), SAND (> 60 % sand). The fault rock classification (Woodcock and Mort, 2008) is based on the* D_{70} *particle size. The sample means* ($\bar{x}$) *for the grain size parameters of the Øygarden Complex fault rocks is in the bottom row.*

	Sampled fault rock															
	Grain Size Distribution (mm)				Fractions (%)					Description			Soil grading			Weight
Sample	D10	D30	D60	D70	Gravel	Sand	Silt	Clay	Fines	Soil description	Fault rock (D70)	Grain- or matrix supported	CU	CC	Result	Dry (g)
LG	0.005	0.04	0.24	0.39	3.2	61.6	28.5	6.7	35.2	SAND, silty, clayey	Fault Gouge	transitional	49	1.6	Well graded	1832.7
ØG01	-	0.02	0.48	1.04	20.7	38.4	26.6	14.3	40.9	Sandy, silty, gravelly, clayey	Fault Gouge	matrix-supported	-	-	-	657.2
ØG02	0.004	0.13	1.88	3.50	39.1	35.2	21.5	4.2	25.7	Gravelly, sandy, silty	Fault Breccia	transitional	469	2.2	Well graded	751.4
ØG03	0.005	0.08	1.63	3.50	37.4	34.4	25.5	2.7	28.2	Gravelly, sandy, silty	Fault Breccia	transitional	327	0.8	Gap graded	1144.6
ØG05a	0.004	0.19	1.72	3.17	37.5	41	16.1	5.4	21.5	Sandy, gravelly, silty, clayey	Fault Breccia	Grain-supported	431	5.3	Gap graded	1298.6
ØG06a	0.004	0.06	0.92	1.94	29.4	39.6	24.5	6.5	31	Sandy, gravelly, silty, clayey	Fault Gouge	transitional	230	0.9	Gap graded	1347.5
ØG06b	0.036	0.43	1.73	3.05	36.5	51	10.5	2	12.5	Sandy, gravelly	Fault Breccia	Grain-supported	48	3.0	Well graded	2272.5
ØC ($\bar{x}$)	0.011	0.15	1.39	2.70	33.43	39.93	20.78	5.85	26.63							

Table 4. *An overview of the key information after sieving to 4 mm. The soil description is based on the fractions of gravel, sand, silt, and clay. Sandy (> 5 % sand), SAND (> 60 % sand). The fault rock classification (Woodcock and Mort, 2008) is based on the* D_{70} *particle size. The sample means* ($\bar{x}$) *for the grain size parameters of the Øygarden Complex fault rocks is in the bottom row.*

	Tested material (After 4 mm sieving)																
	Grain Size Distribution (mm)				Fractions (%)					Description			Soil grading			Weight	
Sample	D10	D30	D60	D70	Gravel	Sand	Silt	Clay	Fines	Soil description	Fault rock (D70)	Grain- or matrix supported	CU	CC	Result	Dry (g)	Loss of particles (g)
LG	0.005	0.04	0.24	0.38	2.3	62.2	28.8	6.8	35.5	SAND, silty, clayey	Fault Gouge	transitional	48	1.5	Well graded	1652.9	179.8
ØG01	-	0.01	0.23	0.49	7.8	44.7	30.9	16.7	47.6	Sandy, silty, clayey, gravelly	Fault Gouge	matrix-supported	-	-	-	495	162.2
ØG02	0.004	0.03	0.55	1.01	16.6	48.2	29.5	5.7	35.2	Sandy, silty, gravelly, clayey	Fault Gouge	transitional	157	0.4	Gap graded	577.1	174.3
ØG03	0.004	0.03	0.34	0.77	13.7	47.5	35.1	3.8	38.9	Sandy, siltey, gravelly	Fault Gouge	transitional	85	0.9	Gap graded	928.9	215.7
ØG05a	0.003	0.08	0.72	1.15	17.0	54.4	21.4	7.2	28.6	Sandy, siltey, gravelly, clayey	Fault Gouge	Grain-supported	225	2.5	Well graded	972.5	326.1
ØG06a	0.003	0.04	0.41	0.79	13.8	48.4	30.0	7.9	37.9	Sandy, silty, gravelly, clayey	Fault Gouge	transitional	137	1.3	Well graded	1049	298.5
ØG06b	0.021	0.25	0.96	1.38	16.3	67.3	13.9	2.6	16.5	SAND, gravelly, silty	Fault Gouge	Grain-supported	46	3.0	Well graded	1990.7	281.8
ØC ($\bar{x}$)	0.007	0.07	0.54	0.93	14.2	51.7	26.8	7.3	34.1								

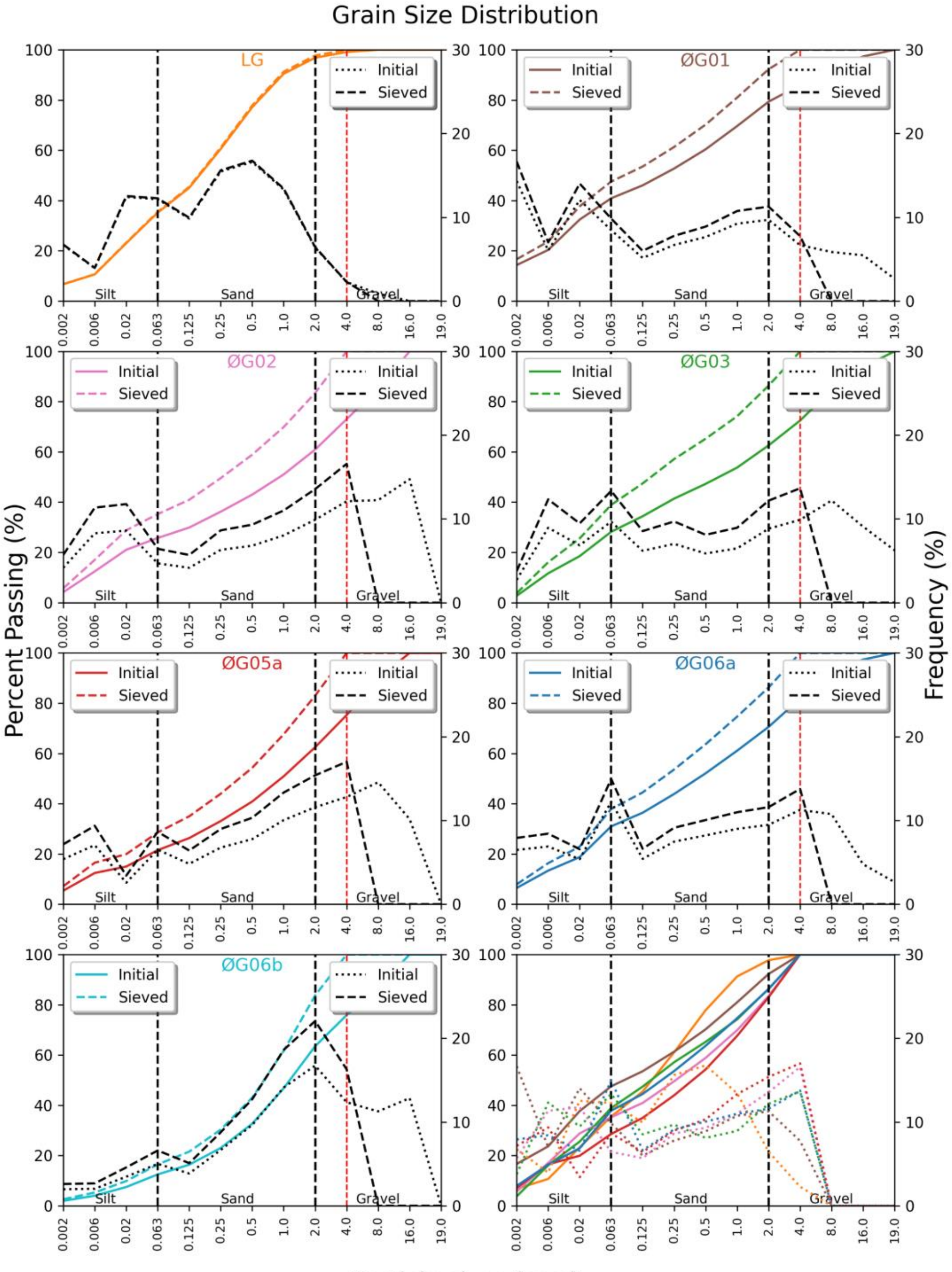

Fig. 35. *Grain size distributions (colored lines) and grain size frequencies (black lines) before and after sieving for direct shear box testing. The solid-colored line and dotted black line represent the in-situ fault rock material. The dashed line represents the particle distribution and frequency of the tested fault rock (sieved 4 mm). The red dashed vertical lines represent the maximum particle size at 4 mm selected for DST.*

5.3 Fault Rock Mineralogy

Fault rock mineralogy from XRD

The identified and quantified minerals phases of the studied fault rocks are presented in Table 5. The fault rocks from the Øygarden Complex were dominated by quartz ($\bar{x} = 33.2$ %), followed by muscovite ($\bar{x} = 28.6$ %), feldspars (i.e., plagioclase and K-Feldspar, $\bar{x} = 25.1$ %), chlorite ($\bar{x} = 11.8$ %), and kaolinite ($\bar{x} = 7.9$ %), Table 5.

The feldspar content of the LG fault rock, at 51.8 %, was significantly higher than that of Øygarden Complex fault rocks (Table 5). The LG fault rock also contained 25 % epidote, and a corresponding low quartz content of 3.7 %, derived from the mafic Jotun Nappe hanging wall block.

Within the Øygarden Complex, the ØG06a fault rock had the highest chlorite content of 26.7%, while the ØG01 fault rock had the highest kaolinite content of 15.3 %. Additionally, the ØG01, ØG03, and the ØG06a fault rocks had the lowest feldspar contents (i.e., plagioclase and K-feldspar) of 18.4, 17.2, and 9.2 %, respectively. Their combined feldspar content was significantly lower compared to the other fault rocks from the Øygarden Complex and the Lærdal-Gjende fault (Table 5).

The remaining clay minerals in Table 5, i.e., illite and smectite, were not quantified in the Rietveld Refinement process. Smectite was overestimated when selected as a constituent phase, with quantities upwards of 40 % in some samples (i.e., compared to clay and silt fractions), and no reference mineral for illite was available in the Profex software (Doebelin and Kleeberg, 2015). The Rietveld Refinement results are presented in Appendix 4, and the clay powdered XRD graphs can be seen in Appendix 3.

Table 5. *Overview of identified minerals from both bulk XRD and powdered clay analysis. Bulk XRD results have been used for a semi-quantitative analysis using Rietveld refinement in Profex. + minerals identified but not quantified, – not identified, ? uncertain. Qz – Quartz, Pl – Plagioclase, Kfs – K-feldspar, Ep – Epidote, Ms – Muscovite, Cal – Calcite, Chl – Chlorite, Ilt – Illite, Sme – Smectite, Kln – Kaolinite (abbr. from Whitney and Evans, 2010). GoF is goodness of fit of the refinement curves. Fsp, i.e., feldspar, is the summed contents of plagioclase and K-feldspar per fault rock sample. The sample mean values ($\bar{x}$) of the identified minerals for the fault rocks from the Øygarden Complex is in the bottom row.*

	Minerals							Clay Minerals				
Sample	**Qz**	**Pl**	**Kfs**	**Fsp**	**Ep**	**Ms**	**Cal**	**Chl**	**Ilt**	**Sme**	**Kln**	**GoF**
LG	3.74	31.08	20.74	51.82	25.10	9.01	0.44	9.88	+	?	-	1.52
ØG01	42.00	9.49	8.89	18.38	-	11.80	-	12.50	+	+	15.3	2.58
ØG02	43.31	17.31	14.94	32.25	-	21.62	2.82	-	?	+	-	3.37
ØG03	41.42	9.60	7.62	17.22	-	40.00	1.38	-	?	+	-	2.64
ØG05a	25.75	20.47	12.73	33.20	-	29.91	3.57	1.18	?	+	6.39	2.50
ØG06a	17.81	9.18	-	9.18	-	40.60	2.39	26.65	+	-	3.37	1.81
ØG06b	29.19	16.52	12.65	29.17	-	27.80	-	7.2	+	-	6.64	2.41
ØC ($\bar{x}$)	33.25	13.76	11.37	25.13	-	28.62	2.54	11.88	-	-	7.93	

Fault rock descriptions from thin sections

The studied fault rock thin sections (i.e., the Øygarden Complex and Lærdal-Gjende), represent the fault rock material after removal of particles above 4 mm. The resulting thin sections are shown in Fig. 36.

The Lærdal-Gjende fault gouge consisted of fractured sub-angular to angular particles in a fine-grained phyllosilicate matrix (Fig. 36A). Calcite inclusions were observed in one of the larger quartz grains (Fig. 36A). The ØG01 fault gouge consisted of large sub-rounded grains in a finer phyllosilicate matrix (Fig. 36B). Aggregates of quartz and feldspar grains with alteration and infill were abundant in the larger grains (Fig. 36B). These also had patchy extinction with bulging grain boundaries. The ØG02 fault gouge consisted of elongated sub-angular grains (Fig. 36C). Some of the larger grains had distinct cleavage in two directions, with ca. 5° extinction relative to the cleavage direction of the grain-elongation. The large grains of feldspar and quartz had numerous inclusions and alteration spots, and the grains had patchy extinction with bulging grain boundaries (Fig. 36C). The matrix was obscured by a dark colour, making observations of the matrix difficult. The ØG03 fault gouge consisted of varyingly sized sub-angular clasts in a fine phyllosilicate matrix (Fig. 36D). The larger grains appeared more rounded than the smaller particles and displayed a patchy extinction with bulging grain boundaries (Fig. 36D). The red staining was visible in the thin section and was interpreted as red iron staining. Elongated grains of calcite were present in minor amounts. The ØG05a fault gouge consisted of sub-angular grains in a fine phyllosilicate matrix (Fig. 36E). The larger grains of feldspar had inclusions, alterations, and patchy extinction with bulging grain boundaries (Fig. 36E). The ØG06a fault gouge consisted of very large, angular, and fractured feldspar grains in a fine phyllosilicate- to smaller sized quartz-matrix. The fractures were infilled by calcite veins, which are in some areas replaced by the phyllosilicate matrix near the grain boundaries (Fig. 36F). Smaller clasts of angular quartz and feldspar were present within the phyllosilicate- to quartz-matrix. The ØG06b fault gouge consisted of medium-sized sub-angular to angular clasts in a fine phyllosilicate matrix (Fig. 36G). Larger cataclastic grains with smaller angular fragments of feldspar and quartz were highly altered by chlorite (Fig. 36G). Chlorite was abundant in the thin section, with minor biotite amounts.

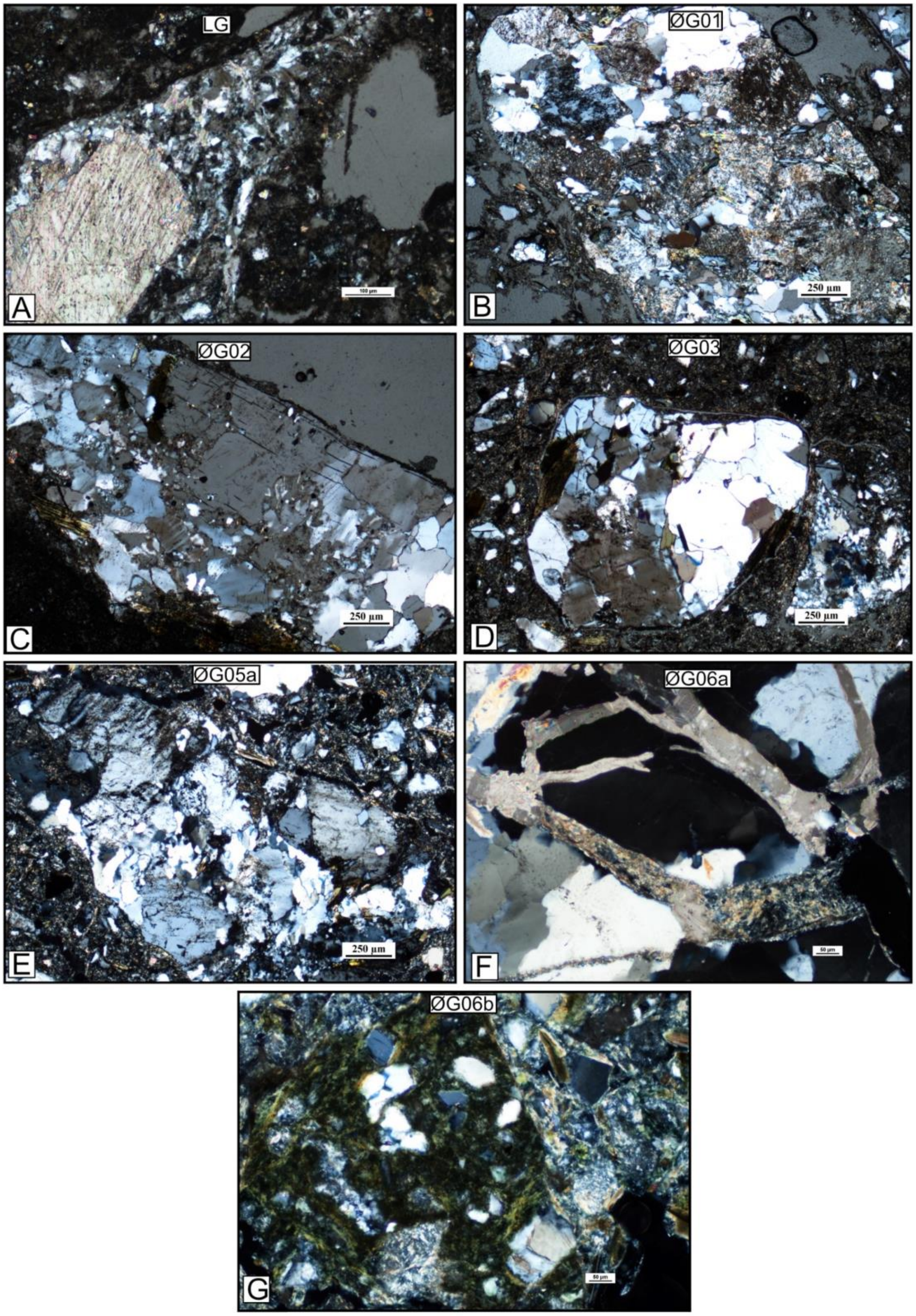

*Fig. 36. Photomicrographs of the fault rock material **A)** The LG fault rock had calcite inclusions. **B)** The ØG01 fault rock contained highly altered feldspar grains. **C)** The ØG02 fault rock contained large and elongated quartz and feldspar grains. **D)** The ØG03 fault rock consisted of larger and sub-rounded grains in a very fine matrix. **E)** The ØG05a fault rock had altered feldspar grains in a very fine matrix. **F)** The ØG06a fault rock had large feldspar grains with weathered calcite veins infilled by fine-grained materials. **G)** The ØG06b fault rock contained cataclastic feldspar grains replaced by chlorite.*

5.4 Shear strength of the fault rocks

Index properties

A total of 30 direct shear box tests were conducted. Most fault rocks samples had a decrease in water saturation based on experimentation data pre-and post-shear, presented in Appendix 1. The most significant drop in saturation was observed in the ØG01 and ØG06a fault rock samples at normal stress ($\sigma_n = 1.5\ MPa$), where water content dropped from 30 % to 13 % and from 25 % to 9 %, respectively. However, the ØG06b fault rock increased in water content from 10 % to close to 20 % at all tested normal stresses.

Compared to initial conditions, the bulk densities increased across all samples during consolidation and shearing (Appendix 1). The void space of all the samples decreased as a response. The greatest change in bulk density was observed in ØG01 and ØG06a at the higher effective normal stresses ($\sigma_n > 0.5\ MPa$).

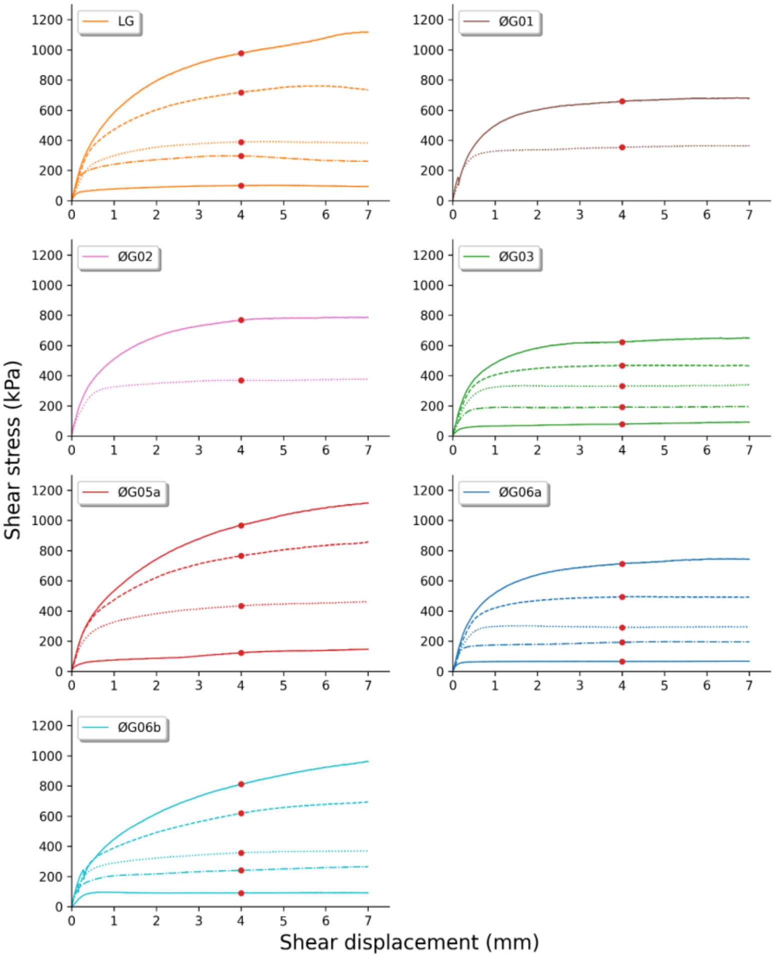

Fig. 37. *Shear graphs for all the tested fault rocks. The horizontal (shear) displacement is plotted on the x-axis, while the shear stress is on the y-axis. Obtained shear stress at 4 mm shear displacement is marked with a red circle. Each curve represents one experiment at a specified normal stress, and a minimum of three tests (different normal stresses) is recommended to compute the failure envelope.*

In the ØG06b sample, the loading pad was tilted as the shear displacement increased. The tilt occurred after 4 mm shear displacement (d), which means that the shear stress path prior to and up to 4 mm was not affected.

Shear stress graphs

The resulting shear graphs for each fault are shown in Fig. 37. The shear graphs show the obtained shear stress as the samples are displaced, and each curve represent one experiment. Most of the tested fault rocks underwent some degree of strain hardening at the higher tested normal stresses (0.5 to 1.5 MPa, Fig. 37), with over-consolidation ratios (OCR) of 3.5, 1.75, 1.17 (Appendix 1). The fault rocks tested at the lower normal stresses (0.1 to 0.5 MPa) experienced significantly less strain hardening, and more well-defined failure curves were observed (Fig. 37). The over-consolidation ratios for the lower normal stress test range were constant at 3.5. When comparing the studied fault rocks, it is evident that the LG, ØG05a, and the ØG06b fault rocks experienced more strain hardening (Fig. 37).

Volumetric response

The volumetric response (i.e., changes in vertical sample height) as the fault rock samples were sheared is presented in Fig. 38. The ØG06b fault rock had a significant volumetric response. It was compressed at the higher normal stresses (1.0 to 1.5 MPa) and dilated at the lower stresses (0.1 MPa), Fig. 38. The ØG05a fault rock had a significant increase in sample height as it was sheared at the lower normal stresses, i.e., dilation (Fig. 38). The volumetric responses of the remaining fault rocks were less pronounced (Fig. 38). However, the higher normal stresses (1.0 to 1.5 MPa) generally led to compression, while the lower normal stresses (0.1 to 0.5 MPa) led to dilation as the samples were sheared.

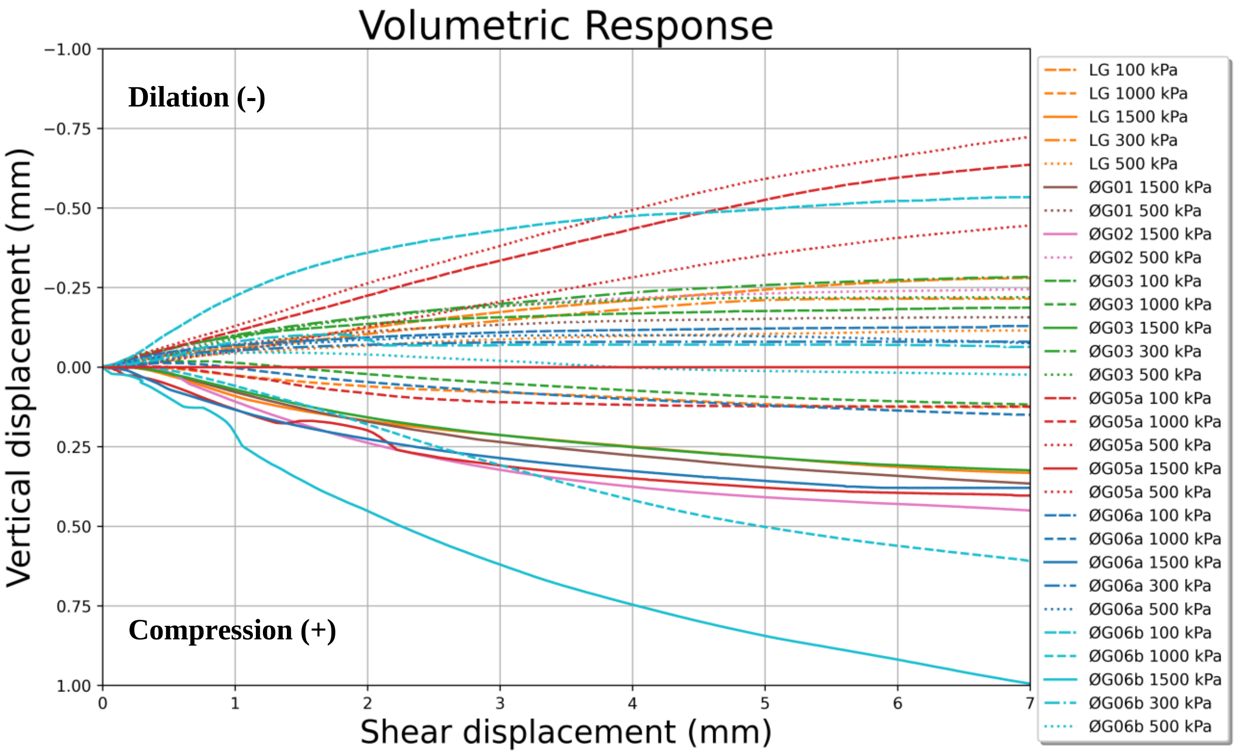

Fig. 38. *Graph showing the volumetric response of the fault rock samples as they are sheared. Any change of height (vertical displacement change) in the sample during the experiment changes the volume either by dilation (-) or compression (+).*

Failure envelopes

In the absence of distinct brittle failure (maximum σ_s, σ_n obtained), peak (-residual) strength at 4 mm shear displacement was systematically picked (Fig. 37). The resulting failure envelopes, found by linear least square regression, are presented in Table 6 and Fig. 40. Three different failure envelopes were computed for each fault rock with sufficient material, one for the lower normal stresses (0.1 to 0.5 MPa), one for the upper normal stresses (0.5 to 1.5), and one for all normal stresses (0.1 to 1.5 MPa), Fig. 39. All these failure envelopes per fault can be seen in Appendix 2.

The criterion for the upper normal stresses for the Øygarden Complex fault rocks with sufficient testing material had a mean cohesion of 160.9 kPa and a mean friction angle of 21.6° (Table 6). The criterion for the lower normal stresses had a mean cohesion of 24.1 kPa, and a mean friction angle of 33.6° (Table 6). A bi-linear or non-linear failure envelope was found by combining the upper and lower normal stress envelopes (Fig. 39, Appendix 2). These non-linear failure envelopes were characterized by a decrease in friction angles and an increase in cohesion as a function of increased normal stress (Appendix 2).

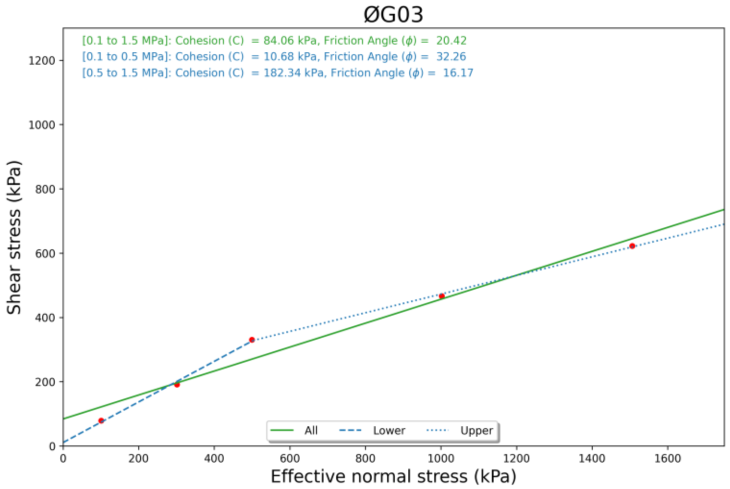

Fig. 39. *The ØG03 fault rock had sufficient materials for 5 tests. Using the 5 available peak points, three failure envelopes can be found by linear least square regression. One for the lower normal stresses (0.1 to 0.5 MPa), one for the upper (0.5 to 1.5 MPa), and one for the total (0.1 to 1.5 MPa).*

Using all available test data over the entire tested normal stress range (Fig. 40, Table 6), the fault rocks from the Øygarden Complex had an average residual friction angle (ϕ_r) of $\bar{x} = 23.5°$, and cohesion (C_r) of $\bar{x} = 113.7$ kPa. The Lærdal-Gjende fault had a significantly higher friction angle ($\phi_r = 31.4$). Within the Øygarden Complex fault rocks, the ØG01 fault rock had the lowest angle of internal friction ($\phi_r = 16.8°$), while the ØG05a fault rock had the highest angle of internal friction ($\phi_r = 31.3°$). The strain hardening effect, mentioned above, is also apparent when comparing the peak strengths at 4 mm (Fig. 40). The samples that underwent the highest degree of strain hardening (i.e., LG, ØG05a, and ØG06b) had higher obtained shear stress at 4 mm shear displacement compared to the other tested fault rocks.

Coefficient of sliding friction

The coefficients of sliding friction (μ_f), i.e., the shear stress over normal stress ratio, at 4 mm shear displacement for the 1.5 MPa tests are shown in Table 6. The ØG01, ØG03 and ØG06a fault rocks were below the threshold value of $\mu_f = 0.5$ for stable sliding (Table 6, see chapter 3.3). The ØG02 fault rock was close to the threshold, while LG, ØG05a and ØG06b were above the threshold value (Table 6).

Table 6. *Summary of the failure envelopes for the sampled fault rock material. Normal stress is given in the first columns, which represents the normal stresses that were used for testing. The number of tests is in brackets. Lower, upper, and total failure envelopes are determined by selecting peak values at 4 mm displacement. The coefficient of friction (μ_f) was found by the shear stress over the normal stress at 4 mm shear displacement for the 1.5 MPa test. The sample mean ($\bar{x}$) of the residual shear strength parameters (C_r, ϕ_r) for the different failure envelopes is seen in the bottom row.*

	Residual strength (4 mm)									
	Lower normal stresses			**Upper normal stresses**			**Total failure criterion**			**Sliding Friction**
Sample	σ_n (MPa)	C_r (kPa)	ϕ_r	σ_n (MPa)	C_r (kPa)	ϕ_r	σ_n (MPa)	C_r (kPa)	ϕ_r	**Stable sliding if μ_f < 0.5**
LG	0.1, 0.3, 0.5 (3)	43.0	35.9	0.5, 1.0, 1.5 (3)	106.7	30.3	0.1, 0.3, 0.5, 1.0, 1.5 (5)	78.0	31.4	0.65
ØG01	-	-	-	0.5, 1.5 (2)	201.3	16.8	0.5, 1.5 (2)	201.3	16.8	0.43
ØG02	-	-	-	0.5, 1.5 (2)	169.8	21.6	0.5, 1.5 (2)	169.8	21.6	0.51
ØG03	0.1, 0.3, 0.5 (3)	10.7	32.3	0.5, 1.0, 1.5 (3)	182.3	16.2	0.1, 0.3, 0.5, 1.0, 1.5 (5)	84.1	20.4	0.41
ØG05a	0.1, 0.5 (2)	44.0	37.9	0.5, 1.0, 1.5 (3)	190.5	27.9	0.1, 0.5, 1.0, 1.5 (4)	103.2	31.1	0.64
ØG06a	0.1, 0.3, 0.5 (3)	12.3	29.4	0.5, 1.0, 1.5 (3)	77.4	22.7	0.1, 0.3, 0.5, 1.0, 1.5 (5)	44.8	24.1	0.47
ØG06b	0.1, 0.3, 0.5 (3)	29.4	33.6	0.5, 1.0, 1.5 (3)	144.1	24.1	0.1, 0.3, 0.5, 1.0, 1.5 (5)	79.1	26.7	0.54
ØC ($\bar{x}$)	-	24.1	33.3	-	160.9	21.6	-	113.7	23.5	0.50

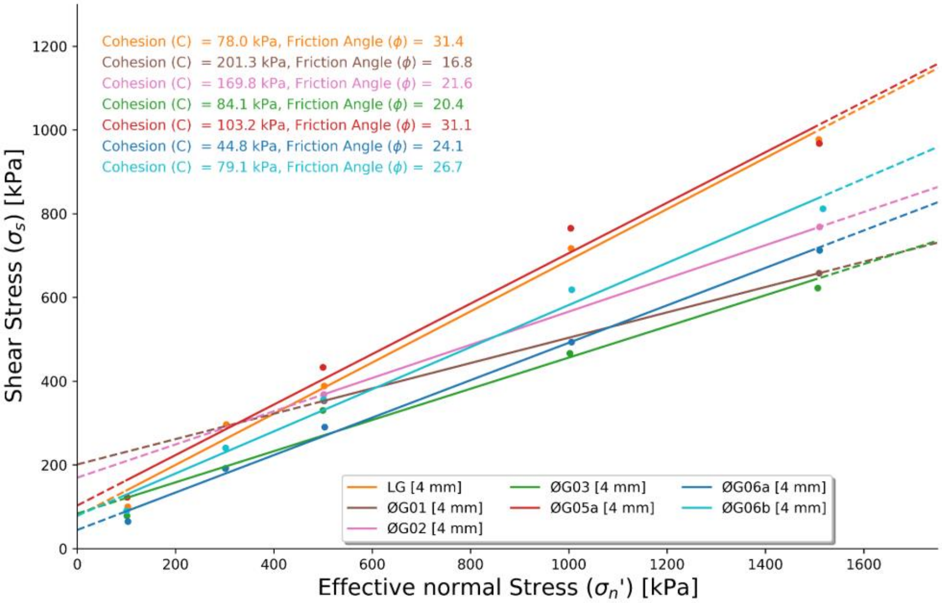

Fig. 40. *Failure envelopes using all available test data (0.1, 0.3, 0.5, 1.0 and 1.5 MPa). The number of points represents the number of tests conducted per fault rock, as material was limited. 5 tests were conducted for LG, ØG03, ØG06a, ØG06b, 4 tests for ØG05a and 2 tests for ØG01 and ØG02. The uncertainty of the failure envelope of the ØG01 (brown) and ØG02 (pink) is therefore higher based on the number of tests conducted. The failure envelopes are only valid within the tested normal stress range, which is indicated by a solid line. The dashed lines correspond to the extrapolated failure envelopes outside the tested range.*

5.5 Øygarden Complex friction angle comparisons

In this section, the friction angles (0.1 to 1.5 MPa, Table 6) from the Øygarden Complex fault rocks will be correlated to the studied parameters in terms of fault-related data (Table 2), grain size data (Table 4), and mineralogical data (Table 5). The Lærdal-Gjende fault rock was excluded in this comparison as the crystalline basement derived fault rocks from the Øygarden Complex were the main interest.

Fault data

The studied fault rocks from the Øygarden Complex did not differ much in host-rock composition. No systematic correlation between host-rock composition and the residual friction angles (ϕ_r) of the Øygarden Complex fault rocks was identified (Fig. 41a).

No apparent difference in friction angles was observed between Set I and Set II faults (Fig. 41b). Based on kinematics, slightly higher friction angles were identified for the strike-slip faults than the normal or reverse faults (Fig. 41c). A gentle negative correlation was observed in terms of fault core width, although with a very low r^2 of 0.02 (Fig. 41d).

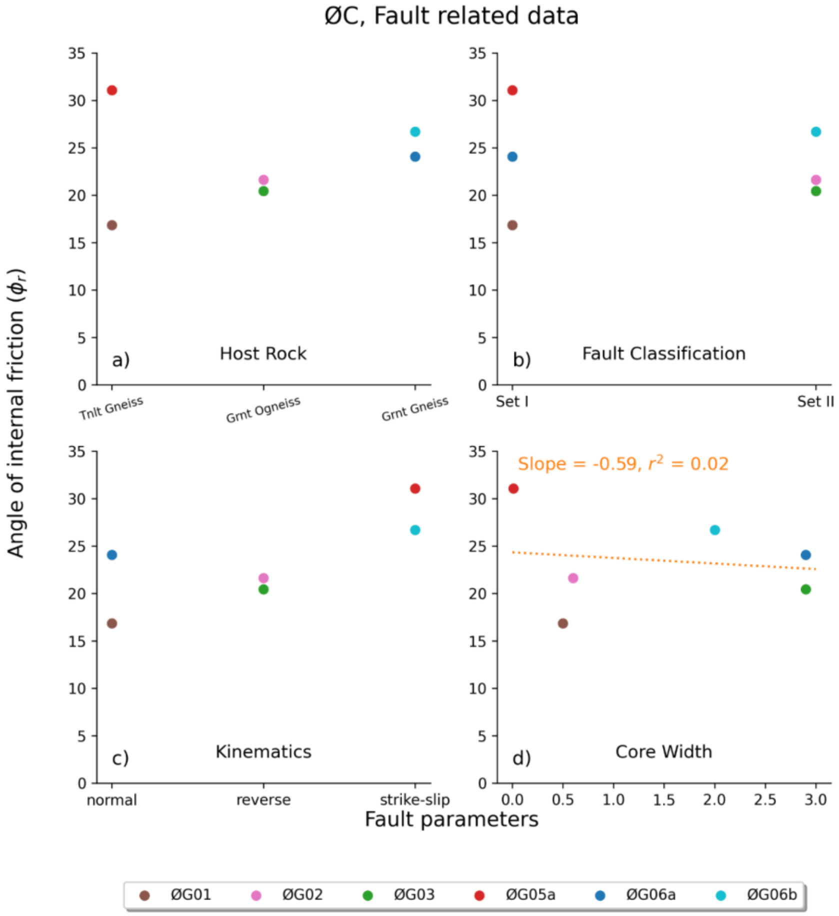

Fig. 41. *Angles of internal friction (ϕ_r) at 4 mm shear displacement compared to fault parameters based on the field work. The Lærdal-Gjende fault rock was excluded.*

Grain size data and friction angles

The fault rocks from the Øygarden Complex had moderately strong positive correlations in friction angle (ϕ_r) with increasing gravel and sand content (Fig. 42a-b). For both the silt and clay fractions, weak to moderate negative correlations was observed in friction angles with increasing silt and clay contents (Fig. 42c-d). In terms of soil grading, the well-graded fault rocks had a higher residual friction angle (ϕ_r) than the gap-graded materials (Fig. 42e). A slight correlation between the qualitative angularity descriptions (i.e., thin section analysis) and the friction angles was observed, where sub-angular to angular grains had slightly higher friction angles (Fig. 42e)

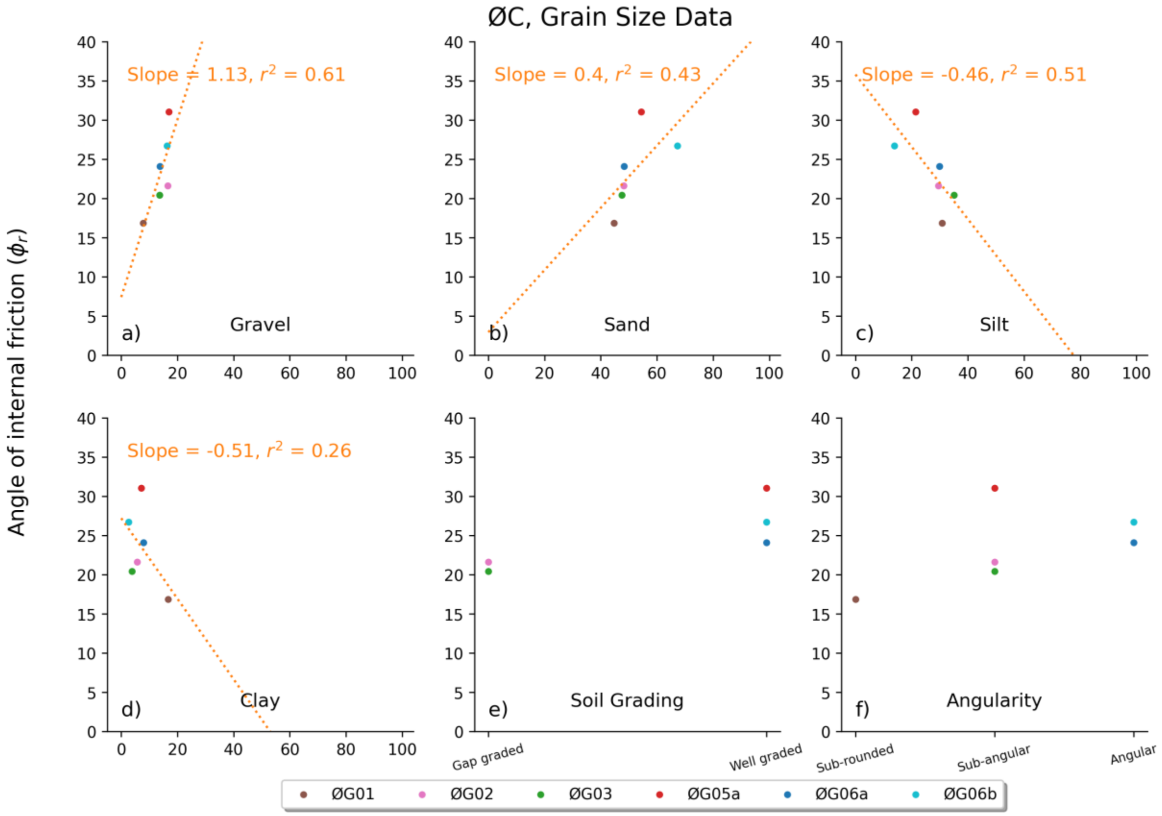

***Fig. 42**. Difference in friction angles (ϕ_r) with varying grain size fractions, soil grading and qualitative angularity descriptions. Linear least-squares regression was used to model the relationship between the friction angle and the grain size data. The Lærdal-Gjende fault rock was excluded.*

Mineralogical data and friction angles

Quartz displayed a negative trend in terms of residual friction angle (ϕ_r), with increasing quartz content (Fig. 43a). The feldspars displayed a positive correlation with increasing mineral content (Fig. 43b). The friction angle (ϕ) does not seem to be affected by a difference in muscovite content (Fig. 43c). Friction angle appears to increase steeply with increasing calcite content (Fig. 43d). The phyllosilicates (i.e., kaolinite and chlorite) display a negative trend with increasing content (Fig. 43e-f). It is common to group muscovite and phyllosilicates as one general mica group representing all phyllosilicates. When grouping the all the phyllosilicates a slight negative trend is observed (Fig. 43h).When grouping the non-phyllosilicates (i.e., quartz, plagioclase, K-feldspar, and epidote) a slight positive correlation between the mineral content and angle of internal friction is observed (Fig. 43e).

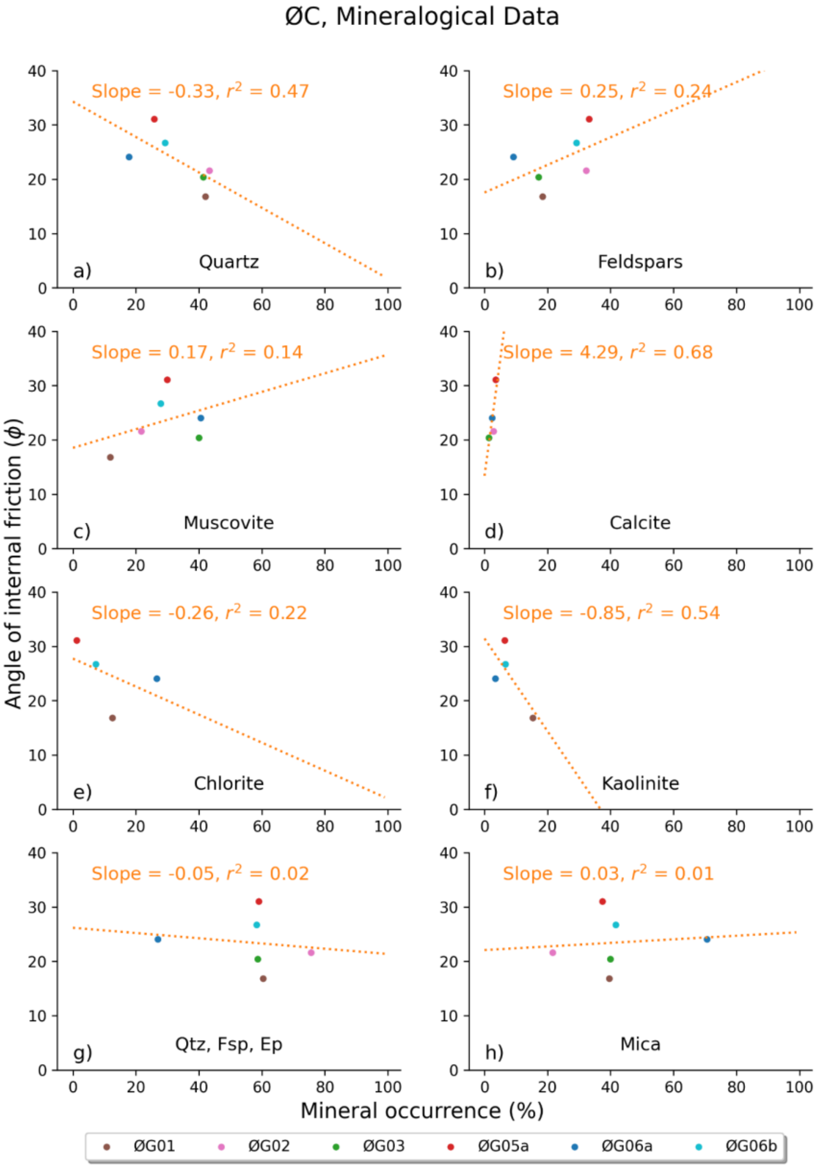

Fig. 43. *Graph showing the angles of internal friction (ϕ) compared to the mineral occurrences from the bulk XRD quantification. Only minerals with a minimum of three data points have been selected, to produce linear least square regression (orange dashed lines). The Lærdal-Gjende fault rock was excluded.*

6 Discussion

We aimed to investigate the existence of systematic friction angle trends that could be applied to fault gouges and fault rocks derived from granitic gneisses of the Øygarden Complex (ØC). The faults' structural characteristics and fault rock properties (i.e., grain size and mineralogical data) were of particular interest.

In this chapter, the question of how representative the fault rock samples are after modifications and the applied test procedures will be discussed. This is followed by a discussion of how the friction angles (ϕ_r) correlate to the measured parameters. The shear strength of the tested fault rock material will also be compared to previous studies on synthetic and natural gouges. Lastly, recommendations for fault stability modelling parameters for the Øygarden Complex granitic gneiss fault rocks will be suggested.

6.1 Methodology impact

There are several limitations and difficulties when acquiring data from surface-exposed fault rocks. The test procedures and parameters could also affect the resulting friction angles, grain size distributions, and mineralogical data. This will be highlighted and discussed in this section. The presented data was gathered using standardised methods (ASTM-D6913, 2009; ASTM-D3080, 2011), but it is still beneficial to discuss the limitations regarding the produced data. An important question to ask is, how representative are the sampled fault rocks?

6.1.1 Fault rock sampling and sample handling

In this study, we targeted the assumed finest and mechanically weakest material, i.e., fault gouges. The fault rock lenses in the studied area (i.e., the Øygarden Complex) were often discontinuous, anastomosing, and intermingled between host-rock fragments and fault breccia, which may have led to the sampling of mixed fault rocks (see chapter 5.1). Sampling of larger fragments of host rock or fault breccia could lead to higher friction angles of the fault rocks, as it is well documented that coarse and oversized particles generally increase the friction angles (e.g., Li, 2013; Islam et al., 2019; Fakhimi and Hosseinpour, 2008; Alias et al., 2014). However, this effect of accidental sampling was mitigated in this work due to removing particles above 4 mm (DST max particle size; ASTM-D3080, 2011).

The average gravel content of the original Øygarden Complex fault rocks was 33.4 % (Table 3), while after modifications (i.e., removal of particles > 4 mm), it was 14.2 % (Table 4). This is expected to have lowered the resulting friction angles (Li, 2013; Islam et al., 2019; Fakhimi and Hosseinpour, 2008; Alias et al., 2014) for the samples that were initially higher in gravel (e.g., ØG05a and ØG06b, Table 3). Previous studies estimating the effect of removing gravel from natural backfilled sands (e.g., Bareither et al., 2008) concluded that friction angles varied by only 2° to 4° when removing gravel contents upwards of 30 %. We can expect similar effects here, as our studied samples correspond well to Bareither et al. (2008) both in material (i.e., sand and gravel content) and shear strength test methods (i.e., direct shear test).

Fault zones and fault rocks are weak zones for surface weathering and erosional processes (Jaboyedoff et al., 2004). The increased surface area of the granular fault rock material can increase weathering rates, resulting in a higher content of phyllosilicates by alteration (Janecke and Evans, 1988; Yuan et al., 2019). The effect of surface weathering was mitigated in this study by not sampling directly surface-exposed fault rocks. However, weathering and alteration are likely not only constrained to the surface. The fault rocks are also susceptible to water erosion and groundwater circulation, which could have removed finer gouge material. These processes could have either increased (i.e., weathering and alteration) or decreased (i.e., erosion) the natural clay-gouge content of the studied fault rocks.

The sampling also disturbed the fault rocks' grain configuration and any over-consolidation formed when the faults in the Øygarden Complex were active (Ksienzyk et al., 2016). For clays, in particular, the in-situ grain configuration is significant, as platy minerals can align along the fault slip surface, lowering the frictional strength (Li, 2013; Lee and Kim, 2005). In terms of the over-consolidation ratio, the record of previous stresses that the fault rock has experienced during active periods of faulting is removed (i.e., post-Caledonian reactivations; Ksienzyk et al., 2016). In-situ testing is required to find the over-consolidation ratio, as it is challenging to sample intact granular fault rocks (Chang, 1991; Henderson et al., 2010). If over-consolidation ratios were estimated or known in this study, we would still not be able to replicate the high stress states that the fault rocks experienced prior to and during fault reactivation, as the normal stress ceiling of the direct shear box was 1.75 MPa.

Although several sources for sampling and sample handling errors could affect the friction angles, we think that the samples provide the best available onshore analogue for fault rocks within the Øygarden Fault System. The over-consolidation and grain configuration records are disturbed, but we still retain valuable information on the fault rocks' grain size properties and mineralogy that affect the geomechanical properties. We also believe that the samples' modification by removing particles above 4 mm works in our favour by lowering the resulting friction angles. In fault stability evaluation, it is essential to find the weakest link, as fault reactivation risk assessment of the Øygarden Fault System should involve considering the worst-case scenario.

6.1.2 Fault rock mineralogy

The fact that smectite and illite concentrations could not be determined could have significantly impacted the resulting mineralogical data (Table 5). Smectite and illite are often found as mixed-layer clays, making them more challenging to identify and quantify (Zhou et al., 2018). Smectite, a swelling clay, has low frictional strength and can dilate significantly. This swelling (i.e., dilation) can significantly lower the in-situ effective normal stress (Kameda et al., 2019). Smectite and illite have also been found to reduce the permeability of fault gouges when they are sheared (Ikari et al., 2009). Roughly 10-20 % smectite was expected in the LG fault rock based on previous studies on the Lærdal-Gjende fault (e.g., Tartaglia et al., 2020). However, the LG bulk XRD pattern had a lot of noise (Appendix 4), and smectite could not conclusively be identified from the clay fraction (Appendix 3).

Despite several challenges related to quantifying the fault rock mineralogy, we believe that relative differences between essential clay gouge minerals (i.e., chlorite and kaolinite) and non-phyllosilicates (e.g., quartz and feldspars) are preserved and can still provide useful information. The most significant limitation of the mineralogical data is that important clay minerals such as smectite and illite were not quantified. However, we can make some estimations based on the amount of clay and silt present (Table 5) and data from previous studies on the ØG06a and the Lærdal-Gjende fault (Ksienzyk et al., 2016; Tartaglia et al., 2020).

6.1.3 Fault rock shear strength

Handling techniques and direct shear box test parameters can influence the frictional strength of granular materials (Montanari et al., 2017). Initial density, initial water content, fluid type, homogenous mixing, and shear rate, amongst other factors, can all have an impact (Saito et al., 2006; Behnsen and Faulkner, 2012; Wei et al., 2019).

Strain hardening

The systematic strain hardening effect that occurred in all the samples at the higher normal stresses (Fig. 37) could result from several factors, such as the methodology or the geomechanical properties of the fault rocks (ASTM-D3080, 2011; Montanari et al., 2017; Morrow et al., 1982). However, there were also differences between the tested fault rocks, where LG, ØG05a, and ØG06b underwent significantly more strain hardening across all normal stresses compared to the other fault rocks (Fig. 37). When comparing the grain size properties of the LG, ØG05a, and ØG06b to the other studied fault rocks, we see that these were well graded, sub-angular to angular, and had the highest sand and gravel contents (Table 4). We interpret the LG, ØG05a and ØG06b to have significantly higher strain hardening effects due to grain interlocking (Kohli and Zoback, 2013; Henderson et al., 2010) and the low shear stresses involved, which did not exceed the temporary strength gained by the grain interlocking.

The strain hardening effect can be problematic because it is more difficult to interpret the peak strength. Strictly speaking, this can lead to over-estimating the friction angles. The strain hardening results in higher peaks (maximum σ_n, σ_s obtained) that could increase the slope of the failure envelopes. Despite this, we believe that systematically selecting shear strength at 4 mm shear displacement is the best option in this case, as it removes any interpretation bias.

Non-linear failure envelopes

The non-linear failure envelopes (Fig. 39, Appendix 2) are consistent with previous studies on fault rocks (e.g., Xu, 2018; Schellart, 2000). This is related to:

1 The cohesion of granular materials is highly dependent on normal stress and is overestimated at higher normal stresses (Montanari et al., 2017; Schellart, 2000).

2 Grain-size reduction lowers the friction angle as the grains are continuously fragmented by abrasion and intra-particular fracturing (Henderson et al., 2010; Xu, 2018; Mair and Abe, 2011). We do see more distinct linear curves in the stronger fault rocks (i.e., LG, ØG05a and ØG06b, Appendix 2) compared to the weaker fault rocks (i.e., ØG03, Appendix 2), which suggests that grain-size reduction mechanisms are not affecting the coarser gouges at the low tested stress range (0.1 to 1.5 MPa).

Over-consolidation ratio

From the shear graphs (Fig. 37), it was also evident that the failure curves were more well-defined at the lower normal stress range (0.1 to 0.5 MPa), where over-consolidation ratios were kept constant at 3.5. The upper normal stresses (0.5 to 1.5 MPa) had over-consolidation ratios from 3.5 to 1.17. This corresponds well with previous studies on fault gouges, and it is well documented that higher over-consolidation ratios produce more well-defined failure curves (e.g., Alves Da Silva, 2021; Li et al., 2017; Vithana et al., 2012).

Volumetric response

The volumetric response (i.e., the dilation or compression during shearing) of the fault rock samples is characterized by a general tendency to dilate at lower normal stresses and compress at higher normal stresses (Fig. 38), which is consistent with previous studies (Alves Da Silva, 2021). Several interpretations can be derived from this.

The dilation that occurs when the samples are sheared at lower normal stress could result from grains having enough space to translate by climbing over other grains. At the higher normal stresses, the materials are held tightly together, which does not allow dilation and instead causes the previously discussed strain hardening effect (Morrow et al., 1982). However, this interpretation does not explain the large difference in volumetric response between the fault rocks that underwent significant volumetric response (i.e., ØG05a and ØG06b) and the fault rocks that did not have a significant response (e.g., ØG01 and ØG06a). When taking a closer look at these two volumetric response end members, we can consider the following additional interpretations:

1) The finer gouge materials (e.g., ØG01 and ØG06a) were matrix-supported, high in silt and clay, and had more round particles that could accommodate the displacement by sliding of grains through the finer matrix even at higher normal stresses (Numelin et al., 2007), which does not cause a significant volume change (i.e., sliding failure; Bao et al., 2019). Also, the high clay and silt content allows the finer gouges to compress more, which can be interpreted as a reduced porosity, consistent with the decrease in post-shear water content of 15 % for the ØG01 fault rock (Appendix 1).

2) The coarser fault gouges (i.e., ØG05a and ØG06b) were grain-supported, low in silt and clay, and had more angular particles that could not accommodate displacement due to significant grain-locking (Henderson et al., 2010; Kohli and Zoback, 2013). Intra-particle fracturing or climbing must occur between these locked grains to allow further displacement of the materials. With the low shear stresses involved, frictional climbing is interpreted as the dominant shear failure mechanism, which does cause an increase in volume (i.e., dilation). This dilation leads to increased porosity, which is also observed by the 10 % increase in post-shear water content of the ØG06b fault rock (Appendix 1).

When the strain hardening effect and the volumetric responses of the LG, ØG05a, and ØG06b fault rocks are considered in conjunction, we can see a clear link. The grain size properties of coarser fault rocks favour grain-locking, which causes strain hardening and higher resulting friction angles. This is a direct indication that these fault rocks (i.e., LG, ØG05a, and ØG06b) are geomechanically the strongest, which is consistent with the resulting failure envelopes (Fig. 40), where these immature and coarser fault rocks have friction angles ranging from 26.7° to 31.4° (Table 6). Even the weaker fault rocks experienced strain hardening at the higher normal stresses (1.0 to 1.5 MPa, Fig. 37), which corresponds well with previous studies that indicate that strain hardening at higher normal stress is a typical physical property of fault gouges (Morrow et al., 1982; Chu et al., 1981; Van Diggelen et al., 2010). These results also show clear correlations between the volumetric response, porosity, and grain size properties.

Coefficient of sliding friction

The LG, ØG05a, and ØG06b fault rocks had coefficients of sliding friction (μ_f) above the threshold value of 0.5 (Table 6). This means that these are more likely to exhibit both unstable and stable sliding behaviour through cycles of grain-locking and subsequent stress release (stick-slip; Ikari et al., 2011). The remaining fault rocks (i.e., ØG01, ØG03, and ØG06a) had coefficients of sliding friction below the threshold ($\mu_f < 0.5$) and are interpreted as more likely to undergo stable sliding (i.e., aseismic creep), while the ØG02 was at the threshold value ($\mu_f = 0.5$) where both stable and unstable sliding can occur. This is consistent with the previously discussed strain-hardening effect, where the coarser fault rocks require a higher shear stress to overcome the grain-locking by intra-particular fracturing or abrasion.

6.2 Øygarden Complex friction angle correlations

Fault structural data

The studied fault rocks from the Øygarden Complex were mainly derived from various types of gneisses (i.e., granitic-, tonalitic-, ortho, and migmatitic-gneisses, Ksienzyk et al., 2016; Larsen et al., 2003). The lack of correlation between the friction angle and the original host rocks across both sides of the faults (Fig. 41a) is likely a result of these low variations. This could suggest that the differences in mineralogical composition and grain size properties between the studied fault rocks are primarily controlled by the development and alterations during fault activity or recent weathering. However, it would require a detailed compositional analysis of the wall rock to determine if this is the case.

In terms of fault kinematics (Fig. 41c), the slightly higher friction angle in the strike-slip faults (i.e., ØG05a and ØG06b) could be related to differences in fault displacements compared to the dip-slip faults that follow the predominant NE-SW and E-W extensional trends (Larsen et al., 2003). If the strike-slip faults have lower displacements than the dip-slip faults, this could be accompanied by more immature and coarser fault rocks (Henderson et al., 2010; Xu, 2018). Several studies show a positive correlation between crystalline rock fault core thickness and displacement (Seifried, 2012; Torabi and Berg, 2011), and frictional grain-size reduction mechanisms mainly occur by fault movement. This interpretation is consistent with the low fault core thickness (0.01 m) and high gravel and sand content of the ØG05a fault. The slight but weak, negative (-0.59) correlation between the friction angles and the core width of Øygarden Complex faults (Fig. 41d) also supports this notion. However, the fault core can be challenging to constrain and highly heterogeneous (Lee and Kim, 2005), and the lack of data points severely reduces the confidence.

Fault rock grain size data

When isolating the grain-size parameters (Fig. 42a-f), we observe that the friction angles have fairly strong correlations with the particle size fractions (i.e., gravel, sand, silt, and clay), angularity, and soil grading. These trends correspond well with the previously discussed strain hardening behaviour. The coarse, well-graded, angular, grain-supported gouges had a higher tendency for strain hardening due to grain-locking, resulting in higher friction angles. These trends also correspond well with previous studies on shear strength and grain size data (Li, 2013; Fakhimi and Hosseinpour, 2008; Islam et al., 2019; Alias et al., 2014). However, there are uncertainties related to this, as the clay (2.6 to 16.7 %, Table 4) and gravel (7.8 to 17.0 %, Table 4) fractions are tested only over a small range with limited data points.

The friction angles are also, as previously discussed, highly dependent on test parameters and mineralogy. This makes the trends (Fig. 42a-f) uncertain within the tested range and more so outside the tested range. These grain-size parameters should ideally be combined to predict frictional strength more confidently. Despite this, they do give some initial indication of the friction angles that could be applied to evaluating granitic gneiss fault stabilities of the Øygarden Fault System.

Rock forming minerals

The low average ($\bar{x}$) feldspar content of the Øygarden Complex fault rocks at 25.1 % (Table 5) and the positive correlation between increasing feldspar content and friction angles (Fig. 43b) suggests a weakening behaviour when feldspar content is reduced. This is most likely related to the alteration of feldspar into phyllosilicate minerals (Janecke and Evans, 1988; Yuan et al., 2019), but it is uncertain if this is a result of recent weathering, authigenic alteration during fault activity in the Øygarden Complex, or a combination. We consider alteration by fault activity most likely, as measures were taken not to sample weathered fault gouges. However, as previously discussed, we are not certain about the degree of weathering inside the fault core.

This phyllosilicate alteration is also seen when looking at individual fault rocks (e.g., ØG01), which had a very low feldspar content (18.4 %, Table 5), and a high combined chlorite and kaolinite content (27.8 %, Table 5). Quartz also had a moderately strong but negative correlation between increasing quartz content and friction angle (Fig. 43a). This suggests that there could be a link between the contents of quartz, feldspar, and the alteration products. If we know or can estimate the initial wall composition, and the feldspar and quartz contents of the gouge, we can consider the following interpretation:

- Fault gouges with high quartz, and an anomalously low feldspar content (i.e., lower than wall-rock composition) could indicate a weakened fault rock, matured by phyllosilicate alteration.

This suggests that we can, to a certain degree, predict the presence of phyllosilicates and the subsequent friction angle of the fault gouge by the ratio of feldspar to quartz content of fault gouges if the composition of the surrounding wall rock is known. This could be useful in the absence of detailed XRD clay quantification as an indirect and quick method of determining strength. However, this is accompanied by several uncertainties related to the XRD quantification method applied, the limited data points in this study, and the fact that the friction angles of the Øygarden Complex fault rocks depend on many variables (i.e., grain size properties and clay minerals).

Clays and phyllosilicates

Kaolinite and chlorite had negative correlations between friction angle and increasing mineral clay content (Fig. 43e-f), consistent with previous studies on clay gouges (Tiwari and Marui, 2003; Ikari et al., 2009). The steeper negative trend for kaolinite could suggest that kaolinite is geomechanically weaker than chlorite. Comparing the ØG01 and the ØG06a fault rock mineralogy, we see a similar summed chlorite and kaolinite content (i.e., 27.8% and 30.0 %, Table 5) but a significant difference in friction angle (i.e., 16.8° and 22.7°, Table 6). The ØG01 fault rock had a 10 % higher total content of fines (i.e., clay and silt, Table 4) and a much higher content of kaolinite (i.e., 15.3 % and 3.37 %, Table 5), which makes it difficult to determine if the strength difference is controlled mainly by clay mineralogy or grain size properties. Based on the field observations, the ØG01 appeared to be the most weathered fault. With kaolinite being a common weathering product of feldspars (Janecke and Evans, 1988; Yuan et al., 2019), this could suggest that the ØG01 have been significantly weakened by surface-weathering, which would explain its high kaolinite contents of 15.3 %, compared to the other Øygarden Complex fault rocks.

Although the smectite and illite concentrations could not be quantified, we can estimate their effect on the friction angles. The ØG01, ØG02, ØG03, and the ØG05a fault rocks all contained smectite in the clay fractions. The ØG01, ØG02, and ØG03 had the lowest friction angles of the tested faults (16.7° to 21.6°,

Table 6), while the ØG05a had the highest (i.e., 31.1°). The ØG05a clay-poor gouge was also significantly dilated at lower normal stresses during shearing. With smectite being a highly swelling clay, the presence of smectite could have contributed to the dilation of the ØG05a rock. However, smectite swelling is also associated with a significant decrease in frictional properties (Kameda et al., 2019). When we consider the high friction angle (i.e., 31.1°) and low contents of fines (28.6 %) of the ØG05a fault rock, it does not seem likely that smectite contents were significant. This interpretation corresponds well with the grain size distribution of the ØG05a and the previously mentioned grain-locking, which we believe to predominantly control its dilation and strain hardening effects.

6.3 Discrepancy between clay fraction and clay mineral content

A large discrepancy between the clay size fraction in the grain size distribution data and the mineralogical clay quantification was observed (Table 7). The difference is more significant if muscovite is included as mica, which is common during XRD quantification. Also, if the concentrations of smectite and illite were quantified, the discrepancy might have been even larger. Rietveld refinement analysis gives a relative amount of each constituent mineral which always totals 100%, so selecting additional clay minerals would likely increase the total amount of clays by lowering the quantities of rock forming minerals. Several interpretations might explain this effect:

- The large discrepancy could be attributed to aggregation of clays or clay sticking to larger particles during oven-drying (Sunil and Krishnappa, 2012). These may not be properly dissolved during the wet-sieving process, which could lead to underestimating the finest clay fraction of the sieved material, where the clay mineral aggregates are recorded as coarser particles.

- It could also be related to phyllosilicates being an alteration product of larger grains (e.g., chlorite and kaolinite). When the samples are crushed into powder for bulk XRD analysis, such large and altered chlorite grains could yield a high chlorite content, while when sieving, the same grain could be considered a much coarser particle. The presence of larger altered chlorite grains in the fault gouge (i.e., ØG06b, Fig. 36G) also supports this interpretation.

- Another factor could be that clay minerals are also abundant in the silt fraction.

The large discrepancy means we need to be careful to distinguish between clay fraction and clay mineralogy when analysing fault rocks. The clay grain size fraction is often used to predict friction angle (e.g., Kim et al., 2018), which may be a misleading indicator. There might also be weak clay minerals present in the silt fraction, thus, estimating based only on the clay fraction (i.e., grain size) will not consider the friction angle contribution of frictionally weak, silt-aggregated, clay minerals. This will also depend on the type of clay minerals present and the quantities of clay minerals in the silt fraction.

Table 7. *The difference in clay content from the XRD quantification and the grain size distribution is shown. The grain size clay fraction is subtracted from the XRD clay and mica (clays + muscovite) content. Positive values represent a higher percent of clay minerals in terms of XRD quantification compared to the grain size distributions.*

Sample	**Clay fractions (%)**	**XRD clays (%)**	**XRD mica (%)**	**Δ clays ($\mathbf{XRD\ clay - c.f.}$) (%)**	**Δ Mica ($\mathbf{XRD\ Mica - c.f.}$) (%)**
LG	6.8	9.88	18.89	3.08	12.09
ØG01	16.7	27.8	39.6	11.1	22.90
ØG02	5.7	0	21.62	-5.7	15.92
ØG03	3.8	0	40	-3.8	36.20
ØG05a	7.2	7.57	37.48	0.37	30.28
ØG06a	7.9	30.02	70.62	22.12	62.72
ØG06b	2.6	13.84	41.64	11.24	39.04

6.4 Comparisons of friction angles

The Øygarden Complex and the Lærdal-Gjende fault rocks

The high friction angle of the Lærdal-Gjende fault of 31.4° compares to the coarsest fault rock from the Øygarden Complex, the ØG05a fault rock (31.1°, Table 6). However, the remaining studied fault rocks from the Øygarden Complex were significantly weaker, and the mean friction angle of the Øygarden Complex fault rocks was 23.5° (Fig. 44, Table 8). When considering that the average content of silt, clay, and chlorite in the Øygarden Complex is similar to the Lærdal-Gjende fault, it is evident that the friction angle difference is controlled by the other parameters (Fig. 44, Table 8).

The Lærdal-Gjende differs from the Øygarden Complex faults in the sense that it is a brittle overprint of a mylonitic shear zone and that it has high epidote and a low quartz content (i.e., 25 and 3.7 %), as it is derived from the mafic Jotun Nappe hanging wall block. The mylonitic rock, which predates the faulting, could have contributed to the well-sorted sand grain size distribution (Table 4), which could contribute to the strain hardening and a high corresponding friction angle. This is in some way opposite to what we expect, as the Lærdal-Gjende fault is a part of a highly matured and large-scale fault system, where we would expect grain-size reduction to have substantially weakened the rock. One possibility is that we have sampled a coarser fault gouge lens from the Lærdal-Gjende.

The large difference in feldspar content between the Øygarden Complex fault rocks and the Lærdal-Gjende fault could be largely controlled by the differences in host-rock composition. But the Øygarden Complex fault rocks was also higher in kaolinite content which could suggest that weathering has played a significant role in weakening the Øygarden Complex fault rocks (Fig. 44).

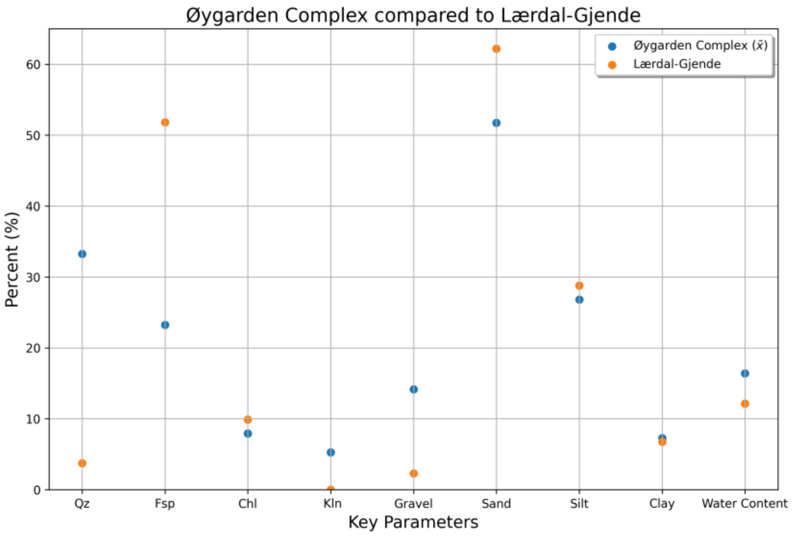

Fig. 44. *Comparison of the sample means ($\overline{x}$) of the key parameters from the Øygarden Complex fault rocks (blue) and the Lærdal-Gjende fault rock (orange). The percent (%) of minerals, grain size fractions, and post-shear water content within the samples is on the y-axis.*

Table 8. *Summary of the mean values of the key-parameters from the Øygarden Complex-derived fault rocks compared to the Lærdal-Gjende fault. Note that μ_f is the coefficient of friction and not coefficient of internal friction.*

	Shear strength			Mineralogy (%)				Grain size data (%)					Structural data		
	Cohesion (kPa)	Friction angle (ϕ)	μ_f	Qz	Fsp	Chl	Kln	Gravel	Sand	Silt	Clay	Fines	Core Width (m)	Orientation (strike)	Dip
Øygarden Complex (mean)	113.7	23.5	0.5	33.2	23.2	7.9	5.3	14.2	51.7	26.8	7.3	34.1	1.5	N-S	77.8
Lærdal-Gjende Fault	78.0	31.4	0.65	3.7	51.8	9.9	0.0	2.3	62.2	28.8	6.8	35.5	1.0	NE-SW	30.0

Synthetic gouges

The Øygarden fault rocks are here compared (Table 9, Fig. 45) to previous studies on synthetic gouges made by mixing clay and sand (i.e., Alves Da Silva, 2021; Tiwari and Marui, 2003; Dafalla, 2013; Ikari et al., 2009). When comparing the friction angles of the Øygarden Complex fault rocks to these previous studies (Table 9, Fig. 45), we see that the Øygarden Complex fault rocks have a significant variation in friction angle over a relatively small range of clay content (2.6 to 16.7 %, Table 3). This emphasises the heterogeneous nature of natural fault rocks.

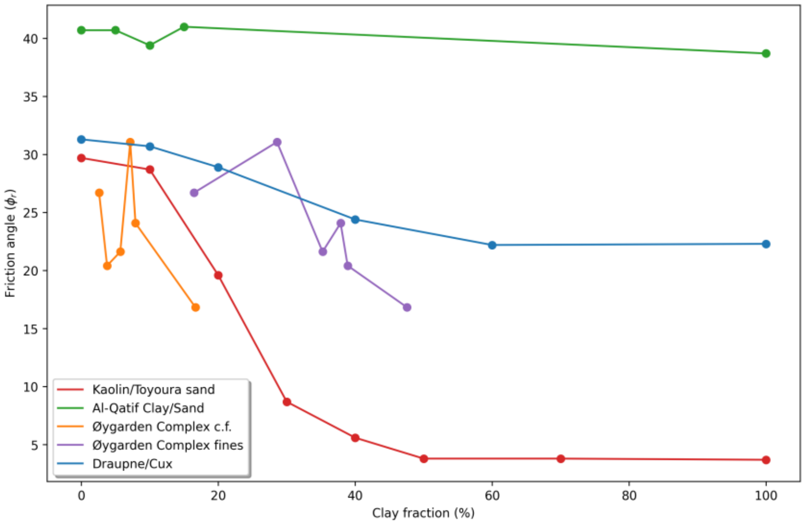

Fig. 45. *Kaolin and Toyoura sand mixture (red) from (Tiwari and Marui, 2003). Al-Qatif clay and sand mixture (green) from Dafalla (2013). Draupne Formation and Cuxhaven sand mixture (blue) from Alves Da Silva (2021). The Øygarden Complex clay fraction (orange). The Øygarden Complex fines fraction consists of the sum of clay and silt contents of each fault rock (purple).*

Alves Da Silva (2021) used the clay-to-sand ratio of Draupne Fm. Shale and Cuxhaven sand to evaluate the frictional properties and how this corresponds to the shale-gouge-ratio, commonly used to predict fault sealing capabilities from seismic data. When we compare these results to the Øygarden Complex fault rocks, we do observe that the highest friction angle of the Øygarden complex fault rocks (i.e., ØG05a) aligns well with the clay fraction of the Cuxhaven sand and Draupne Shale formation mix (Table 9, Fig. 45). Also, when combining the silt and clay contents of the Øygarden Complex fault rocks, we get a similar negative trend to Alves Da Silva (2021).

Another interesting observation is that these natural fault rocks are generally weaker than the synthetic gouges, which could be related to several factors such as differences in the methodology applied and the material properties. One possibility is that synthetic gouges, in general, could be more well-graded with more even grain-size distributions. The synthetic gouges are typically ground down from well-sorted sedimentary rocks (e.g., Alves Da Silva, 2021) to evaluate fault-bound reser-voirs juxtaposed to sedimentary rocks, industrial-grade materials, or rocks and soils related to evaluating slope stability (e.g., Tiwari and Marui, 2003). The weakest studied fault rock from the Øygarden Complex (i.e., ØG01, 16.8°) corresponds well to the clay-rich chlorite and illite gouge from Ikari et al. (2009). However, Ikari et al. (2009) used biaxial (-triaxial) testing and a much higher normal stress test range (12 to 58 MPa, Table 9).

Table 9. *Comparison of the Øygarden Complex fault rock friction angles to previous synthetic gouge studies*.

Sample	Reference	Method	Fault rock/Material	Normal stresses	Sand f. (%)	Clay f. (%)	Clay minerals	ϕ	ϕ_r
ØG01		Direct Shear (drained, saturated)	Fault Gouge	0.1 to 1.5 Mpa	44.7	16.7	Chl, Ilt, Sme, Kln	-	16.8
ØG02			Fault Gouge		48.2	5.7	Ilt (?), Sme	-	21.6
ØG03			Fault Gouge		47.5	3.8	Ilt (?), Sme	-	20.4
ØG05a			Fault Gouge		54.4	7.2	Chl, Ilt, Sme, Kln	-	31.1
ØG06a			Fault Gouge		48.4	7.9	Chl, Ilt, Kln	-	24.1
ØG06b			Fault Gouge		67.3	2.6	Chl, Ilt, Kln	-	26.7
Cuxhaven sand, Draupne Formation Shale	(Alves Da Silva, 2021)	Direct shear (drained, saturated)	Synthetic gouge (sand/clay mix)	0.5 to 1.5 Mpa	100	0	Sme, Kln	-	31.3
					90	10		-	30.7
					80	20		-	28.9
					60	40		-	24.4
					40	60		-	22.2
					0	100		-	22.3
Landslides and debris flows	(Tiwari and Marui, 2003)	Ring shear (drained, saturated)	Commercial kaolin and Toyoura sand mixture		100	0	Kln	-	29.7
					90	10		-	28.7
					80	20		-	19.6
					70	30		-	8.7
					60	40		-	5.6
					50	50		-	3.8
					30	70		-	3.8
					0	100		-	3.7
Al-Qatif Clay, industrial fine-grained sand	(Dafalla, 2013)	Direct shear (drained, saturated)	Synthetic clay-sand mixtures		100	0		40.7	-
					95	5		40.7	-
					90	10		39.4	-
					85	15		41	-
					0	100		38.7	-
	(Ikari et al., 2009)	Biaxial testing under true-triaxial conditions	Synthetic Montmorillonite/quartz gouge	12 to 58 MPa	50	50	Sme	10.8 to 13.0	-
			Illite shale		50	50	Ilt and chl	15.1 to 17.7	-
			Chlorite Schist		50	50		15.1 to 17.7	-

Natural fault gouges

Limited data from natural fault rocks, specifically granitic gneiss-derived gouges, and the variability in testing methods make comparison with previous studies challenging. Seo et al. (2016) conducted a numerical analysis of 584 in-situ and laboratory tests of natural fault rocks from gneiss, granite, andesite, phyllite, schist and shale. They found friction angles varying from 14.7° to 44°. The studied fault rocks from the Øygarden Complex plots comfortably within this range, and the coarsest gouge (i.e., the ØG05a) corresponds well with Seo et al. (2016) results from gneissic- and granite-derived gouges and fault breccias (Table 10).

Table 10. *Comparison of the Øygarden Complex fault rock friction angles to previous natural fault rock and fault gouge studies.*

Sample	Reference	Method	Fault rock/Material	Normal stresses	Sand f. (%)	Clay f. (%)	Clay minerals	ϕ	ϕ_r
ØG01		Direct Shear (drained, saturated)	Fault Gouge	0.1 to 1.5 Mpa	44.7	16.7	Chl, Ilt, Sme, Kln	-	16.8
ØG02			Fault Gouge		48.2	5.7	Ilt (?), Sme	-	21.6
ØG03			Fault Gouge		47.5	3.8	Ilt (?), Sme	-	20.4
ØG05a			Fault Gouge		54.4	7.2	Chl, Ilt, Sme, Kln	-	31.1
ØG06a			Fault Gouge		48.4	7.9	Chl, Ilt, Kln	-	24.1
ØG06b			Fault Gouge		67.3	2.6	Chl, Ilt, Kln	-	26.7
Gneiss	(Seo et al., 2016)	Direct shear, triaxial compression, in-situ borehole shear tests	Fault Gouge	-	-	-	-	29	-
			Cataclasite		-	-	-	31	-
			Fault Breccia		-	-	-	30.9	-
			Damage zone		-	-	-	31	-
Granite			Damage zone		-	-	-	32.3	-

6.5 Applications for modelling and de-risking the Øygarden Fault System

The lack of input data for fault stability modelling of crystalline basement involved fault zones (i.e., granitic gneisses), such as the Øygarden Fault System, was a motivator for this study. We find both strong and weak fault gouges in the Øygarden Complex, with internal angles of friction ranging from 16.8° to 31.1° (0.1 to 1.5 MPa). The friction angles are visualized here by assuming that the data follows a normal distribution centred around the sample means ($\overline{x}$) in Fig. 46. Note that the sample size is very small (i.e., 6 fault rocks), so more data is required to find the true distribution (i.e., if it is normally distributed). The distribution representing the entire tested range (0.1 to 1.5 MPa) has a mean internal angle of friction of 23.5°, with an assumed standard deviation of 5° (Fig. 46). The 95 % confidence interval is in the range of 19.5° to 27.5° (i.e., 95 % chance that the true population mean could be in this range).

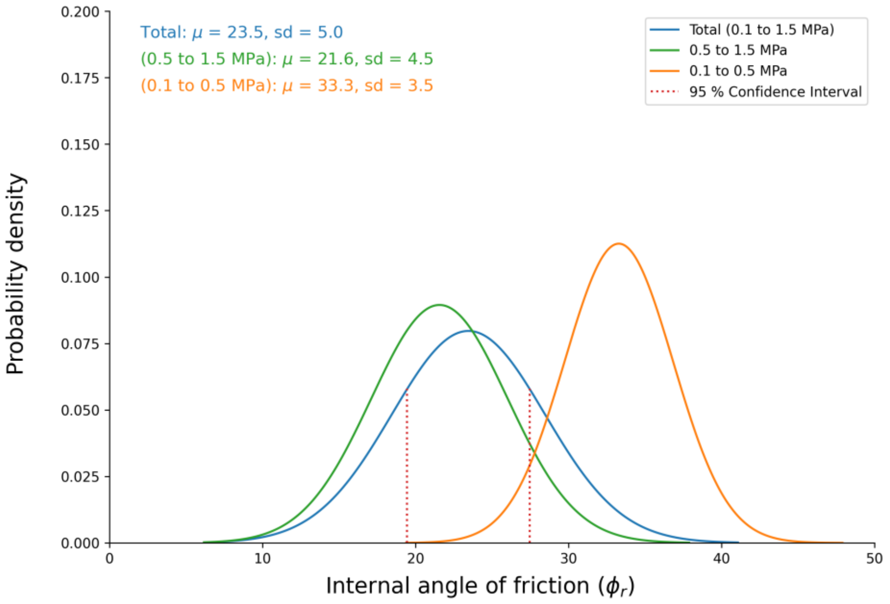

Fig. 46. *Normally distributed residual friction angles (ϕ_r). The total failure envelopes (blue), uses all available tested normal stresses ($\sigma_n = 0.1, 0.3, 0.5, 1.0, 1.5\ MPa$), while the lower and upper uses the lower and upper three points.*

The normal stress test range (i.e., 0.1 to 1.5 MPa) is still much lower than what would be expected at the Smeaheia reservoir depths. With lithostatic and hydrostatic stress states, the expected in-situ stresses of the Beta site are likely to be in the magnitudes of 20 MPa (Wu et al., 2021; Mulrooney et al., 2020). The significant difference in normal stresses means that extrapolation to higher normal stresses must consider the non-linear failure envelope of the fault rocks, where friction angle will decrease and cohesion will increase as a function of increased depth (Montanari et al., 2017; Schellart, 2000). The fault rocks of the Øygarden Fault System are also expected to be more matured by grain-size reduction due to the relatively large displacements of the Øygarden Fault System at the Beta site (> 300 m; Wu et al., 2021).

The varying friction angles (i.e., 16.8° to 31.1°) coupled with the average coefficient of friction (μ_f) of 0.50, means that the studied Øygarden Complex fault gouges are in the transition between the stable and unstable slip regimes at these low normal stresses (Ikari et al., 2011). The following interpretations can be explored:

- The faults with mature and weaker fault gouges (i.e., ØG01, ØG03, ØG06a) that follow the predominant regional E-W to NE-SW extensional trends are interpreted as more likely to favour reactivation by stable sliding. These fault rocks had coefficients of sliding friction $\mu_f < 0.5$.

- Smaller conjugate or Riedel-type faults that do not follow the regional E-W trend (i.e., ØG05a, ØG06b) are more commonly associated with immature and stronger fault gouges (-breccias) and might display more unstable stick-slip behaviour through cycles of grain-locking and stress release. These fault rocks had coefficients of sliding friction μ_f > 0.5.

Considering these two interpretations, the heterogeneous nature of natural fault zones, potential weathering in the Øygarden Complex, and the low stresses applied to the gouges, the stability that the tested fault rocks could provide is still highly uncertain. The latest significant fault reactivation that produced fault gouges onshore in the Øygarden Complex was during the Early Cretaceous, at ca. 120 to 110 Ma (Ksienzyk et al., 2016). However, the northern parts of the Øygarden Fault System have been interpreted to have been active up until the Holocene (Bell et al., 2014), and seismic events are, to the present day, still recorded in the Øygarden Complex and the North Sea (Olesen et al., 2013; Mulrooney et al., 2020; Wu et al., 2021). Rutqvist et al. (2016) also argue that reservoirs juxtaposed to crystalline basement rocks should be avoided due to the increased likelihood of induced seismicity. Still, no seismic events have been reported from any CO_2 storage project to the present date (Rutqvist et al., 2016), but this is also depends on the required scale of the CCS project, and the injected CO_2 volumes.

7 Summary and conclusions

We conducted a series of direct shear box tests to determine the friction angles of natural fault rocks from the Øygarden Complex. The goal was to contribute to increasing available shear strength inputs for modelling of fault stability, and potential for induced seismicity, of the Øygarden Fault System. The Øygarden Complex juxtaposes the Beta storage site (i.e., Smeaheia fault block) through the basin bounding N-S striking Øygarden Fault System; thus, the onshore fault rocks of the Øygarden Complex provide a highly accessible onshore analogue. Additionally, we wanted to investigate if the fault rock friction angles could be correlated to fault structural data, grain size properties, and mineralogical data.

The onshore faults from the Øygarden Complex were predominantly N-S trending, parallel to the dominating N-S trend of the Øygarden Fault System. The studied fault rocks were derived from the Øygarden Complex granitic gneisses and had friction angles (ϕ_r) at 4 mm shear displacement (d) ranging from 16.8° to 31.3° with a sample mean $(\overline{x})$ of 23.5°. The failure envelopes were non-linear, characterized by an increased cohesion and decreased friction angle at the higher normal stresses (0.5 to 1.5 MPa).

The gouges underwent systematic strain hardening, especially at the higher normal stresses (0.5 to 1.5 MPa). The coarser fault rocks underwent significant strain hardening and dilation also at lower normal stresses (0.3 to 0.5 MPa) due to grain-locking. This is closely related to the angularity of the particles, the grain-size distributions of the fault rocks, and the effective normal stresses applied.

The tested fault gouges were predominantly sand dominated, with sand contents ranging from 44.7 to 67.3 % and clay contents ranging from 2.6 to 16.7 %. The finer gouges that were matrix-supported, high in silt and clay, and had more round particles, underwent compression, less strain hardening, and had lower friction angles. The coarser gouges underwent dilation, significant strain hardening, and had higher resulting friction angles. The volumetric responses (i.e., dilation or compression) were accompanied by a corresponding change in porosity and density.

Faults, as highlighted in this work, are highly heterogeneous and can contain various fault rocks, which complicates the procedure. Based on the findings of this study, the following conclusions are proposed:

- The friction angles of the Øygarden Complex fault rocks (16.8 to 31.3°, $\overline{x} = 23.5$) are generally much lower than both the Lærdal-Gjende fault rock (31.4°) and synthetic gouge mixtures.

- Grain-size clay fraction does not correspond with the quantities of clay minerals of the studied gouges. Care should be taken to distinguish these very different parameters in fault rock classification.

- Feldspar and quartz contents are closely related to the quantities of altered phyllosilicates of gneissic-derived fault rocks and could be used to predict the quantity of clay minerals in natural fault gouges.

- No convincing correlations between friction angles of the Øygarden Complex fault rocks and the structural fault parameters were identified.

- All the tested fault gouges display strain hardening behaviour at higher normal stresses (i.e., 0.5 to 1.5 MPa) consistent with previous studies (Morrow et al., 1982; Alves Da Silva, 2021). The fault gouges higher in clay and silt content tend to compress during shear, while the coarser gouges dilate.

- We propose using grain size distribution (i.e., grain size fractions, angularity, and grain- or matrix-supported) to characterize fault rocks. Grain size data provides a good initial predictor for frictional strength properties in terms of fault stability. The mineralogy in terms of clay minerals becomes increasingly more important if the clay and silt fractions are higher.

- The average coefficient of sliding friction (μ_f) of the Øygarden Complex fault rocks at 1.5 MPa normal stress and 4 mm shear displacement is at the threshold value for stable to unstable sliding of μ_f = 0.5 (Ikari et al., 2011).

Suggestions for future work

This work has highlighted some critical difficulties related to characterizing fault rocks. Generally, large datasets are needed to predict the fault stability contribution of fault rocks confidently. This is especially true given the heterogeneous nature of fault zones and fault cores, which means that the resulting friction angles could be a direct result of the sampling methodology.

- Sampling a much higher quantity of onshore faults could therefore reveal trends in terms of structural data if they exist.

- It would also be useful to quantify the amount of clay minerals derived from the faulting compared to surface weathering in the Øygarden Complex. This could be used to estimate the weakening by weathering (i.e., increasing phyllosilicates). This weakening effect could be applied the Øygarden Fault System, as the Øygarden Complex basement at the Smeaheia site could also be weathered.

- Constraining the damage zones of the studied faults could be used to estimate the fault displacements (Torabi et al., 2020). This data could then be applied to approximate the maturity of the Øygarden Complex fault rocks as a function of the displacement. If the fault displacement at the Beta site is known from seismic data, then this can be used to estimate the maturity of the fault rocks at depth. This would require estimating the contribution of the gouge’s phyllosilicate concentrations by weathering or alterations (non-frictional).

- Additionally, more in-depth analysis of the clay mineralogy and tests at higher normal and shear stresses would be a natural next step to simulate how these fault rocks would react under reservoir conditions.

- Finally, it would be interesting to test the frictional properties of the Øygarden Complex fault rocks (fault rock contribution from the footwall) with an interface of sandstone or shale (fault rock contribution from the hanging wall), as this could increase the complexity and perhaps give more site-specific data (i.e., the Smeaheia site).

8 References

ALI, A., CHIANG, Y. W. & SANTOS, R. M. 2022. X-ray Diffraction Techniques for Mineral Characterization: A Review for Engineers of the Fundamentals, Applications, and Research Directions. *Minerals,* 12**,** 205.

ALIAS, R., KASA, A. & TAHA, M. 2014. Particle size effect on shear strength of granular materials in direct shear test. *International Journal of Civil and Environmental Engineering,* 8**,** 1144-1147.

ALVES DA SILVA, D. C. 2021. *Experimental study addressing fault slip Implications for derisking of the Smeaheia potential CO2 storage site.*

ASTM-D3080 2011. Standard Test Method for Direct Shear Test of Soils Under Consolidated Drained Conditions. ASTM International.

ASTM-D6913 2009. Standard Test Methods for Particle-Size Distribution (Gradation) of Soils Using Sieve Analysis. ASTM International.

BAO, H., QI, Q., LAN, H., YAN, C., XU, W., LIU, X. & LI, L. 2019. Shear Mechanical Behaviours and Multistrength Parameter Characteristics of Fault Gouge. *Advances in Civil Engineering,* 2019.

BARDET, J.-P. 1997. *Experimental soil mechanics*, Prentice Hall.

BAREITHER, C. A., BENSON, C. H. & EDIL, T. B. 2008. Comparison of shear strength of sand backfills measured in small-scale and large-scale direct shear tests. *Canadian Geotechnical Journal,* 45**,** 1224-1236.

BEHNSEN, J. & FAULKNER, D. R. 2012. The effect of mineralogy and effective normal stress on frictional strength of sheet silicates. *Journal of Structural Geology,* 42**,** 49-61.

BELL, R. E., JACKSON, C. A. L., WHIPP, P. S. & CLEMENTS, B. 2014. Strain migration during multiphase extension: Observations from the northern North Sea. *Tectonics,* 33**,** 1936-1963.

BRODIE, K., FETTES, D., HARTE, B. & SCHMID, R. 2007. Structural terms including fault rock terms. *Recommendations by the IUGS Subcommission*.

CAPPA, F. & RUTQVIST, J. 2011. Impact of CO2 geological sequestration on the nucleation of earthquakes. *Geophysical Research Letters,* 38.

CHANG, M. 1991. Interpretation of overconsolidation ratio from in situ tests in recent clay deposits in Singapore and Malaysia. *Canadian Geotechnical Journal,* 28**,** 210-225.

CHU, C., WANG, C. & LIN, W. 1981. Permeability and frictional properties of San Andreas fault gouges. *Geophysical Research Letters,* 8**,** 565-568.

CLADOUHOS, T. T. 1999. Shape preferred orientations of survivor grains in fault gouge. *Journal of Structural Geology,* 21**,** 419-436.

DAFALLA, M. A. 2013. Effects of clay and moisture content on direct shear tests for clay-sand mixtures. *Advances in Materials Science and Engineering,* 2013.

DOBLAS, M., MAHECHA, V. & HOYOS, M. 1997. Slickenside and fault surface kinematic indicators on active normal faults of the Alpine Betic cordilleras, Granada, southern Spain. *Journal of Structural Geology,* 19**,** 159-170.

DOEBELIN, N. & KLEEBERG, R. 2015. Profex: a graphical user interface for the Rietveld refinement program BGMN. *Journal of applied crystallography,* 48**,** 1573-1580.

DUFFY, O. B., BELL, R. E., JACKSON, C. A.-L., GAWTHORPE, R. L. & WHIPP, P. S. 2015. Fault growth and interactions in a multiphase rift fault network: Horda Platform, Norwegian North Sea. *Journal of Structural Geology,* 80**,** 99-119.

ENGELDER, J. T. 1974. Cataclasis and the generation of fault gouge. *Geological Society of America Bulletin,* 85**,** 1515-1522.

FÆRSETH, R. 1996. Interaction of Permo-Triassic and Jurassic extensional fault-blocks during the development of the northern North Sea. *Journal of the Geological Society,* 153**,** 931-944.

FAKHIMI, A. & HOSSEINPOUR, H. The role of oversize particles on the shear strength and deformational behavior of rock pile material. The 42nd US Rock Mechanics Symposium (USRMS), 2008. OnePetro.

FARRELL, N., DEBENHAM, N., WILSON, L., WILSON, M., HEALY, D., KING, R. C., HOLFORD, S. P. & TAYLOR, C. 2021. The effect of authigenic clays on fault zone permeability. *Journal of Geophysical Research: Solid Earth,* 126**,** e2021JB022615.

FAULKNER, D., JACKSON, C., LUNN, R., SCHLISCHE, R., SHIPTON, Z., WIBBERLEY, C. & WITHJACK, M. 2010. A review of recent developments concerning the structure, mechanics and fluid flow properties of fault zones. *Journal of Structural Geology,* 32**,** 1557-1575.

FOSSEN, H. 2000. Extensional tectonics in the Caledonides: Synorogenic or postorogenic? *Tectonics,* 19**,** 213-224.

FOSSEN, H. 2016. *Structural geology*, Cambridge university press.

FOSSEN, H., GABRIELSEN, R. H., FALEIDE, J. I. & HURICH, C. A. 2014. Crustal stretching in the Scandinavian Caledonides as revealed by deep seismic data. *Geology,* 42**,** 791-794.

FOSSEN, H. & HURICH, C. A. 2005. The Hardangerfjord Shear Zone in SW Norway and the North Sea: a large-scale low-angle shear zone in the Caledonian crust. *Journal of the Geological Society,* 162**,** 675-687.

FOSSEN, H., KHANI, H. F., FALEIDE, J. I., KSIENZYK, A. K. & DUNLAP, W. J. 2017. Post-Caledonian extension in the West Norway–northern North Sea region: the role of structural inheritance. *Geological Society, London, Special Publications,* 439**,** 465-486.

GRIGOLI, F., CESCA, S., RINALDI, A. P., MANCONI, A., LOPEZ-COMINO, J. A., CLINTON, J., WESTAWAY, R., CAUZZI, C., DAHM, T. & WIEMER, S. 2018. The November 2017 M w 5.5 Pohang earthquake: A possible case of induced seismicity in South Korea. *Science,* 360**,** 1003-1006.

HENDERSON, I. H., GANERØD, G. V. & BRAATHEN, A. 2010. The relationship between particle characteristics and frictional strength in basal fault breccias: Implications for fault-rock evolution and rockslide susceptibility. *Tectonophysics,* 486**,** 132-149.

IKARI, M. J., MARONE, C. & SAFFER, D. M. 2011. On the relation between fault strength and frictional stability. *Geology,* 39**,** 83-86.

IKARI, M. J., SAFFER, D. M. & MARONE, C. 2009. Frictional and hydrologic properties of clay-rich fault gouge. *Journal of Geophysical Research: Solid Earth,* 114.

ISLAM, M. N., SIDDIKA, A., HOSSAIN, M. B., RAHMAN, A. & ASAD, M. A. 2019. Effect of particle size on the shear strength behavior of sands. *arXiv preprint arXiv:1902.09079*.

JABOYEDOFF, M., BAILLIFARD, F., BARDOU, E. & GIROD, F. 2004. The effect of weathering on Alpine rock instability. *Quarterly Journal of Engineering Geology and Hydrogeology,* 37**,** 95-103.

JANECKE, S. U. & EVANS, J. P. 1988. Feldspar-influenced rock rheologies. *Geology,* 16**,** 1064-1067.

KAMEDA, J., UNO, M., CONIN, M., UJIIE, K., HAMADA, Y. & KIMURA, G. 2019. Fault weakening caused by smectite swelling. *Earth, Planets and Space,* 71**,** 1-7.

KIM, D., NAM, B. H. & YOUN, H. 2018. Effect of clay content on the shear strength of clay–sand mixture. *International Journal of Geo-Engineering,* 9**,** 1-12.

KOHLI, A. H. & ZOBACK, M. D. 2013. Frictional properties of shale reservoir rocks. *Journal of geophysical research: solid earth,* 118**,** 5109-5125.

KSIENZYK, A. K., WEMMER, K., JACOBS, J., FOSSEN, H., SCHOMBERG, A. C., SÜSSENBERGER, A., LÜNSDORF, N. & BASTESEN, E. 2016. Post-Caledonian brittle deformation in the Bergen area, West Norway: results from K–Ar illite fault gouge dating. *Norwegian Journal of Geology,* 96**,** 275-299.

LARSEN, Ø., FOSSEN, H., LANGELAND, K. & PEDERSEN, R.-B. 2003. Kinematics and timing of polyphase post-Caledonian deformation in the Bergen area, SW Norway. *Norwegian Journal of Geology/Norsk Geologisk Forening,* 83.

LEE, H.-K. & KIM, H. S. 2005. Comparison of structural features of the fault zone developed at different protoliths: crystalline rocks and mudrocks. *Journal of Structural Geology,* 27**,** 2099-2112.

LI, D., YIN, K., GLADE, T. & LEO, C. 2017. Effect of over-consolidation and shear rate on the residual strength of soils of silty sand in the Three Gorges Reservoir. *Scientific Reports,* 7**,** 1-11.

LI, Y. 2013. Effects of particle shape and size distribution on the shear strength behavior of composite soils. *Bulletin of Engineering Geology and the Environment,* 72**,** 371-381.

LIU, Q., BUTTON, E. & KLIMA, K. 2007. Investigation for probabilistic prediction of shear strength properties of clay-rich fault gouge in the Austrian Alps. *Engineering geology,* 94**,** 103-121.

LOGAN, J. Experimental studies of simulated gouge and their application to studies of natural fault zones. Proceedings of conference VIII-analysis of actual fault zones in bedrock, 1979. 305-343.

LOMMLER, J. C. 2012. *Geotechnical problem solving,* John Wiley & Sons.

LOUCKS, R. G. 1999. Paleocave carbonate reservoirs: Origins, burial-depth modifications, spatial complexity, and reservoir implications. *AAPG bulletin,* 83**,** 1795-1834.

MAIR, K. & ABE, S. 2011. Breaking up: comminution mechanisms in sheared simulated fault gouge. *Pure and Applied Geophysics,* 168**,** 2277-2288.

MARONE, C. & SCHOLZ, C. 1989. Particle-size distribution and microstructures within simulated fault gouge. *Journal of Structural Geology,* 11**,** 799-814.

MONTANARI, D., AGOSTINI, A., BONINI, M., CORTI, G. & VENTISETTE, C. D. 2017. The use of empirical methods for testing granular materials in analogue modelling. *Materials,* 10**,** 635.

MORROW, C., SHI, L. & BYERLEE, J. 1982. Strain hardening and strength of clay-rich fault gouges. *Journal of Geophysical Research: Solid Earth,* 87**,** 6771-6780.

MOUM, J. 1965. Falling drop used for grain-size analysis of fine-grained materials. *Sedimentology,* 5**,** 343-347.

MULROONEY, M. J., OSMOND, J. L., SKURTVEIT, E., FALEIDE, J. I. & BRAATHEN, A. 2020. Structural analysis of the Smeaheia fault block, a potential CO2 storage site, northern Horda Platform, North Sea. *Marine and Petroleum Geology,* 121**,** 104598.

NUMELIN, T., MARONE, C. & KIRBY, E. 2007. Frictional properties of natural fault gouge from a low-angle normal fault, Panamint Valley, California. *Tectonics,* 26.

OLESEN, O., BUNGUM, H., DEHLS, J., LINDHOLM, C., PASCAL, C. & ROBERTS, D. 2013. Neotectonics, seismicity and contemporary stress field in Norway–mechanisms and implications. *Quaternary Geology of Norway, Geological Survey of Norway Special Publication,* 13**,** 145-174.

PHILLIPS, W. J. 1972. Hydraulic fracturing and mineralization. *Journal of the Geological Society,* 128**,** 337-359.

RUTQVIST, J. 2012. The geomechanics of CO2 storage in deep sedimentary formations. *Geotechnical and Geological Engineering,* 30**,** 525-551.

RUTQVIST, J., RINALDI, A. P., CAPPA, F., JEANNE, P., MAZZOLDI, A., URPI, L., GUGLIELMI, Y. & VILARRASA, V. 2016. Fault activation and induced seismicity in geological carbon storage–Lessons learned from recent modeling studies. *Journal of Rock Mechanics and Geotechnical Engineering,* 8**,** 789-804.

SAITO, R., FUKUOKA, H. & SASSA, K. 2006. Experimental study on the rate effect on the shear strength. *Disaster mitigation of debris flows, slope failures and landslides***,** 421-427.

SCARINGI, G. & DI MAIO, C. 2016. Influence of displacement rate on residual shear strength of clays. *Procedia Earth and Planetary Science,* 16**,** 137-145.

SCHELLART, W. 2000. Shear test results for cohesion and friction coefficients for different granular materials: scaling implications for their usage in analogue modelling. *Tectonophysics,* 324**,** 1-16.

SEIFRIED, D. T. 2012. *Faults architecture and their scaling relationships: Insights into fault core thickness and fault displacement.* The University of Bergen.

SEO, Y.-S., YUN, H.-S., BAN, J.-D. & LEE, C.-K. 2016. Mechanical properties of fault rocks in Korea. *The Journal of Engineering Geology,* 26**,** 571-581.

SIBSON, R. H. 1977. Fault rocks and fault mechanisms. *Journal of the Geological Society,* 133**,** 191-213.

SKURTVEIT, E., CHOI, J. C., OSMOND, J., MULROONEY, M. & BRAATHEN, A. 3D fault integrity screening for Smeaheia CO2 injection site. 14th Greenhouse Gas Control Technologies Conference Melbourne, 2018. 21-26.

STORTI, F., BILLI, A. & SALVINI, F. 2003. Particle size distributions in natural carbonate fault rocks: insights for non-self-similar cataclasis. *Earth and Planetary Science Letters,* 206**,** 173-186.

SUNIL, B. & KRISHNAPPA, H. 2012. Effect of drying on the index properties of lateritic soils. *Geotechnical and Geological Engineering,* 30**,** 869-879.

TARTAGLIA, G., VIOLA, G., VAN DER LELIJ, R., SCHEIBER, T., CECCATO, A. & SCHÖNENBERGER, J. 2020. "Brittle structural facies" analysis: A diagnostic method to unravel and date multiple slip events of long-lived faults. *Earth and Planetary Science Letters,* 545**,** 116420.

TEMBE, S., LOCKNER, D. A. & WONG, T. F. 2010. Effect of clay content and mineralogy on frictional sliding behavior of simulated gouges: Binary and ternary mixtures of quartz, illite, and montmorillonite. *Journal of Geophysical Research: Solid Earth,* 115.

TIWARI, B. & MARUI, H. 2003. Estimation of residual shear strength for bentonite-kaolin-Toyoura sand mixture. *Journal of the Japan Landslide Society,* 40**,** 124-133.

TJIA, H. D. 2014. Fault-plane markings as displacement sense indicators. *Indonesian Journal on Geoscience,* 1**,** 151-163.

TORABI, A. & BERG, S. S. 2011. Scaling of fault attributes: A review. *Marine and Petroleum Geology,* 28**,** 1444-1460.

TORABI, A., ELLINGSEN, T., JOHANNESSEN, M., ALAEI, B., ROTEVATN, A. & CHIARELLA, D. 2020. Fault zone architecture and its scaling laws: where does the damage zone start and stop? *Geological Society, London, Special Publications,* 496**,** 99-124.

TORABI, A., JOHANNESSEN, M. U. & ELLINGSEN, T. S. S. 2019. Fault core thickness: Insights from siliciclastic and carbonate rocks. *Geofluids,* 2019.

VAN DIGGELEN, E. W., DE BRESSER, J. H., PEACH, C. J. & SPIERS, C. J. 2010. High shear strain behaviour of synthetic muscovite fault gouges under hydrothermal conditions. *Journal of Structural Geology,* 32**,** 1685-1700.

VITHANA, S. B., NAKAMURA, S., KIMURA, S. & GIBO, S. 2012. Effects of overconsolidation ratios on the shear strength of remoulded slip surface soils in ring shear. *Engineering geology,* 131**,** 29-36.

WANG, L., KWIATEK, G., RYBACKI, E., BONNELYE, A., BOHNHOFF, M. & DRESEN, G. 2020. Laboratory study on fluid-induced fault slip behavior: The role of fluid pressurization rate. *Geophysical Research Letters,* 47**,** e2019GL086627.

WEI, Y., WU, X., XIA, J., MILLER, G. A., CAI, C., GUO, Z. & HASSANIKHAH, A. 2019. The effect of water content on the shear strength characteristics of granitic soils in South China. *Soil and Tillage Research,* 187**,** 50-59.

WHITE, J. A. & FOXALL, W. 2016. Assessing induced seismicity risk at CO2 storage projects: Recent progress and remaining challenges. *International Journal of Greenhouse Gas Control,* 49**,** 413-424.

WHITNEY, D. L. & EVANS, B. W. 2010. Abbreviations for names of rock-forming minerals. *American mineralogist,* 95**,** 185-187.

WIEST, J., JACOBS, J., FOSSEN, H., GANERØD, M. & OSMUNDSEN, P. 2021. Segmentation of the Caledonian orogenic infrastructure and exhumation of the Western Gneiss Region during transtensional collapse. *Journal of the Geological Society,* 178.

WIEST, J. D., FOSSEN, H. & JACOBS, J. 2020. Shear zone evolution during core complex exhumation – Implications for continental detachments. *Journal of Structural Geology,* 140**,** 104139.

WIEST, J. D., JACOBS, J., KSIENZYK, A. K. & FOSSEN, H. 2018. Sveconorwegian vs. Caledonian orogenesis in the eastern Øygarden Complex, SW Norway–geochronology, structural constraints and tectonic implications. *Precambrian Research,* 305**,** 1-18.

WOODCOCK, N. H. & MORT, K. 2008. Classification of fault breccias and related fault rocks. *Geological Magazine,* 145**,** 435-440.

WU, L., THORSEN, R., OTTESEN, S., MENEGUOLO, R., HARTVEDT, K., RINGROSE, P. & NAZARIAN, B. 2021. Significance of fault seal in assessing CO2 storage capacity and containment risks–an example from the Horda Platform, northern North Sea. *Petroleum Geoscience,* 27.

XU, Y. 2018. Shear strength of granular materials based on fractal fragmentation of particles. *Powder Technology*, 333**,** 1-8.

YUAN, G., CAO, Y., SCHULZ, H.-M., HAO, F., GLUYAS, J., LIU, K., YANG, T., WANG, Y., XI, K. & LI, F. 2019. A review of feldspar alteration and its geological significance in sedimentary basins: From shallow aquifers to deep hydrocarbon reservoirs. *Earth-science reviews*, 191**,** 114-140.

ZHOU, X., LIU, D., BU, H., DENG, L., LIU, H., YUAN, P., DU, P. & SONG, H. 2018. XRD-based quantitative analysis of clay minerals using reference intensity ratios, mineral intensity factors, Rietveld, and full pattern summation methods: A critical review. *Solid Earth Sciences*, 3**,** 16-29.

ZOBACK, M. D. 2010. *Reservoir geomechanics*, Cambridge university press.

9 Appendix

Appendix 1

Appendix 1. *Overview of experimentational data of all the direct shear box experiments performed. 30 total tests were performed at different effective normal stresses (second column), and by using varying over-consolidation ratios (third column). Dry density, void ratio and water content is calculated both pre-shear and post-shear. Peak strength values (effective shear stress, effective normal stress) at 4 mm horizontal displacement change are the values used to create the failure envelopes by linear regression (least square error regression). ØG06b experienced systematic tilting which is most likely caused by it being the coarsest sample. The experiment ØG06b_b was used to test the effect of over-consolidation ratio at the residual shear strength peak. No significant difference in measured shear stress was observed at 4 mm horizontal displacement change.*

Sample	Consolidation			Pre Shear				Post Shear			Residual Peak (4 mm)		Comment
	Normal Stress	Consolidation normal stress	OCR	Weight, wet (g)	Dry density initial (g/cm^3)	Void Ratio initial	Water Content initial (%)	Dry density final (g/cm^3)	Void Ratio (final)	Water Content final (%)	Shear Stress (kPa)	Effective Normal Stress (kPa)	
LG	100	350	3.50	226.63	2.06	0.28	15.00	2.31	0.15	13.10	100.04	102.72	
LG	300	1050	3.50	226.20	2.06	0.29	15.00	2.40	0.10	11.67	296.77	303.24	
LG	500	1750	3.50	226.35	2.06	0.29	15.00	2.59	0.02	11.40	388.79	502.33	
LG	1000	1750	1.75	226.88	2.06	0.28	15.00	2.53	0.05	11.75	717.18	1004.41	
LG	1500	1750	1.17	226.37	2.06	0.29	15.00	2.44	0.08	12.88	977.06	1508.28	
ØG01	500	1750	3.50	225.50	1.57	0.68	30.00	2.29	0.18	13.94	353.18	501.98	
ØG01	1500	1750	1.17	225.31	1.57	0.69	30.00	2.41	0.12	13.36	657.90	1509.02	
ØG02	500	1750	3.50	227.10	1.65	0.61	25.00	2.08	0.28	19.16	368.56	501.48	
ØG02	1500	1750	1.17	227.31	1.65	0.61	25.00	2.19	0.23	18.70	768.41	1510.10	
ØG03	100	350	3.50	204.25	1.69	0.56	20.00	1.82	0.46	24.59	78.75	100.81	tilt(failed)
ØG03	300	1050	3.50	204.47	1.70	0.56	20.00	2.01	0.32	20.20	191.74	301.00	
ØG03	500	1750	3.50	235.47	1.70	0.56	20.00	2.07	0.28	19.23	330.47	499.57	
ØG03	1000	1750	1.75	204.50	1.70	0.56	20.00	2.24	0.18	19.15	466.53	1002.10	
ØG03	1500	1750	1.17	204.30	1.69	0.56	20.00	2.28	0.16	18.00	622.49	1506.40	
ØG05a	100	350	3.50	223.11	1.93	0.37	15.00	2.05	0.31	17.21	122.98	101.38	
ØG05a_b	100	350	3.50	223.57	1.94	0.37	15.00	2.05	0.30	10.91	130.6	102.0	
ØG05a	500	1750	3.50	223.11	1.93	0.37	15.00	2.23	0.21	15.19	433.36	499.98	
ØG05a	1000	1750	1.75	223.12	1.93	0.37	15.00	2.29	0.18	14.37	765.35	1003.69	
ØG05a	1500	1750	1.17	223.40	1.93	0.37	15.00	2.36	0.15	15.05	967.79	1509.48	
ØG06a	100	350	3.50	225.05	1.75	0.51	25.00	2.22	0.19	15.30	65.21	102.86	
ØG06a	300	1050	3.50	224.32	1.74	0.52	25.00	2.36	0.12	13.17	192.26	301.68	
ØG06a	500	1750	3.50	250.00	1.89	0.40	25.00	1.97	0.34	-	290.83	503.27	
ØG06a	1000	1750	1.75	231.29	1.67	0.58	25.00	2.32	0.14	11.56	493.44	1005.44	
ØG06a	1500	1750	1.17	224.01	1.74	0.52	25.00	2.51	0.05	8.98	712.53	1510.07	
ØG06b	100	350	3.50	204.18	1.89	0.40	10.00	1.90	0.39	19.81	90.55	100.32	tilt
ØG06b_b	100	1750	17.50	205.91	1.86	0.42	10.00	1.94	0.37	18.83	87.0	103.0	
ØG06b	300	1050	3.50	206.43	1.87	0.42	10.00	1.97	0.36	18.92	240.80	301.75	tilt
ØG06b	500	1750	3.50	219.69	1.90	0.40	10.00	2.06	0.30	17.33	356.55	501.02	
ØG06b	1000	1750	1.75	219.58	1.89	0.40	10.00	2.14	0.25	18.92	618.64	1005.98	tilt
ØG06b	1500	1750	1.17	204.36	1.85	0.43	10.00	2.22	0.22	18.62	811.87	1517.16	tilt

Appendix 2

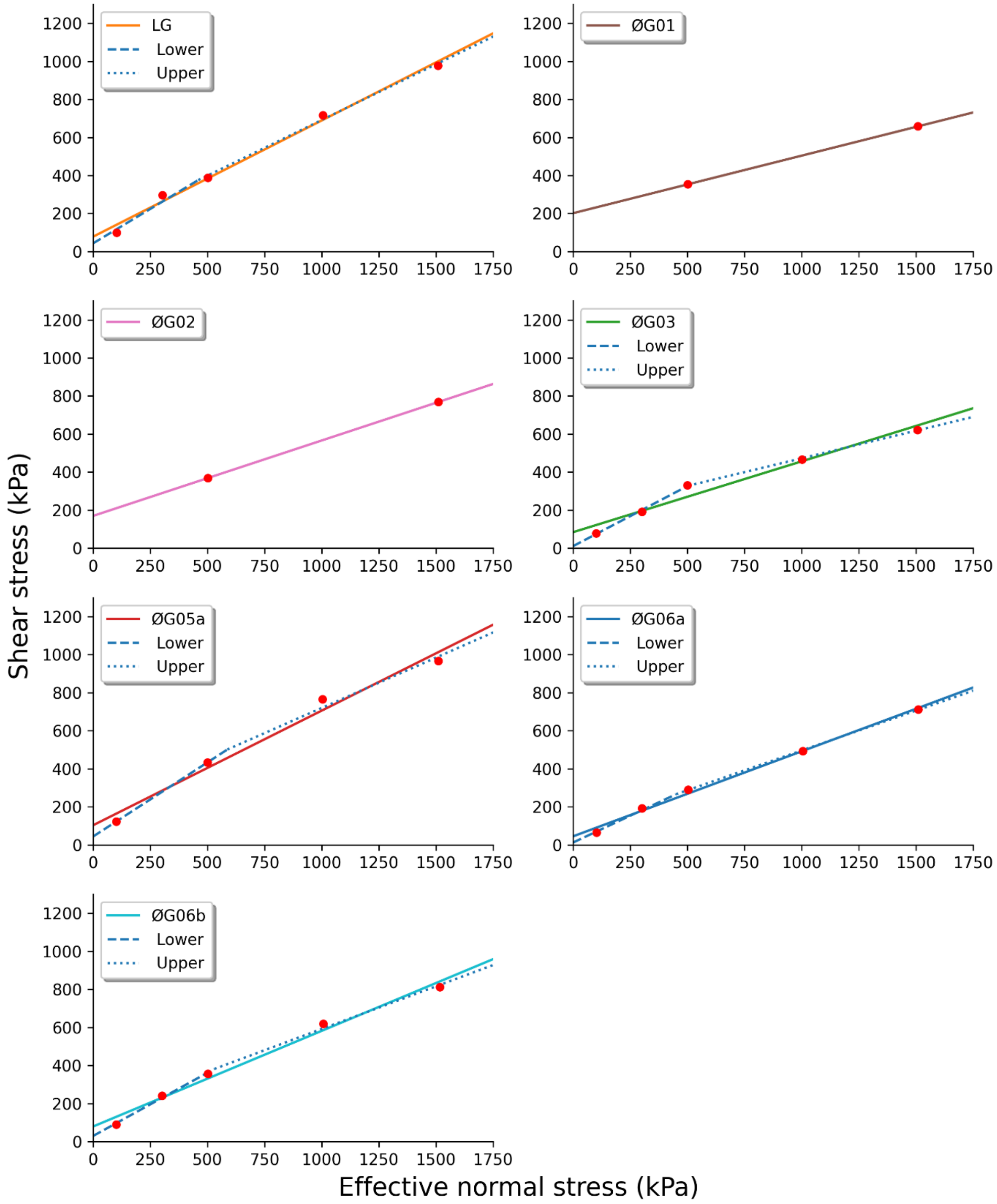

Appendix 2. *Shear stress paths for the tested fault rocks. Shear displacement in mm along x-axis, and applied shear stress along y-axis.*

Appendix 3

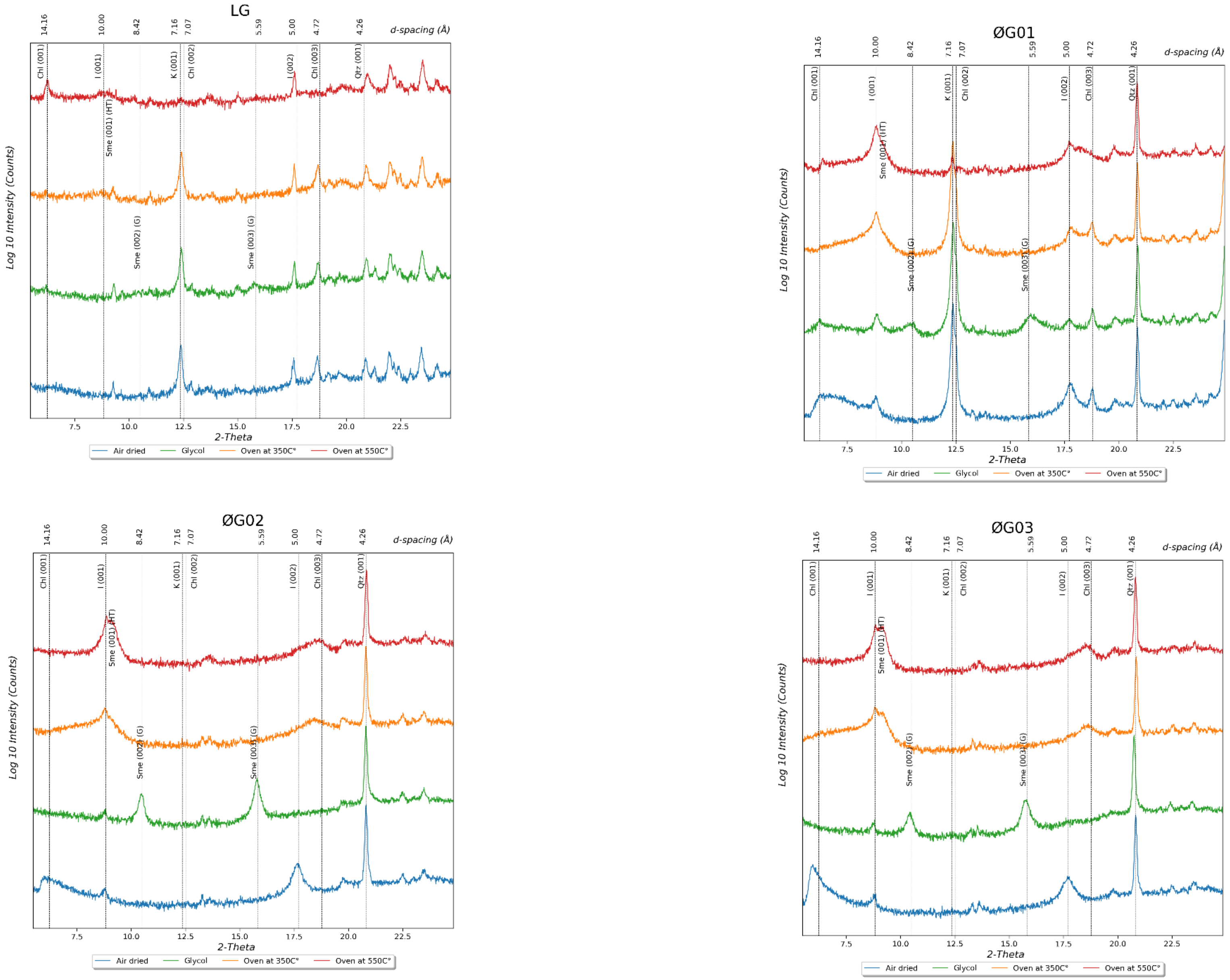

Appendix 3. *Powdered clay analysis XRD patterns. Log10 intensity on the y-axis, while both 2θ and d-spacing (Å) is on the x-axis.*

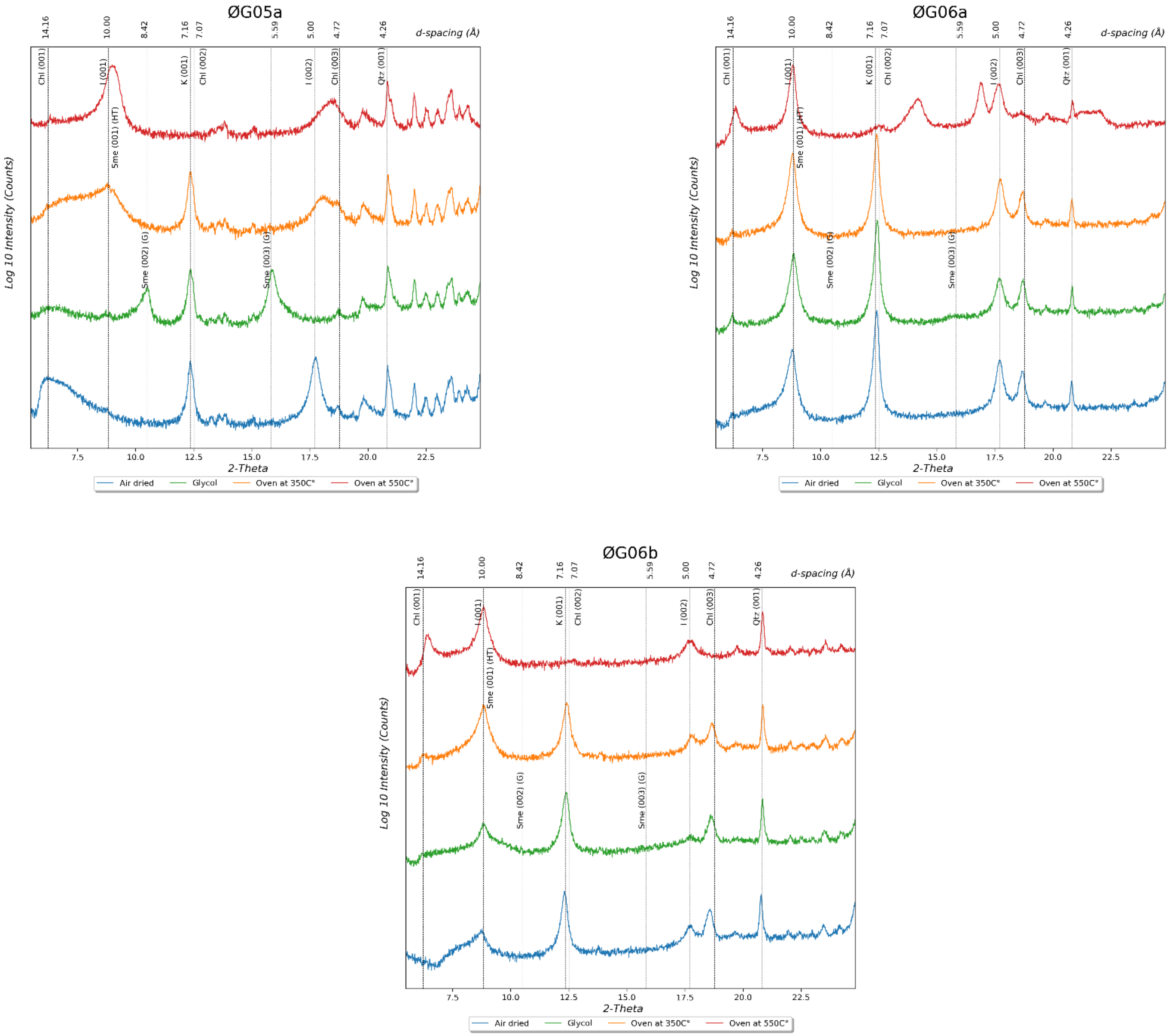

Appendix 3. *Powdered clay analysis XRD patterns. Log10 intensity on the y-axis, while both 2θ and d-spacing (Å) is on the x-axis.*

Appendix 4

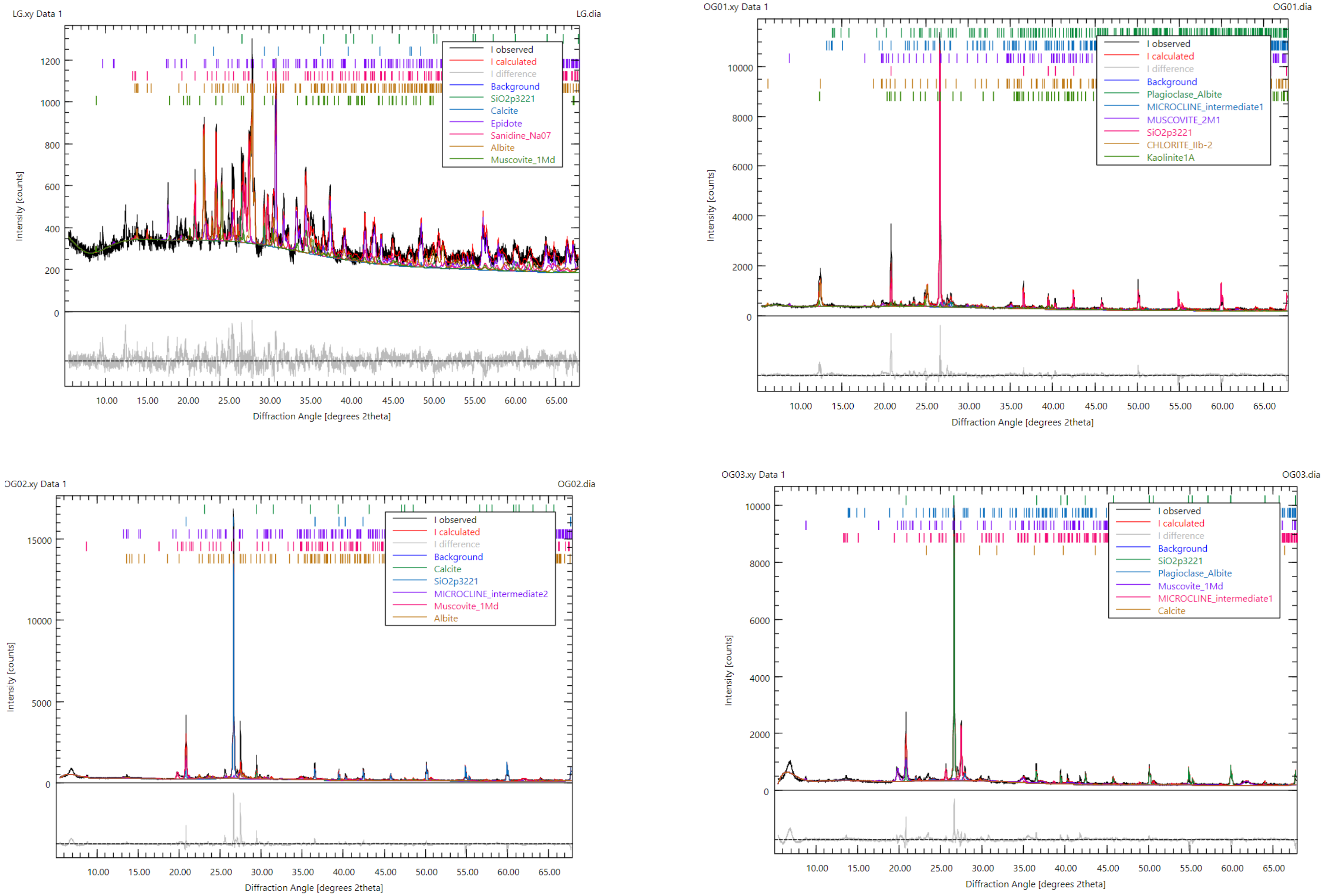

Appendix 4. *Powdered bulk analysis XRD patterns, with Rietveld Refinement curves.*

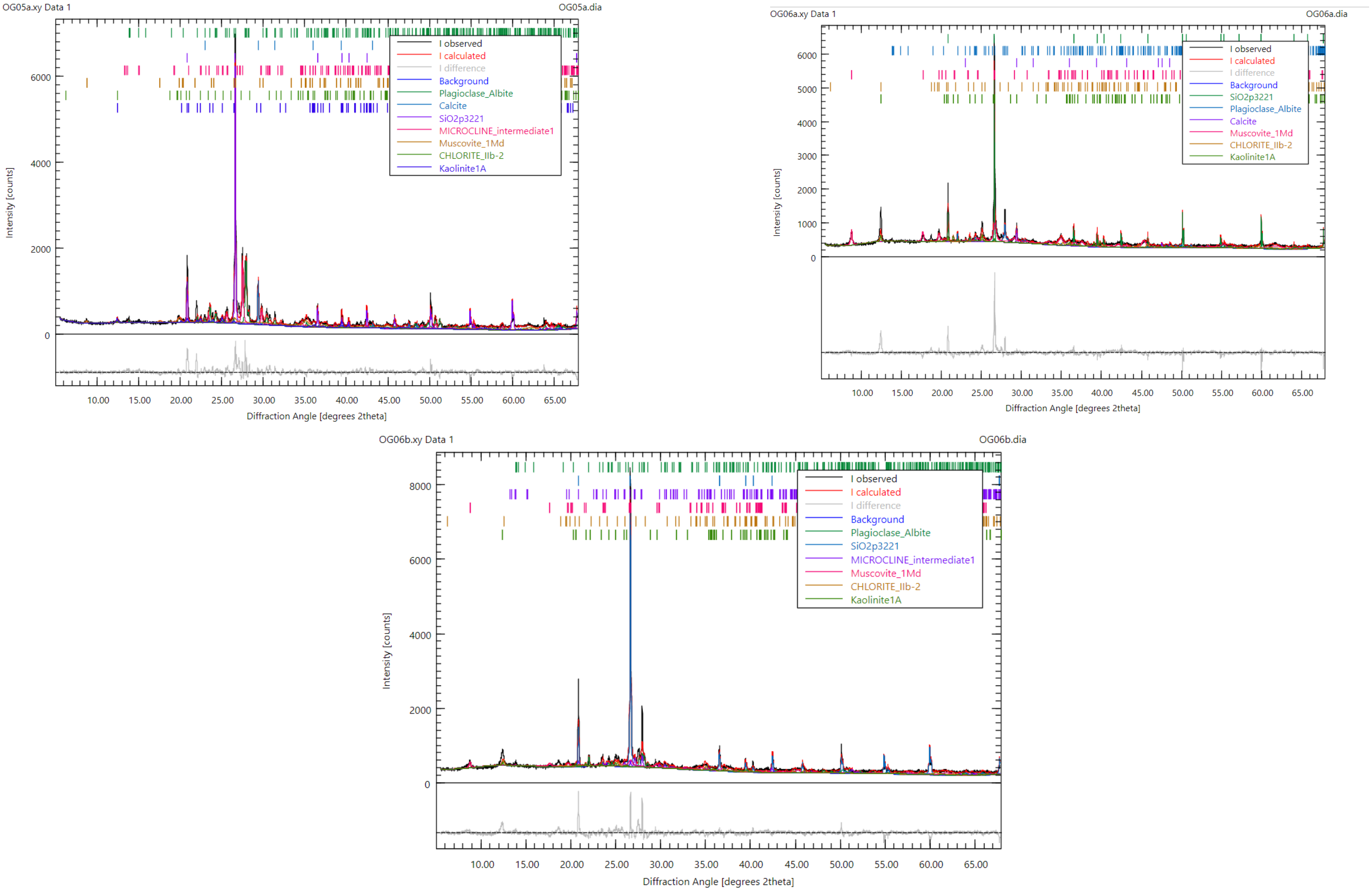

Appendix 4. *Powdered bulk analysis XRD patterns, with Rietveld Refinement curves.*